Characterizing the Spatial Properties of High Harmonic Generation

David Lloyd

St Cross College

University of Oxford

A thesis submitted for the degree of

Doctor of Philosophy

Trinity Term 2014

Abstract

This thesis is concerned with describing a novel technique for characterizing the (spectrally resolved) spatial properties of light. The new approach, known as Scanning Interference Method for Integrated Transverse Analysis of Radiation (SCIMITAR), is a specific implementation of a variable-separation two-pinhole interferometer. Evaluation of the series of interference patterns produced by a SCIMITAR measurement allows the transverse profiles of intensity and spatial phase to be retrieved, while at the same time characterizing the spatial coherence of light. Including a diffraction grating in the simple experimental arrangement permits the spectral dependence of the aforementioned quantities to be measured.

The SCIMITAR technique was demonstrated by characterizing the spatial properties of high harmonic generation (HHG). Excellent agreement with an alternate characterization technique known as SWORD was observed. The spectral dependence of the harmonic spatial properties was also investigated. Evidence suggesting absorption may play a role in shaping the harmonic intensity and spatial coherence was presented. Treating the harmonic radiation as either a fully coherent or partially coherent beam allowed the intensity width, spatial phase curvature and coherence width of the harmonic radiation source to be deduced.

Measurement of the fine variation of the harmonic complex coherence factor (CCF) with pinhole separation revealed distinctive modulations. The Van Cittert-Zernike theorem was modified by including a Gerchberg-Saxton inspired improvement, allowing data missing from the SCIMITAR measurement to be inferred. The harmonic equivalent incoherent source intensity profile was found to be asymmetric with low intensity features isolated away from the optical axis. Calculations of the diffraction pattern produced by illumination of a non-redundant array of pinholes showed that the modulated harmonic properties could adversely influence lensless imaging-type experiments.

I would like to dedicate this thesis to my parents,

for making all things seem possible.

Acknowledgements

This thesis has benefitted immeasurably from the wisdom and support of Simon Hooker and Kevin O'Keeffe. I feel priviledged for having had Simon supervise my DPhil. He has the uncanny ability to see the positives of any situation and has steered me through the uncharted waters of graduate life with skill and patience. Through Kevin I have been schooled in the 'dark arts' of experimental optics. I am grateful that I have been able to call upon his huge experience and I am surely a better scientist for it.

The rest of the Hooker group (past and present) have always been on hand to help or offer a sympathetic ear. Thank you Svet, Andi, Wolf, Nicholas, Anthony, James, Chris, Gavin and Lewis. I have been lucky to share an office with some other great people, ever willing to hear my troubles over a cup of tea (at 4pm promptly, of course). Thank you Katya, Jesse, Vikaran, Matt and David .

Outisde of the Clarendon I have had the pleasure of sharing a house with some fantastic fiends. My thanks to Sherlock, Brian, Gabs, Laura, Abi, Madhuri, Marco and Max H.

It would be remiss to not thank the huge contributions Maxine and Gianni have made, keeping me sane and well-fed over the last few

years. I have enjoyed my time in Oxford far more for having known you both. The house on Cardigan Street was a home away from home thanks to your love and friendship.

Most of all I am grateful for my family, for reasons more numerous than I can describe.

Journal Publications

1. Kevin O'Keeffe, David T. Lloyd, Simon M. Hooker, **"Quasi-phase matched high-order harmonic generation using tunable pulse trains,"** *Optics Express* 22(7), 7722 (2014)

2. Lewis Z. Liu, Kevin OKeeffe, David T. Lloyd and Simon M. Hooker, **"A general analytic solution for far-field phase and amplitude control with a phase only spatial light modulator."** *Optics Letters* 39(7), 2137 (2014)

3. David T. Lloyd, Kevin O'Keeffe, and Simon M. Hooker, **'Complete spatial characterization of an optical wavefront using a variable-separation pinhole pair."** *Optics Letters* 38, 1173-1175 (2013)

Conference Contributions

1. David Lloyd, Kevin OKeeffe and Simon Hooker, **"Order Dependent Spatial Properties of High Harmonic Generation,"** *High Intensity Lasers and High Field Phenomenon (HILAS)*, March 2014

2. David Lloyd, Kevin OKeeffe and Simon Hooker, **"Complete Spatial Characterization of EUV Wavefronts,"** *2013 International Workshop on EUV and Soft X-ray sources*, November 2013

3. Kevin OKeeffe, David Lloyd and Simon Hooker, **"A tunable source of quasi-phase-matched coherent EUV radiation,"** *2013 International Workshop on EUV and Soft X-ray sources* , November 2013

4. David Lloyd, Kevin OKeeffe and Simon Hooker, **'Complete spatial characterization of an optical wavefront using a variable-separation pinhole pair."** *CLEO Europe*, May 2013

5. David Lloyd, Kevin OKeeffe and Simon Hooker, **'Complete spatial characterization of an optical wavefront using a variable-separation pinhole pair."** *Ultrafast Optics*, March 2013

6. David Lloyd, Kevin OKeeffe and Simon Hooker, **'Characterization of the transverse properties of high harmonic radiation using a variable separation pinhole pair,"** *Photon 12*, September 2012

Contents

List of Figures

Chapter 1

Introduction

The demonstration of the optical laser by Maiman in 1960 [109] has proven to be one of the most significant technological feats of the 20th century. The ability to convert incoherent pump energy into a coherent, bright beam of light has enabled not only the creation of a multitude of scientific fields, but also brought about technological changes in areas from ophthalmic surgery to telecommunications.

The experiments of Franken et al. [94], shortly after Maiman's landmark study, conclusively showed how nonlinear optics could be utilised to change (in their case halve) the wavelength of a light. Their pioneering work, the frequency doubling of the ruby laser, is regarded as the first experiment in optical harmonic generation. Nowadays, researchers making use of energetic femtosecond laser pulses routinely employ a more extreme, non-perturbative, version of Franken's early work: high harmonic generation (HHG) [16]. Low order harmonics in the ultraviolet generated in crystals have made way for soft x-ray photons from noble gases, producing, in some cases, radiation with a wavelength as small one 5000th of that of the driving optical laser [88].

There has long been a strong scientific interest in the use of x-rays as a probe of matter. Indeed, Roentgen's early experiments with electrical discharges produced (x-ray) radiation with a previously unobserved, penetrative property, allowing the imaging of the skeletal structure of his wife's hand. Nowadays, bright, pulsed, coherent x-ray sources are found at synchrotrons, and, of late, free-electron lasers (FELs). Such large scale facilities have provided scientists with the tools to probe and image matter on very small length scales and over very short periods of time, enabling ground-breaking work in fields as diverse as biology [60] and archaeology [102]. However, significant capital investment is required for the construction and maintenance of these so called third (e.g synchrotrons) and fourth (e.g FELs) generation light sources. In the case of Diamond, the synchrotron facility situated in Oxfordshire in the UK, the initial outlay was greater than £260 million [116]. A means of producing similar extreme ultraviolet (XUV)[1] and soft x-ray (SXR)[2] radiation from a table-top sized machine would serve as a cost effective means of extending access and application of light in this part of the spectrum.

The pursuit of compact, coherent, short-wavelength lasers has been hampered by the fact that laser pump power scales with the inverse of somewhere between the third and sixth power of the lasing frequency:[3] a laser operating in the XUV spectrum would require a pump power density exceeding 100 MW/cm^3 [12], prohibitively large compared to existing technologies. The frequency conversion of optical lasers in the near infrared (NIR) to the XUV presents a feasible means of circumventing this issue.

A typical high harmonic light source requires linearly polarized laser pulses,

[1]The extreme ultraviolet spectrum covers the wavelength range from 124 to 10nm.
[2]The soft x-ray spectrum covers the wavelength range 10 to 0.1 nm.
[3]The exponent depends on the particular broadening mechanism employed.

usually with a wavelength in the visible or near infrared, around a few 100's of microjoules in energy, with a duration of a few 10's of femtoseconds, focussed into some 10's of millibar of a noble gas. For a peak intensity of the order of $10^{14} - 10^{15}$ W/cm^2, the extreme non-linear interaction of light with a gaseous media produces a collinear beam of harmonic radiation. The inherent simplicity of the HHG arrangement, coupled with the capability of producing coherent, spectrally bright radiation with an incredibly short pulse duration, sub 130 attoseconds (1 attosecond $=10^{18}$ seconds) has been reported [35], has led to the rapid uptake of the technique as the table-top source of choice for experiments in chemistry [80], materials science [24] and metrology [23], among many other areas. Despite the great success of studies centred on understanding and exploiting HHG, both through experiment and simulation, significant scope remains to further optimise, and better utilise, the radiation produced through this technique. One approach to furthering our knowledge of HHG is based up performing a detailed characterization of the properties of the generated radiation.

In the temporal domain, pulse characterization has shown that the different spectral components of HHG can be produced phase-locked and, generally, lead to the production a train of XUV pulses per single driving laser pulse [91]. A single, isolated attosecond pulse per driving laser pulse may be produced [58] using a variety of methods, amongst which spectral filtering of the harmonic cut-off is often used owing to its inherent simplicity. The demonstration of control over pulses so short in duration heralded the beginning of experimental studies in the attosecond domain and made very real the prospect of controlling matter on the natural time scale of electronic process in atoms and molecules.

In the spatial domain, measurements of the spatial coherence of phase-matched

HHG from a capillary waveguide have found the radiation to be essentially fully coherent [72], paving the way for applications which exploit this desirable property such as coherent diffractive imaging [76] and dynamic holography [74]. The significance of this result must be understood in context; alternate sources of soft x-rays, (for instance laser-plasma sources and synchrotrons) possess intrinsically poor spatial coherence [41, 92]. Improving the transverse coherence of these incoherent sources is only possible by illumination of a pinhole, at the expense of a great reduction in flux. The unique combination of attosecond pulse duration, short-wavelength and high spatial coherence from a compact, laboratory sized arrangement found in HHG, presents manifold possibilities to perform studies of matter at the natural time and length scale of microscopic behaviour.

In the studies described above, appropriate and accurate characterization, whether in the spatial or temporal domain, displayed the true potential of HHG for application in areas of intense scientific interest. Further, characterization enabled optimisation of the radiation source by providing knowledge of the properties of interest while also providing an insight into intense light-matter interaction. In addition to the above two points, the accurate modelling of the propagation of light through an optical system is contingent on knowledge of the properties, both spatial and temporal, of the illumination. With this in mind, we can broadly identify the three motivations for performing characterization:

1. **Optimisation**. Of the light, for a particular activity.

2. **Generation**. To provide insight into how the radiation is produced.

3. **Propagation**. Information to enable the modelling of optical systems.

Throughout this thesis, the purpose and consequences of the presented work will be referenced back to these three motivating aspects.

1.1 Scope of This Thesis

A number of questions remain unanswered (or equally well, poorly explored) regarding the nature of the spatial properties of HHG. In particular, the dependence of beam characteristics on harmonic order is a facet worthy of further investigation and quantification. With respect to the spatial coherence of HHG, a wide range of aspects have yet to be addressed. For instance, measurements of the fine variation of the spatial coherence with test point separation, experiments aimed at explaining the origin of partial coherence in HHG, as well as tests on whether different parts of the transverse beam posses equal coherence properties, are just three potential areas, among many others, where research could be directed.

This thesis is aimed at addressing the questions outlined in brief above. In chapter 2 the main theoretical underpinnings of HHG are outlined, with an emphasis on some physical phenomena that contribute to final harmonic spatial properties. Chapter 3 provides an account of pulse metrology, highlighting properties of interest and techniques developed for measuring them. The chapter also provides an outline on some theories of the propagation of light from a statistical standpoint.

Chapter 4 describes, in detail, a new method for measuring the frequency-resolved spatial properties of light as well as showing results from the technique's first application to characterizing HHG. Chapter 5 is dedicated to describing the results of an experiment aimed at quantifying the spectral dependence of

HHG spatial properties, whilst also describing the implications with respect to the harmonic source size and spatial coherence. In chapter 6 the observation of hitherto unreported modulations in the HHG transverse properties is reported, with some effort given to explaining their possible origin. Chapter 7 concludes the thesis, offering some suggestions on the implications of the described work and potential future research directions.

1.2 Role of the Author

All work presented in this thesis was completed by the author, under the supervision of Prof. Simon Hooker and with guidance from Dr. Kevin O'Keeffe. The experimental beamline used to carry out the characterization experiments was constructed by the author with the exception of the the hollow core fibre and chirped mirror set. This was installed by Dr. Felix Frank, Mr. William Okell and Prof. John Tisch and was tested by the author with the help of Dr. Kevin O'Keeffe. All experimental data was recorded and analysed by the author, with guidance and support from Dr. Kevin O'Keeffe and Prof. Simon Hooker.

Chapter 2

High Harmonic Generation

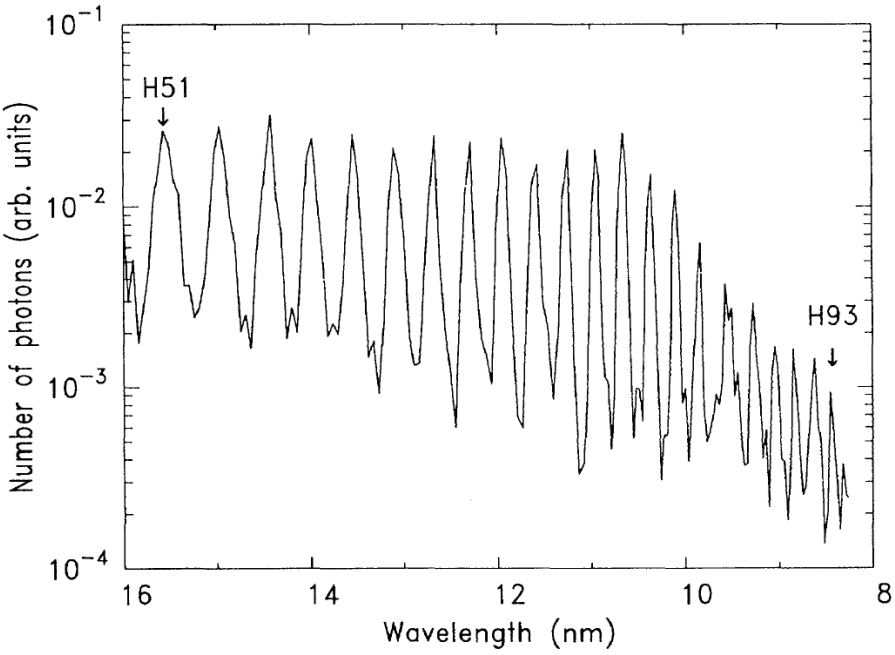

Figure 2.1: Experimental HHG spectrum generated in helium by laser pulses focussed to an intensity of 1×10^{15} Wcm^{-2}. A clear plateau of equal intensity harmonics is followed by an abrupt cut-off in the spectrum. Figure taken from [121].

The development of chirped pulse amplification (CPA) and the subsequent construction of ultrafast, titanium-doped sapphire (Ti:sapphire) laser amplifiers has enabled the routine production of linearly polarized laser pulses with peak intensities in the region $10^{14} - 10^{15}$ Wcm^{-2}, from now commercially available systems. The interaction of light of such an intensity with a gas medium produces harmonic radiation. Each harmonic frequency (ω_q) obeys the relationship $\omega_q = q\omega_0$, where ω_0 is the fundamental frequency of the driving laser and, for the case of interaction with a gas,[1] q is an odd-integer. In the frequency domain, a typical high harmonic spectrum is composed of a comb with decreasing intensity over the first few orders (comb teeth), followed by an extended plateau of equal strength harmonics, proceeded by an abrupt cut-off at the maximum photon energy. An example spectrum, taken from [121], is shown in figure 2.1. The cut-off frequency may be very large, extending into several 100's or even 1000's of times the fundamental laser frequency. Over the last twenty years, significant effort has been directed into creating a firm theoretical description of the physics of light-matter interaction in the intensity regime relevant for HHG. Here we give an overview highlighting some of the underlying concepts.

2.1 The Simple Man's Model

The work of Paul Corkum in 1993 [11] combined aspects of quantum and classical mechanics to provide a theoretical description of high harmonic generation. His modestly titled 'Simple man's model' provides a basis for tackling the underlying physical phenomena which govern the non-linear up-conversion of light.

[1] Or any other centro-symmetric medium.

Corkum showed that the interaction of an intense laser field with a neutral atom in the non-perturbative regime (i.e where the laser electric field approaches the level of the coulomb potential) can be framed in terms of a three-step process:

1. **Ionization**

   The laser field initially perturbs the potential of a neutral atom in its ground-state, allowing an electron to undergo tunnel ionization and to instantly be born into the continuum.

2. **Propagation**

   The freed electron, starting from rest, is accelerated by the ponderomotive potential of the strong laser field, obeying the classical equation of motion.

3. **Recombination**

   The force of the laser field changes sign, reversing the direction of the electron motion. About 50% of the possible electron trajectories return to the location of the parent atom after some excursion time (typically a half cycle of the laser field) and the subsequent recombination allows the emission of a harmonic (high energy) photon.

Step one requires the calculation of the probability of ionization. The Keldysh parameter (γ) offers a guide as to which ionization mechanism dominates for a given set of laser parameters:[1]

$$\gamma = \frac{\omega_0}{E_0 e}\sqrt{2 I_p m_e} \tag{2.1}$$

[1]The Keldysh parameter may be thought of as the ratio of the laser period to the time taken for an electron to tunnel.

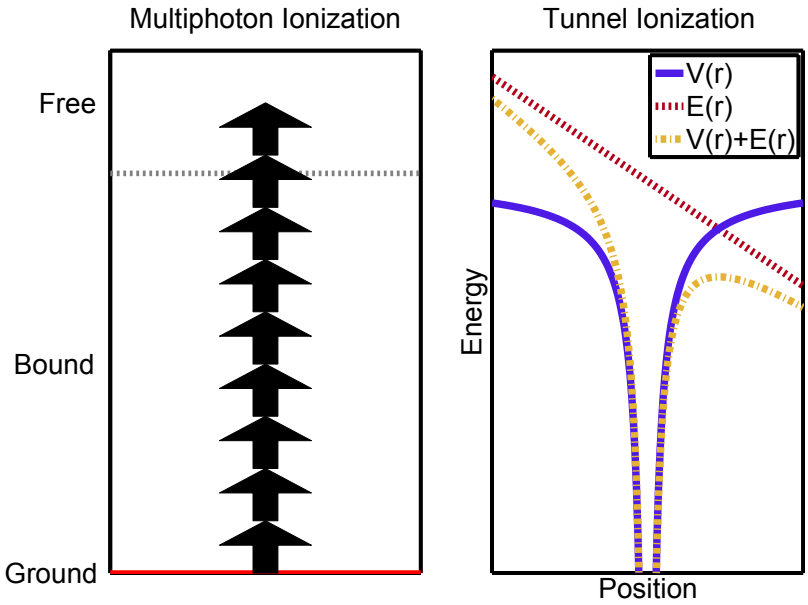

Figure 2.2: Left: schematic representing multiphoton ionization. Many photons (represented by black arrows) are absorbed exciting an electron from a bound to a free state. Right: diagram representing tunnel ionization. The atomic potential $V(r)$, is perturbed by the laser potential $E(r)$, resulting in the distorted potential $V(r) + E(r)$, enhancing the tunnelling probability.

where E_0 is the laser electric field magnitude, I_p is the ionization potential of the target atom species and m_e and e are the electron mass and charge, respectively. When $\gamma \ll 1$, optical field ionization (tunnelling) dominates, whereas for $\gamma \gg 1$ multiphoton ionization is the more important mechanism. The two situations are represented in figure 2.2.

The Keldysh parameter, calculated for a number of atomic species, under relevant laser conditions, is shown in table 2.1. In the regime relevant to high harmonic generation typically $\gamma < 1$.

Corkum called upon the work of Ammosov, Delone and Krainov (referred to

Atom Species	Ionization Potential (eV)	Keldysh Parameter
Xenon 1^+	12.14	0.45
Xenon 2^+	20.98	0.59
Argon 1^+	15.76	0.51
Argon 2^+	27.93	0.68
Neon 1^+	21.56	0.60
Neon 2^+	40.96	0.83
Helium 1^+	24.58	0.64
Helium 2^+	54.42	0.96

Table 2.1: Table showing the Keldysh parameter calculated for laser parameters of $I = 5 \times 10^{14}$ Wcm^{-2} and $\lambda = 800$ nm, for a number of atomic species and final charge states.

collectively as ADK), who derived the rate for tunnel ionization of a neutral atom exposed to a strong laser field [3]. The ionization rate can be calculated from:

$$W = \omega_s |C_{n^*l^*}|^2 G_{lm} \left(\frac{4\omega_s}{\omega_t}\right)^{2n^*-m-1} \exp\left(\frac{-4\omega_s}{3\omega_t}\right) \tag{2.2}$$

where $\omega_s = I_p^0/\hbar$, $\omega_t = eE_0(2m_3 I_p^0)^{-\frac{1}{2}}$, $n^* = \left(\frac{I_p^h}{I_p^0}\right)^{\frac{1}{2}}$, G_{lm} is a factor which depends on the quantum numbers, l and m, and $C_{n^*l^*}$ is a factor which depends on the quantum numbers n and l. The ionization potential of the atom in question is given by I_p^0, I_p^h is the ionization potential of hydrogen and E_0 is the applied laser electric field magnitude. The probability of ionization $P(t)$ in a time interval dt is given by $P(t) = W(\mathcal{E}(t))dt$. An example of an ADK calculation for argon atoms exposed to an intense laser field is shown in figure 2.3.

For the second step of the model, the motion of the electron is treated classically, assuming that it starts from rest at the instant of ionization (t_0). The effect of the Coulomb potential of the atom is neglected. In one spatial dimension, the

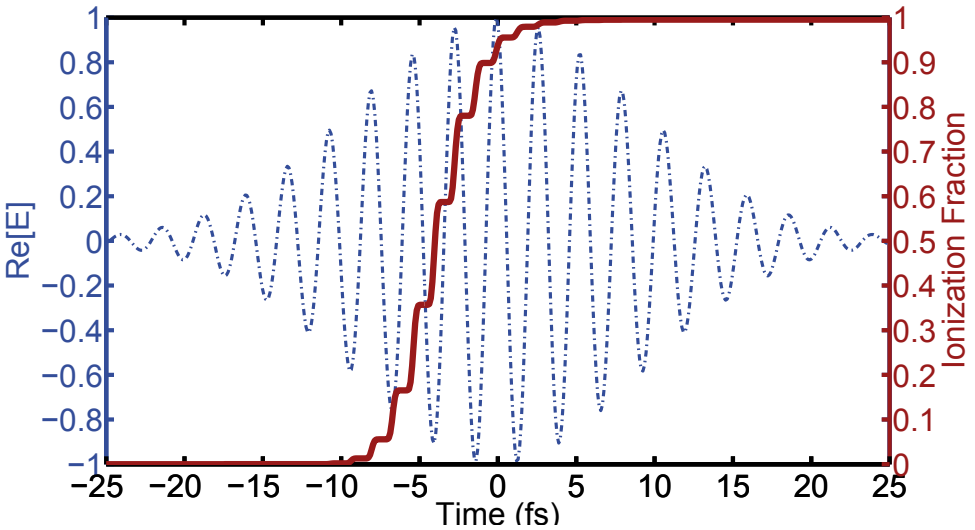

Figure 2.3: Calculation, based on the (ADK) theory described in [3], of the fraction (brown solid line) of ionized argon atoms, during the interaction of a 15 fs laser pulse focussed to a peak intensity of 6×10^{14} W/cm^2. The real part of the laser electric field is shown by the blue dot-dashed line.

electron's position (x) is given by:

$$x(t, t_0) = \frac{e\mathcal{E}}{m\omega^2} \left[\cos(\omega t_0)\cos(\omega t) - \omega(t - t_0)\sin(\omega t_0)\right] \tag{2.3}$$

where e and m are the electron charge and mass, respectively. The phase of the driving laser field at the moment of ionization (ϕ_b) is given by $\phi_b = \omega t_0$, such that ionization at the laser cycle peak occurs for $\phi_b = 0$. The subsequent path, or trajectory, the electron takes under only the influence of the laser field, is determined by the instant of ionization. Analytical evaluation of equation 2.3 shows that only select electron trajectories bring the electron back to the vicinity of the atom. Specifically those which obey:

$$0 < \phi_b < \pi/2 \tag{2.4}$$

or

$$\pi < \phi_b < 3\pi/2. \tag{2.5}$$

The third step of the model not only identifies which electron trajectories are viable for harmonic photon emission but also estimates the electron wavepacket spreading, a factor affecting the recollision cross section. This allows evaluation of the electron continuum state-bound state transition dipole matrix element and thus the probability of recollision.

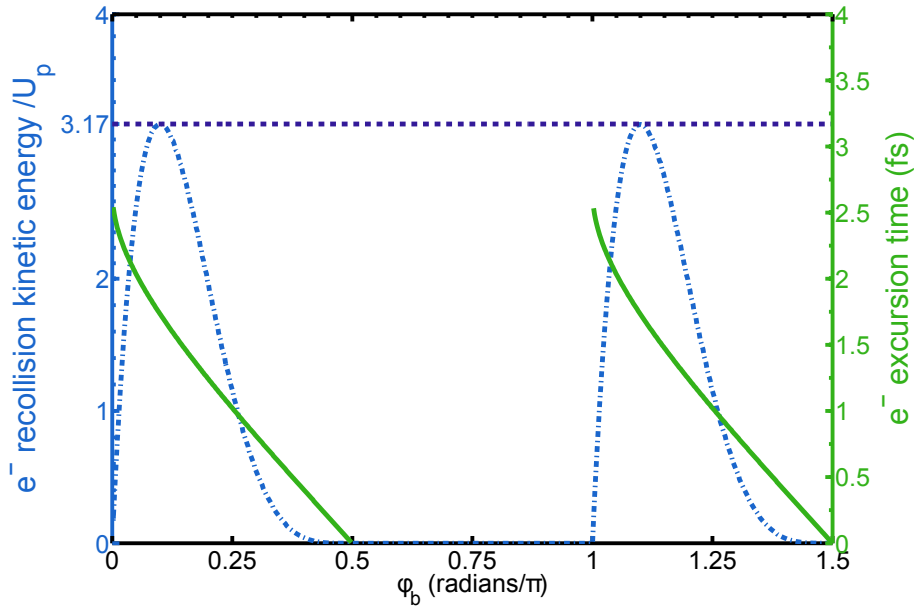

Figure 2.4: The kinetic energy, evaluated at the moment of recollision, gained by an electron accelerated by a laser field (dot-dashed blue line) and total time an electron spends in the continuum (solid green line) are plotted as functions of the laser phase at the time the electron is ionized. The purple dotted line shows the maximum kinetic energy an electron may gain as a multiple of the ponderomotive potential (U_p). All plots are shown for a laser wavelength of 800 nm.

The calculated electron kinetic energy at the moment of recollision is shown in figure 2.4. The largest return energy is obtained twice (once per half cycle of

the laser), and is equal to a little over $3U_p$, where $U_p = \frac{eE_0^2}{4m\omega_0^2}$ is the ponderomotive potential of the laser field. Evaluation of the harmonic cut-off (highest) photon frequency ($\nu_{\max}$) yields:

$$h\nu_{\max} = I_{\mathrm{p}} + 3.17U_{\mathrm{p}} \tag{2.6}$$

where I_{p} is the ionization potential of the atom. Equation 2.6 has been found to agree with the spectral cut-off observed in experiments of HHG after macroscopic effects were been taken into account [15], suggesting that the simple man's model captures much of the essential physics of the problem.

Figure 2.4 shows that, for all but the cut-off harmonic emission, two possible electron trajectories (uniquely identified by different values of ϕ_b) can produce a harmonic photon of the same energy. The time an electron spends in the continuum as a function of the laser phase is also shown in figure 2.4. It is clear that, for given harmonic energy less than the cut-off, the two trajectories differ in the amount of time spent in continuum. Specifically, the electrons born in to the continuum early in the laser half cycle proceed on a longer journey than those born later. The two contributions are identified as the "long" and "short" electron trajectories after the respective length of their excursions. The model doesn't preclude the possibility that the electron may collide after a (larger) number of laser cycles. However, since we are considering one dimensional motion, such trajectories would require the electron to remain free after encountering the parent atom the first and potentially subsequent times.

2.2 Further Theoretical Developments

Corkum's three step model came at a time of fruitful theoretical research into intense light-matter interaction. Krause et al. [105], numerically solved the time-dependent Schrdinger equation (TDSE) to simulate harmonic spectra from both neutral atoms and ions. Such an approach, despite proving successful in modelling the HHG process, is hampered by both the significant computational requirements and the difficulty of modelling systems driven by lasers with arbitrary laser polarization states and spectral content.

Lewenstein et al. [59] built upon the earlier work of Corkum by formulating a fully quantum mechanical treatment of the three step model. The second step, propagation, previously modelled using the classical equation of motion, was recast as an integral over possible quantum paths. Their work includes more rigorous treatment of effects such as quantum wavepacket diffusion. The authors wished to explore three key assumptions of Corkum's work from a purely quantum, rather than semi-classical basis. Those assumptions are that harmonic emission is dominated by liberated electrons which:

1. return to the nucleus.

2. appear in the continuum with zero velocity.

3. have a return kinetic energy equal to the energy of the emitted harmonic photon.

The authors derived a quantum mechanical expression for the time-dependent dipole moment involving integration over both time and momentum. The integration over momentum was found to be dominated by stationary points in the classical action of the electron. Said stationary points corresponded to electron trajectories which return to close (within a Bohr radius) of the parent nucleus, thus providing a justification for Corkum's first assumption. The integral over time was dominated by a saddle point which corresponded to an electron with an initial velocity of zero, justifying assumption two. The third and final assumption was justified by calculating the Fourier transform of the dipole moment, a quantity equivalent to the harmonic spectrum. This process provided a link between harmonic emission of a given photon energy and the kinetic energy of the recolliding electron, addressing the third and final assumption. Lewenstein et al.'s model benefits from being far quicker to compute compared to earlier work centered on solving the TDSE.

In a later publication Lewenstein and co-authors [107] applied their fully quantum version of the three step model to study the phase of the atomic dipole, specifically its intensity dependence. They emphasised that the phase of the induced atomic dipole responsible for harmonic emission can be associated with the value of the action of a freed electron under the influence of the laser field. As such the phase of emission depends on the excursion time of the particular electron trajectory. Specifically, the phase may effectively be treated as a linear function of the laser ponderomotive potential, with the slope dependent on whether the harmonic emission occurs in the cut-off or plateau spectral regions.

2.3 Propagation and Phase-matching

Calculation of the single atom response of a system irradiated by an intense laser pulse, as described through the work of Lewnstein et al. in the previous section, provided a fascinating insight into the physics behind HHG. However, some differences between calculated and measured experimental spectra were observed [15]. The microscopic picture, that of light interacting with a single atom, insufficiently encompasses all aspects of the problem. An understanding of the macroscopic response of the media, that is, the bulk behaviour of the laser pulse interaction with a finite volume of gas, is needed.

Common to all non-linear processes, dispersion is a key factor in the efficient generation of harmonic light. Typically, the phase velocity of light propagating in a material possesses a wavelength dependence. Thus, a harmonic photon created at the beginning of a medium may not necessarily be in phase with light generated further on, at a later time. The derivation for the expression of the harmonic signal as a function of propagation distance in a dispersive medium is a well-known textbook exercise; the reader is referred to the excellent treatment by Boyd [5] for a full derivation. Here we quote the result for a continuous wave driving laser field, denoted by $E_0^{(\omega)}$, which induces a non-linear polarization, P_{NL} in a medium. The resultant intensity of the harmonic field of order q, $I^{(q\omega)}(z)$ is given by :

$$I^{(q\omega)}(z) = \frac{B^{(q\omega)}}{\Delta k^2}\sin^2\left(\frac{\Delta k z}{2}\right) \tag{2.7}$$

where z denotes the longitudinal position in medium, $B^{(q\omega)}$ is related to the

induced nonlinear polarization and Δk is given by:

$$\Delta k_q = k(q\omega) - qk(\omega). \tag{2.8}$$

Most media are dispersive and $k(q\omega) \neq qk(\omega)$, in which case the harmonic intensity will oscillate with propagation distance z. The distance over which a π phase is accumulated between local and previously generated harmonics is known as the coherence length, L_c:

$$L_c = \frac{\pi}{|\Delta k|}. \tag{2.9}$$

If a system can be engineered such that $k(q\omega) = qk(\omega)$ the harmonic intensity is said to be phase-matched, experiencing quadratic growth with distance:

$$I_{\mathrm{pm}}^{(q\omega)} = \frac{B^{(q\omega)}}{4} z^2. \tag{2.10}$$

An alternate means of addressing this limitation of harmonic generation in the dispersive regime is known as quasi-phase-matching (QPM), where regions in the generating medium which might otherwise contribute destructively to the measured signal are either re-phased or suppressed altogether. The technique has proved successful for improving the efficiency of second harmonic generation from solid state lasers using periodically poled lithium niobate (PPLN) crystals. For HHG, a number of QPM schemes have been demonstrated. In a free focus geometry, Seres et al. [51] employed multiple gas cells, appropriately separated longitudinally to provide the required modulation in HHG signal. In a waveguide geometry, mode beating [64], waveguide mode diameter modulation [31] and

counter propagating pulse trains [90] have all been used to achieve QPM and improve the conversion efficiency of the source.

2.3.1 Causes of Dispersion

Relevant to HHG, there are a number of contributions to the overall dispersion of a system:

1. Gas media

   (a) Neutral Atoms

   Dispersion arises from a difference in the (neutral gas) refractive index encountered by the fundamental and harmonic:

$$\Delta k_N = \frac{2\pi q}{\lambda_0}\Big[n(\lambda_0) - n\Big(\frac{\lambda_0}{q}\Big)\Big](1-\eta)\frac{P}{P_{atm}} \tag{2.11}$$

   where n is the refractive index, η is the fraction of ionized atoms, P and P_{atm} are the gas pressure and atmospheric pressure, respectively. Control of the neutral gas dispersion comes from setting the pressure in the medium.

   (b) Ionized Atoms

   During the course of HHG, approximately half of the electrons liberated by the laser field fail to return to the parent nucleus, producing a plasma. The plasma refractive index (n_{P}) is given by:

$$n_{\mathrm{P}} = \sqrt{1 - \Big(\frac{\omega_{\mathrm{P}}}{\omega}\Big)^2} \tag{2.12}$$

   where $\omega_{\mathrm{P}} = \frac{N_e e^2}{\epsilon_0 m_e}$ is the plasma frequency, N_e is the free electron den-

sity, ϵ_0 is the permittivity of free space, and m and e are the electron mass and charge respectively. The wavenumber is well approximated by the expression:

$$k_{\mathrm{P}} \approx \frac{\omega}{c} - \frac{\omega_{\mathrm{P}}^2}{2\omega^2 c}. \tag{2.13}$$

The contribution to the dispersion can then be written as:

$$\Delta k_{\mathrm{P}} = qk(\omega_0) - k(q\omega_0) \tag{2.14}$$

$$= -N_e r_e \lambda q + \frac{N_e r_e \lambda}{q^2} \Delta k_{\mathrm{P}}$$

$$\approx -N_e r_e \lambda_0 q \tag{2.15}$$

where $r_e = e^2/4\pi\epsilon_0 m_e c^2$ is the classical electron radius. Equation 2.15 is valid when $q \gg 1$. The free electron density is driven by ionization from the intense laser field. Pulses with shorter duration (fewer cycles) will produce fewer free electrons prior to generation of a harmonic of a given order [6].

2. Geometric

   (a) Free Focus

   In a free focus geometry, a focussed beam accumulates a π phase change,[1] the so called Gouy phase:

$$\Phi_{\mathrm{g}} = \frac{1}{b + 2iz} \exp\Big(- \frac{kr^2}{b + 2iz} \Big) \tag{2.16}$$

[1] The π phase change is accrued between $z = -\infty$ and $z = \infty$. Naturally, a smaller phase change occurs over smaller distances.

where b is the confocal parameter, related to the beam waist size (w_0) through $b = \frac{2\pi w_0^2}{\lambda}$. The associated wavevector is given by $k_g = \nabla\Phi_g$. The Gouy phase experienced during the generation process can be changed by shifting the longitudinal position of the generating medium, with respect to the laser focus, or though shaping (aperturing) the fundamental beam.

(b) Waveguide

In the case where the harmonic radiation is generated in a (cylindrically symmetric) waveguide, an additional contribution to the dispersion takes the form of:

$$\Delta k_{\mathrm{wg}} = -\frac{u_{n,m}^2 \lambda q}{4\pi a^2} \tag{2.17}$$

where $u_{n,m}$ is the mth root of the (n-1)th Bessel function on the first kind and a is the waveguide inner radius.

The overall dispersion of the system is simply the sum of all the relevant contributions. Phase-matching is achieved when $\Delta k = 0$. This is possible, in practice by adjusting the gas pressure of the generating medium to balance the (oppositely signed) contributions from neutral and ionized atoms [21]. However, there is a maximum ionization fraction for which this can be achieved; any higher and no suitable gas pressure can be found to satisfy $\Delta k = 0$. In the simplified case where geometric dispersion is neglected this so-called critical ionization fraction is given by:

$$\eta_{\mathrm{crit}} = \left(1 + \frac{N_{\mathrm{atm}} r_e \lambda^2}{2\pi\Delta n}\right) \tag{2.18}$$

where N_{atm} is the number of atoms per unit volume at atmospheric pressure[1] and $\Delta n = n(\lambda) - n\left(\frac{\lambda}{q}\right)$. Considering the temporal profile of a laser pulse, harmonics of a higher order are generated at higher peak intensities, later on in the pulse. Such later times are associated with higher levels of ionization, as evidenced in figure 2.3. If such harmonics are generated in the medium after η exceeds η_{crit} they may not be phase-matched through simple pressure tuning.

2.4 The Harmonic Wavefront

The spatial phase profile of the harmonic field in the generating medium is related to that of the induced non-linear polarization. There are two principle contributions (shown here for a Gaussian beam) [71]:[2]

1. Fundamental phase

   The harmonic wavefront inherits the phase of the fundamental driving laser, albeit multiplied by the harmonic order:

$$\Phi_{\text{fun}}(r, z, q) = -q \arctan\left(\frac{2z}{b}\right) + q\frac{2z}{b}\left(\frac{r}{w(z)}\right)^2 \tag{2.19}$$

   where b is the confocal parameter and $w(z)$ is the fundamental beam width.

2. Intensity dependent phase

   The phase of the dipole responsible for harmonic emission can be equated to the semiclassical action (S) acquired by the electron during its sojourn

[1] The relationship $\frac{N_{\text{atm}}}{N_e} = \frac{P_{\text{atm}}}{P}$ has been used here to derive η_{crit}.

[2] In the case of a molecular gas, additional contributions to the harmonic phase arising from tunnelling [66] and the transition moment [14] may also contribute to the harmonic wavefront.

in the continuum, as per the model of Lewenstein et al. [107]:

$$\Phi_{\text{Int}} = q\omega t_f - \frac{1}{\hbar} S(p_{\text{st}}, t_i, t_f) \tag{2.20}$$

where t_i and t_f are the times the electron enters the continuum and returns to the nucleus, for a given trajectory, respectively, and p_{st} is the stationary action value of the canonical momentum. The action is well approximated by:

$$S \approx -\tau_s U_p \tag{2.21}$$

where τ_s is the return time of the electron. This implies that the phase itself is proportional to the fundamental intensity:

$$\begin{aligned} \Phi_{\text{Int}}(r, z, q) \approx -\alpha I(r, z) &= \frac{-\alpha I_0}{1 + (\frac{2z}{b})^2} \exp\Big[-2\Big(\frac{r}{w(z)}\Big)^2 \Big] \\ &\simeq \frac{-\alpha I_0}{1 + (\frac{2z}{b})^2} + \frac{2\alpha I_0}{1 + (\frac{2z}{b})^2} \Big(\frac{r}{w(z)}\Big)^2 \end{aligned} \tag{2.22}$$

where α is a (positive) proportionality constant, the value of which depends on the spectral location of the harmonic order (plateau or cut-off) and I_0 is the peak fundamental intensity.

For a given position z about the focus, the harmonic phase is found to take the form:

$$\begin{aligned} \Phi_q &= \Phi_{\text{fun}} + \Phi_{\text{Int}} \\ \Phi_q &= -\alpha I_q \exp\Big[-\frac{r^2}{w(z)^2} \Big] + \frac{qz\lambda}{\pi w_0^2 w_z^2} r^2 \end{aligned}$$

$$\approx \left\{ \frac{2\alpha I_q}{w(z)^2} + \frac{qz\lambda}{\pi w_0^2 w(z)^2} \right\} r^2 \tag{2.23}$$

where only terms explicitly dependent on r are retained, I_q is the intensity at which harmonic q is generated and, in the second line, we have assumed we are concerned with positions (r), close to the optical axis. Equation 2.23 takes the form of a parabolic wavefront: $\Phi_q = \frac{k}{2R} r^2$, where R is the radius of curvature. In equation 2.23 I_q depends on the harmonic order q. If we assume that the brightest harmonics are generated when the laser intensity is large enough that the harmonic cut-off is q, then equation 2.6 can be inverted yielding an expression for I_q:

$$I_q(q) = \frac{qhc}{\lambda_0^3 \kappa} - \frac{I_\mathrm{p}}{\kappa \lambda_0^2} \tag{2.24}$$

where κ is a constant that depends on the units I_q and λ_0 are expressed in.[1] It is reasonable to assume that rather than a given harmonic q being generated at the minimum possible intensity, as defined by equation 2.24, it is produced by some larger intensity $\beta I_q(q)$, where $\beta > 1$. The radius of curvature of the harmonic wavefront - in the source plane (R_0) - is then given by:[2]

$$R_0 = \pi \left\{ \frac{2\alpha\beta}{w(z)^2} \left[\frac{hc}{\kappa\lambda_0^2} - \frac{I_\mathrm{p}}{q\kappa\lambda_0} \right] + \frac{\lambda_0^2 z}{\pi w_0^2 w(z)^2} \right\}^{-1}. \tag{2.25}$$

The harmonic soure curvature shows only a very weak dependence on order. Rather it depends on α, which, to a good approximation, varies piecewise de-

[1] If the units of I_0 are W/cm^2 and λ_0 is in meters then $\kappa = 4.81 \times 10^{-20}$ cm^{2}W^{-1}m^{-2}.

[2] The subscript '0' here, and used throughout, denotes a quantity in the generation plane, a transverse section in the gas cell where the radiation may be thought of as originating from.

pending on whether the harmonic is in the plateau or cut-off spectral region [114]. In the plateau region α depends on the electron trajectory that gives rise to the harmonic emission, thus the long and short trajectories are expected to differ in their source plane curvature. It should also be noted that the under the right circumstances (specifically when $z < 0$), the two contributions the harmonic wavefront can be equal in magnitude but opposite in sign. In this situation the harmonic source is said to be planar: it has an infinite radius of curvature.

The harmonic source wavefront has been the subject of both theoretical [71] and experimental work [28]. Prior studies have concluded that, generally, HHG is produced with a wavefront of positive curvature (positive in the sense that the phase increases with transverse distance from the beam centre, or equally well, a surface of constant phase is concave with respect to the source). The intensity dependent phase term was identified as being most responsible for the overall wavefront shape [28]. Salieres et al. [71] noted that such a curved wavefront results in the 'apparent' harmonic source location (longitudinal position of flat phase and minimum transverse extent) appearing as though it is located before (upstream of) the generating medium. The size of such an effective source could be used as an estimate of the ultimate focusability of the harmonic beam.

2.4.1 The Harmonic Phase and Phase-matching

A key theoretical result which plays a central role in the current understanding of macroscopic features of HHG is found in the work of Balcou et al. [67]. In a study aimed at forging a better understanding the role of phase matching in high harmonic generation, the authors calculated the harmonic divergence and intensity

profile as a function of the longitudinal position of the gas medium relative to the laser focus. Interestingly, they found that when harmonic generation occurred before the laser reached its focus, when the driving wavefront is converging, a diverging harmonic wavefront was produced, with a complex and non-uniform intensity profile, see figure 2.5. Quite clearly there was little direct inheritance of the spatial properties from the driver beam to the harmonic field. The authors' explanation for such unintuitive behaviour was that the macroscopic response of the generating media and the collective emission of all atoms in the ensemble must be considered. Moreover, the intensity dependence of the phase of emission from each atom plays a central role in defining the spatial properties of HHG.

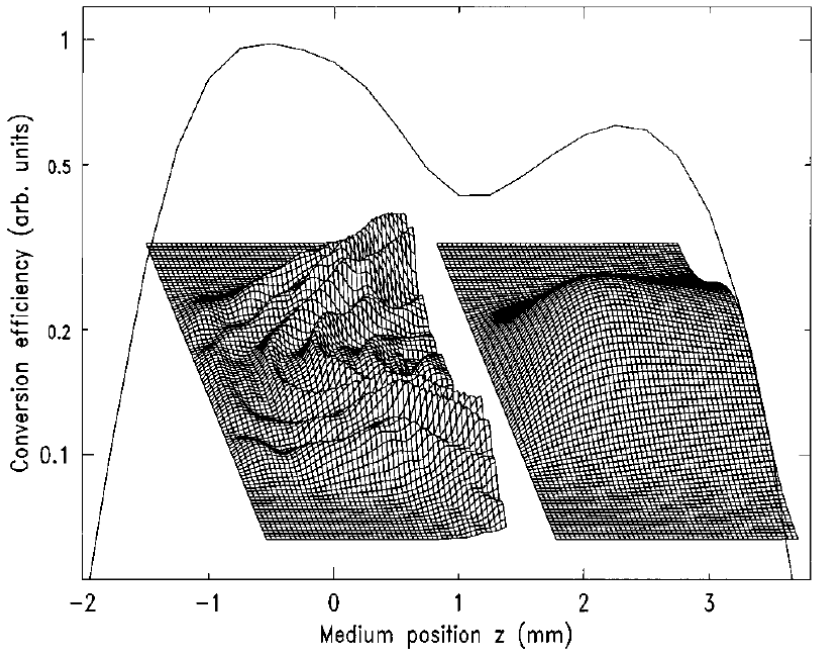

Figure 2.5: The conversion efficiency of harmonic emission as a function of z is shown by the black line. The 3D plots show the calculated (near-field) harmonic beam profile, generated before (left) and after (right) the laser focus (located at $z = 0$ here). Figure taken from [67].

2.5 Early HHG Studies

In the time since the first demonstration of high harmonic generation by Macpherson et al. [16] there have been a number of landmark studies which have focussed on improving our understanding of the spatial properties of the emission. Given ideal experimental conditions one might reasonably expect the spatial properties of HHG beam to not differ wildly from those of the parent laser. Such an assumption is often found true in the perturbative regime typical for second harmonic generation from crystals, see for instance [1]. However, numerous studies show that high harmonics, whether in their transverse intensity profile, wavefront or spatial coherence, can differ, sometimes acutely, from those of the driving beam.

A study by Tisch et al.[52], in which harmonics were generated in helium by 1 ps long pulses from a Nd:Glass laser, showed that the harmonic intensity profile can have a complex, non-uniform shape. In the plateau spectral region the beam profile differed drastically from that of the parent laser, narrowing to a more uniform, Gaussian-like shape in the cut-off. They attributed the complex harmonic beam shape to the deleterious effect of excessive ionization in the medium. In the same year as the study of Tisch et al., Salieres et al. [70] performed similar measurements using 140 fs duration pulses from a Cr:LiSaf laser system. They corroborated the conclusions of the earlier study when finding the harmonic transverse intensity profile was near Gaussian in shape when driven by the shorter pulses of their system. The reduction in pulse duration reduced the degree of ionization and hence reduced the distortion of the transverse profile of the harmonics from that of the driving beam. The work of Salieres et al. served to cement the idea that high harmonics could be generated in a confined, low

divergence beam with good spatial quality.

Researchers recognised early on that HHG held the prospect of providing a coherent source of XUV radiation. The observation of low divergence light, although not a sufficient condition [9], is indicative of light possessing good spatial coherence. The first experimental study probing this quality in HHG was by Ditmire et al. [85]. They related the visibility (modulation depth) of interference patterns formed from illumination of a double slit to the harmonic spatial coherence,[1] in a set-up reminiscent of the pioneering work of Young [125]. They found that the HHG beam showed good spatial coherence (visibility > 0.5) over the most of the transverse extent, although the fringe visibility could be reduced by increasing the driving laser intensity. The attributed this effect to the increased presence of free electrons, produced through ionization, in the medium. In addition the spatial coherence was always lower than that of the fundamental beam. A more detailed discussion of this point, and the phenomenon of spatial coherence in HHG, may be found in later chapters.

[1] See section 3.1.3 for more detail on this point.

Chapter 3

Characterizing Light

Characterization, at least within the realm of physics, refers to the process of performing a measurement to quantify a particular property, or set of properties, of an object. In the field of laser physics, the characterization of light has provided landmarks by which we may judge the state of the art. The constant forward march of improved performance from sources of radiation has provided a driving force in a number of emerging scientific fields, enabling researchers to build an ever improving understanding of physics through the use of an appropriate and well optimised probe. The modelling of the behaviour of light, whether in its propagation, reflection, diffraction or absorption by matter relies on accurate information of the initial state of the radiation. The interpretation of experimental data and the construction of experimental beamlines are two generic situations which benefit from having a well characterized radiation source. It is therefore of paramount importance that techniques are developed that provide accurate and reliable information of relevant properties for immediate use.

3.1 Properties of Interest

Before engaging in a discussion of characterization it is worthwhile identifying which aspects of light are experimentally feasible to measure and why such properties are of interest. Conventionally, the electric field of a pulsed beam[1] of radiation, propagating in the z-direction, with transverse extent in the x and y directions, may be formed from the product of two functions:

$$E_T(x, y, z, t) = \mathcal{E}_s(x, y, z)\mathcal{E}_t(t) \tag{3.1}$$

where $\mathcal{E}_s$ encodes the spatial properties and $\mathcal{E}_t$ the temporal. This assumption has been shown to be insufficient in the case of ultrafast pulses in a number of situations, where so called 'space-time coupling' is observed [79], however, for the sake of simplicity, at this stage of the discussion at least, we will continue to treat the spatial and temporal properties as distinct.[2]

3.1.1 Temporal Properties

When using light to probe a system, it is the pulse duration which defines the time scale of the phenomenon which may be studied. Pulsed light may be thought of as being composed of a real envelope function A_t modulated by a fast carrier wave:

$$\mathcal{E}_t(t) = A_t(t)\exp\{i[\Phi_t(t) + \omega_0 t]\} \tag{3.2}$$

[1] A beam refers to a field where the intensity is confined to close to the propagation axis (z here), with small angular divergence.

[2] For the interested reader, a brief exposition on space-time coupling in ultrafast pulses is found in Appendix B.

where ω_0 is the angular frequency and $\Phi_t(t)$ the temporal phase. For now we only consider the field at fixed spatial location. For light in the visible spectrum a single oscillation of the electric field lasts just a few femtoseconds[1] and is too fast to be measured directly. Knowledge of the pulse duration is gained from measuring the temporal extent (or duration) of A_t, but true characterization of the field requires extraction of the temporal phase (Φ_t) as well.

It is often convenient to treat the optical pulse in terms of its spectrum. To do so, we Fourier transform equation 3.2:

$$\mathcal{E}_\omega(\omega) = A_\omega \exp[-i\Phi_\omega(\omega_0 - \omega)] \tag{3.3}$$

where A_ω is related to the pulse spectrum ($S(\omega) = \langle|A_\omega|^2\rangle$), angled brackets indicate a time average and Φ_ω is the spectral phase. The negative frequency components are neglected for brevity. The spectral behaviour of a pulse may be modified by propagation through a dispersive, linear medium:

$$\mathcal{E}_{\text{out}} = \mathcal{E}_{\text{in}} T(\omega) \exp[-i\Phi_{\text{mat}}(\omega_0 - \omega)] \tag{3.4}$$

where $T(\omega)$ is the *amplitude* transmission function of the medium and is often equal to 1 and Φ_{mat} is the added spectral phase coming from dispersion. The spectral phase may be expressed in terms of its Taylor series:

$$\Phi_{\text{mat}}(\omega) = \Phi_0 + \Phi_1(\omega - \omega_0) + \Phi_2\frac{(\omega - \omega_0)^2}{2} + \Phi_3\frac{(\omega - \omega_0)^3)}{6}... \tag{3.5}$$

[1] 2.66 fs for λ=800 nm light.

where:

$$\Phi_i = \frac{\partial^i \Phi_{\text{mat}}}{\partial \omega^i}|_{\omega_0} \tag{3.6}$$

and $i = 0, 1, 2, 3...$. The first term in equation 3.5 corresponds to a phase offset. The second gives rise to a delay of the whole laser pulse. The third is known as the group delay dispersion (GDD), leading to a frequency dependent delay during the temporal extent of the pulse. The fourth is referred to as third order dispersion (TOD) and gives rise to a quadratic phase variation across the pulse. GDD and TOD (as well as higher order terms) lead to the changes in the duration of a pulse without corresponding changes to the pulse spectrum. This idea is exploited in chirped pulse compression, where GDD is added to a pulse to stretch it before amplification and removed afterward in order to recompress the pulse.

3.1.2 Spatial Properties

This thesis is concerned almost exclusively with characterizing and understanding the spatial properties of short-wavelength light. The spatial part of the electric field (at an instant in time) can be written as:

$$\mathcal{E}_s(x, y, z) = A_s(x, y, z)\exp\Big\{i[\Phi_s(x, y, z) + kz]\Big\} \tag{3.7}$$

where A_s is a (real) function which corresponds to the transverse extent of the field at a particular longitudinal position z and Φ_s is the spatial phase. The time

integrated intensity is given by:

$$I(x, y, z) = \langle |E_T(x, y, z, t)|^2 \rangle \tag{3.8}$$

where the angled brackets denote a time-average.[1] Detectors, such as CCDs and MCPs, are sensitive to the (time integrated) beam intensity, rather than the electric field itself. The variation in intensity with transverse coordinate is often referred to as the intensity/irradiance profile or distribution (profile for a 1-D transverse lineout, distribution for a 2-D transverse slice). If the detector is placed many Rayleigh lengths away from the source, it may be assumed that the field's transverse width increases linearly with position from the source location, and it is possible to calculate the divergence from the measured beam size.

The variation in spatial phase with transverse coordinate is often referred to as the spatial phase distribution. The beam wavefront is a surface of constant phase. A point source emitting radiation isotropically possesses a spatial phase of the form:

$$\Phi_{\text{point}}(r, z) = \frac{kr^2}{2z} \tag{3.9}$$

where r is the radial coordinate. Although, generally speaking, detectors are insensitive to the phase properties of light, a number of methods have been developed to perform an accurate measurement of this quantity. Those applicable in the XUV and SXR spectrum, directly relevant to the task of characterizing HHG, are outlined in section 3.4.1.

[1] Strictly speaking, there is a proportionality constant between the left and right hand sides of equation 3.8 which is omitted here. For SI units, and propagation in vacuum, this constant is equal to $\frac{1}{2}c\epsilon_0$.

3.1.2.1 Example: The Gaussian Beam

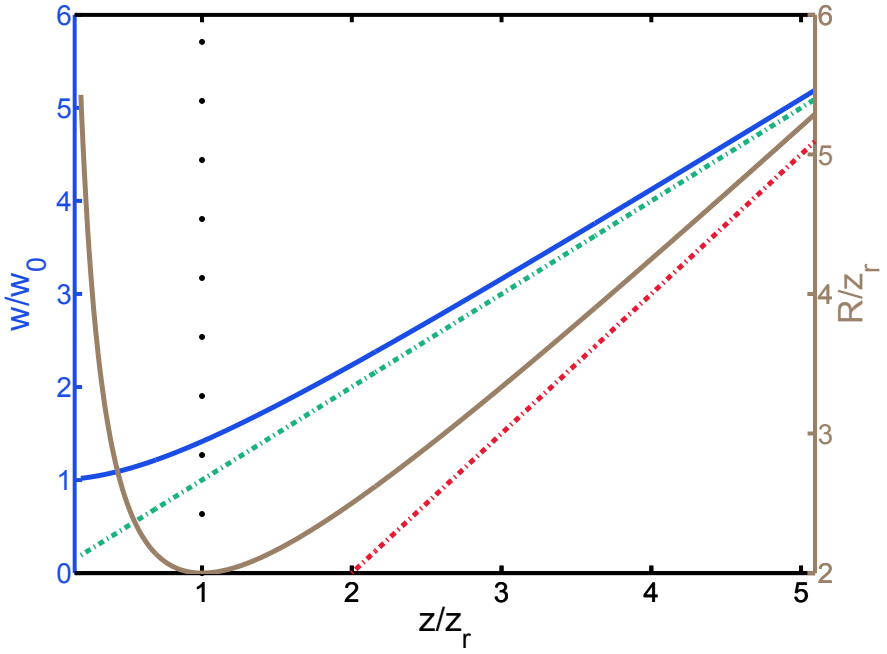

Figure 3.1: Beam diameter (blue line) and radius of curvature (brown line) both plotted as a function of longitudinal position (normalised to the Rayleigh range) for a Gaussian beam with a waist at $z = 0$. Here $\lambda = \frac{w_0}{5}$. The green and red dash-dotted lines show the asymptotic ($\lim z \to \infty$) behaviour of beam diameter and radius of curvature respectively.

The Gaussian beam (a field with an intensity distribution shaped like a Gaussian function) is a common description for the output of most optical lasers. It also offers a convenient example for understanding the way the spatial properties light change with propagation. We start by considering a beam propagating in the z direction with extent in one transverse dimension, x. The beam at a longitudinal position $z = 0$, is given by:

$$E(x, z = 0) = E_0 \exp\left[\frac{-x^2}{w_0^2}\right] \tag{3.10}$$

where E_0 is the electric-field magnitude and the full width at half maximum (FWHM) of the beam is given by $2\sqrt{\ln(2)}w_0$. Solving the paraxial wave equation for a field of this form yields a beam which maintains a Gaussian shape throughout propagation. Specifically:

$$E(x,z) = E_0 \exp\left[\frac{-x^2}{w(z)^2}\right] \exp\left[i\Phi_s(z)\right] \tag{3.11}$$

where $w(z)$ is the beam width and $\Phi_s(z)$ is the spatial phase:

$$w(z) = w_0\sqrt{1+\frac{z^2}{z_r^2}} \tag{3.12}$$

$$\Phi_s(z) = \frac{kx^2}{2R(z)} \tag{3.13}$$

where:

$$z_r = \frac{\pi w_0^2}{\lambda} \tag{3.14}$$

$$R(z) = z\left(1+\frac{z_r^2}{z^2}\right) \tag{3.15}$$

are the Rayleigh range and beam radius of curvature, respectively. Far from the source location, where $z \gg z_r$ is well satisfied, the beam width and radius of curvature may be approximated by:

$$w(z) \simeq \frac{\lambda z}{\pi w_0} \tag{3.16}$$

$$R(z) \simeq z \tag{3.17}$$

i.e. both quantities increase linearly with propagation distance. The longitudinal

variation of the beam width and wavefront curvature are shown in figure 3.1 for a spot size five times larger than the wavelength.

The propagation characteristics of a Gaussian beams serve as a useful example for comparison with more complicated sources of radiation. It should be noted that for the case outlined above, the field is implicitly assumed to be fully spatially coherent. More generalised models of light propagation have shown the state of coherence can play an important role in governing, for instance, the beam divergence [8].

3.1.3 Spatial Coherence

So far we have limited the discussion to pulse temporal properties at a specific spatial location, or the spatial properties at an instant of time. Coherence cannot be framed from either perspective. In essence, we wish to compare field oscillations potentially separated in both space and time, specifically commenting on how well correlated the oscillations are. As we will see, correlation, in the optical sense, is mathematically similar to the concept of covariance found in the field of statistics. It is then by no means surprising to find that a statistical picture of light [4, 98] leads to an intuitive understanding of what coherence means in the context of optical phenomena.

Here we summarise the approach of Born and Wolf [4]. We begin by considering an electric field with transverse extent in one spatial dimension: $E(x,t)$. Strictly, $E(x,t)$ should be an ergodic and stationary function [4], which, for all practical purposes, is equivalent to assuming that the average properties of $E(x,t)$ do not change over time. We wish to measure the degree of correlation of the field

measured at two (spatially separated) test points located at $x = x_1$ and $x = x_2$, delayed in time by τ. To do so we define the mutual coherence function (MCF) $\Gamma(x_1, x_2, \tau)$, in a similar vein to the covariance function in statistics:

$$\Gamma(x_1, x_2, \tau) = \langle E(x_1, t+\tau)E(x_2, t)^* \rangle \tag{3.18}$$

where the angled brackets indicate a time average as in equation 3.8. In fact, setting $\tau = 0$, and making reference to 3.8, it can be shown the intensity may be derived from the MCF:

$$\Gamma(x_1, x_1, 0) = \langle E(x_1, t)E(x_1, t)^* \rangle = I(x_1) = I_1 \tag{3.19}$$

where we use I_1 to indicate the (time integrated) intensity evaluated at location x_1. Since we are primarily concerned with spatial coherence, that is the degree of correlation between two spatially separate locations at equal time ($\tau = 0$), we will continue without making further reference to τ.[1] The MCF evaluated at $\tau = 0$ is referred to as the mutual intensity (J_{12}), where the subscripts identify J_{12} with points x_1 and x_2. Normalisation of the mutual intensity gives the complex coherence factor (CCF) μ_{12}:

$$\mu_{12} = \frac{J_{12}}{\sqrt{J_{11}J_{22}}} = \frac{J_{12}}{\sqrt{I_1 I_2}}. \tag{3.20}$$

Through application of the Schwarz inequality it is possible to show that μ must

[1] $\Gamma(x, x, \tau)$, the MCF evaluated when $x_1 = x_2 = x$ but $\tau \neq 0$, is the quantity of interest when considering the temporal coherence of light.

be bounded:

$$0 \leq |\mu| \leq 1. \tag{3.21}$$

When $|\mu| = 1$ the wave has perfect spatial coherence. Conversely, when $|\mu| = 0$, there is no correlation present in the oscillations between the two locations and we may treat the light as incoherent.

One of the most widely studied manifestations of spatial coherence is found in the interference fringes formed by illumination of a pinhole pair, as originally considered by Young [125]. We locate the pinholes at $x = x_1$ and $x = x_2$ respectively. The pinholes lie on the plane denoted by σ_1. We will neglect any interference in the transverse dimension orthogonal to x. The resultant inference pattern is measured on a detector lying on a plane denoted by σ_2. The distance separating σ_2 and σ_1 is z. We consider the case where z is large enough to place σ_2 in the 'far-field'[1] of light originating from pinholes on σ_1 such that interference effects may be detected. Such an arrangement, is shown in figure 3.2. The electric field at a point X on σ_2 is given by:

$$E(X,t) = K_1 E(x_1,t) + K_2 E(x_2,t) \tag{3.22}$$

where K_i is a (generally complex) function which deals with the propagation of the field from the pinhole located at position x_i to the point on the detector, denoted by X.

[1]Far-field may be defined as longitudinal distances satisfying $z \gg \frac{\pi a^2}{\lambda}$, where a is the aperture diameter.

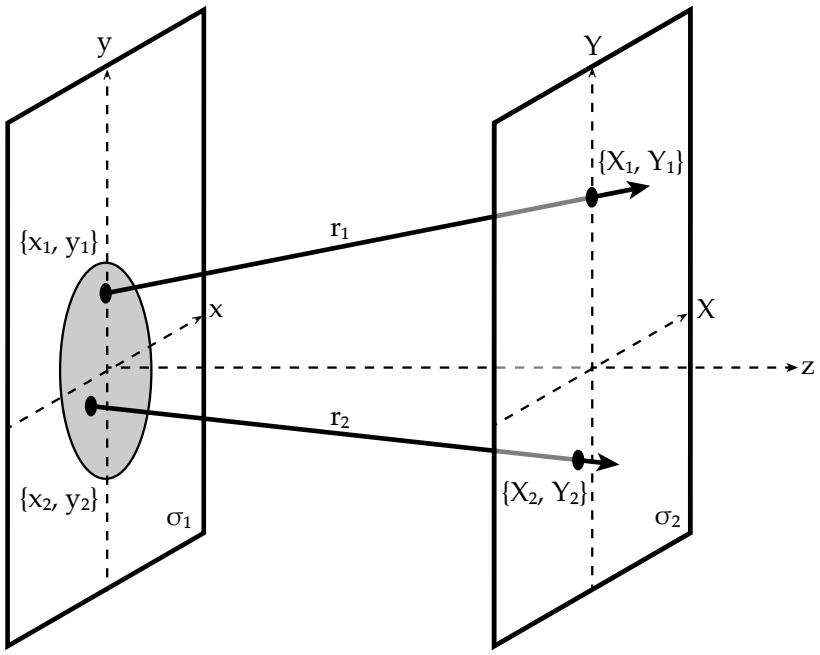

Figure 3.2: Diagram depicting the relevant geometry for describing beam propagation. Braces enclose coordinates of points on the respective 2-D planes, σ_1 and σ_2. In this section and beyond the discussion is limited to a single transverse dimension (x on σ_1 and X on σ_2).

The detector lying on σ_2 records intensity:

$$\begin{aligned} I(X) &= \langle |E(X,t)E(X,t)^*|^2 \rangle \\ &= \langle |K_1 E(x_1,t)|^2 \rangle + \langle |K_1 E(x_2,t)|^2 \rangle + 2\Re[K_1 K_2 \langle E(x_1,t)E(x_2,t)^* \rangle] \\ &= |K_1|^2 I_1 + |K_2|^2 I_2 + 2\Re[K_1 K_2 \Gamma(x_1,x_2)] \\ &= I^{(1)} + I^{(2)} + 2\Re[K_1 K_2 J_{12}] \end{aligned} \tag{3.23}$$

where $\Re[...]$, indicates the real part of the function enclosed by the square brackets and $I^{(i)}$ is the intensity reaching the detector from pinhole i alone. Making use of equation 3.20, we may then write what is called the *general interference law for stationary optical fields*:

$$I(X) = I^{(1)} + I^{(2)} + 2\sqrt{I^{(1)} I^{(2)}}\mu^{(r)}(x_1,x_2) \tag{3.24}$$

where $\mu^{(r)} = \Re[\mu]$. The law may also be expressed as:

$$I(X) = I^{(1)} + I^{(2)} + 2\sqrt{I^{(1)} I^{(2)}}|\mu(x_1,x_2)| \cos[\theta - k(r_2 - r_1)] \tag{3.25}$$

without loss of generality, where θ is the phase of the CCF and r_i is the distance between x_i and X. The maximum and minimum values of 3.25 are respectively:

$$I_{\max} = I^{(1)} + I^{(2)} + 2\sqrt{I^{(1)} I^{(2)}}|\mu(x_1,x_2)| \tag{3.26}$$

$$I_{\min} = I^{(1)} + I^{(2)} - 2\sqrt{I^{(1)} I^{(2)}}|\mu(x_1,x_2)|. \tag{3.27}$$

Since we are considering the case of a two-pinhole interferometer, it is useful to quantify the modulation depth of fringes that may arise. Specifically, the *visibility*

(V) of an interference pattern is given by:

$$\mathcal{V} = \frac{I_{\max} - I_{\min}}{I_{\max} + I_{\min}} = \frac{2\sqrt{I^{(1)}I^{(2)}}}{I^{(1)} + I^{(2)}}|\mu(x_1, x_2)| \tag{3.28}$$

In the case where both pinholes are illuminated by coherent light of equal intensity ($I^{(1)} = I^{(2)}$) the visibility attains its maximum value of unity and the depth of modulation in the observed pattern is maximised. In the case of incoherent illumination $|\mu| = 0$, the visibility is also zero and the interference fringes wash out. Example interference patterns for two cases (coherent illumination and partially coherent illumination) are shown in figure 3.3.

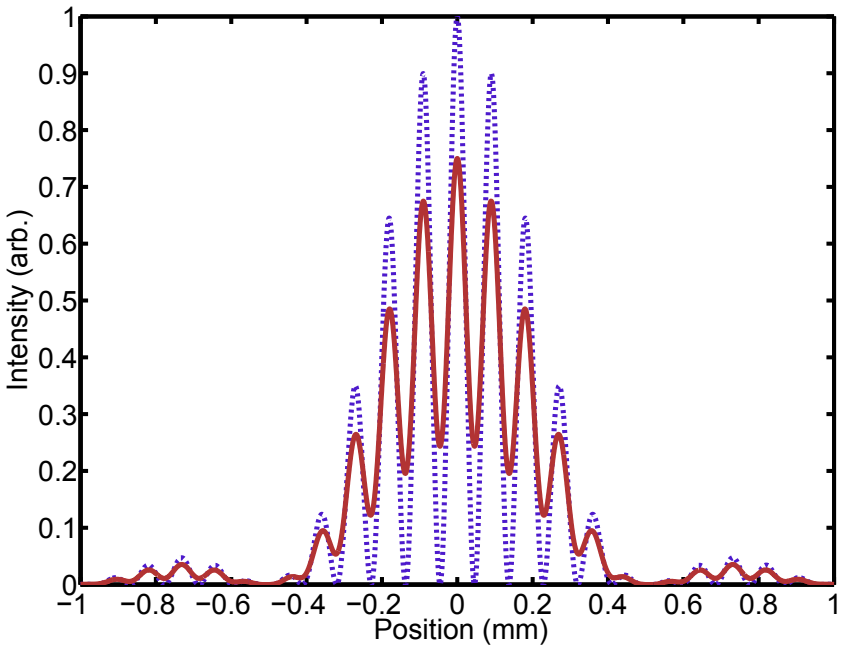

Figure 3.3: Calculated interference fringes for light of wavelength of 32 nm impinging on 20 μm wide pinholes separated by 250 μm, recorded 1 m downstream for the case of coherent light (blue dotted line) and partially coherent light (red solid line).

It seems natural to use the fringe visibility as the principal metric for measuring the spatial coherence of light with equation 3.28 establishing the relationship between $\mathcal{V}$ and $|\mu|$. The same equation also describes how fully coherent illumination will produce less than unity fringe visibility in the case where the intensity falling on each pinhole is not equal. Therefore, care must be taken to either maintain even illumination or have good knowledge of the beam intensity in order for the CCF to be measured accurately using a two-pinhole interferometer.

As a further note, it is worth drawing attention to the fact that the discussion has been limited to the scalar definition of light: polarization effects have been neglected. If a beam were to possess a spatially dependent polarization one would expect the fringe visibility to be reduced, even for interference from pinholes illuminated evenly by spatially coherent light. This subtlety has been considered recently by Singh et al. who derived a vectoral generalisation to the Van Cittert-Zernike theorem [75] (section 3.2.1 details the scalar version of this theory).

3.2 Theories of Spatial Coherence

The last century has seen numerous inroads made into improving our understanding of optical coherence. Such efforts have provided a firm basis for the exploitation of coherence in a variety of experimental settings. Theories quantifying the origin and propagation of this spatial property have been developed providing a useful tool for the modelling of the behaviour of light.

3.2.1 Van Cittert-Zernike Theorem

A central theorem of statistical optics comes from the work of Pieter Hendrik van Cittert and Frits Zernike [7, 126, 127]. In a series of papers they independently derived an expression for the spatial coherence of radiation emitted by an extended, monochromatic, *incoherent* source.

Here the account given in [4] is followed. The source is assumed to be planar and lying in the plane σ_1, emitting radiation some distance to a second plane σ_2. It is composed of small,[1] radiating elements labelled δs_1, δs_2... The field reaching P_1, a point lying on σ_2 can be written as:

$$E(P_1, t) = \sum_m E_{m1}(t) \tag{3.29}$$

where $E_{m1}(t)$ is the field originating from radiating element δs_m. We may equally consider a second point on σ_2, P_2, and form the mutual intensity function evaluated on σ_2:

$$J_{12} = \langle E(P_1, t)E^*(P_2, t)\rangle = \sum_m \langle E_{m1}(t)E^*_{m2}(t)\rangle + \sum_{m\neq n}\sum \langle E_{m1}(t)E^*_{n2}(t)\rangle. \tag{3.30}$$

The source is incoherent, hence radiation from spatially separated elements is not correlated:

$$\langle E_{m1}(t)E^*_{n2}(t)\rangle = \langle E_{m1}(t)\rangle\langle E_{n2}(t)\rangle = 0 \quad \text{when } m \neq n \tag{3.31}$$

The contribution from a single element δs_m, a distance r_{m1} from position P_1 on

[1] Element sizes are smaller than the emitting radiation wavelength.

σ_2 can be written as:

$$E_{m1}(t) = A_m\Big(t - \frac{r_{m1}}{v}\Big)\frac{\exp[ik(r_{m1} - vt)]}{r_{m1}} \tag{3.32}$$

where A_m is the wave amplitude, v is the speed of light in the medium between σ_1 and σ_2 and k is the wavenumber. We may neglect the retardation in equation 3.32 provided the source is small compared to the separation of σ_1 and σ_2. An expression similar to equation 3.32 holds for $E_{m2}(t)$. The mutual intensity then takes the form:

$$J_{12} = \sum_m \langle A_m(t)A_m^*(t)\rangle \frac{\exp[ik(r_{m1} - r_{m2})]}{r_{m1}r_{m2}}. \tag{3.33}$$

Rather than treating the source as being formed of an array of discretised mutu-

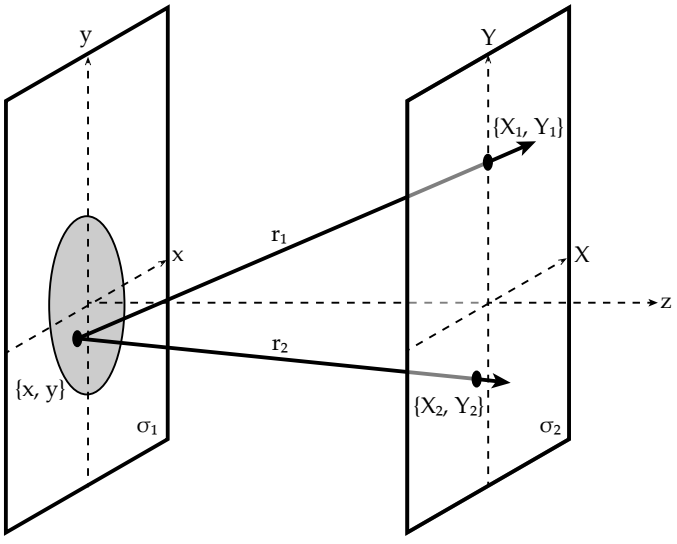

Figure 3.4: Diagram depicting the geometry relevant to the Van Cittert-Zernike theorem. The grey shaded area represents the incoherent radiation source.

ally incoherent sources, we may instead compose it of a continuum of infinitesimal elements:

$$J_{12} = \int_{\sigma_1} I(S) \frac{\exp[ik(r_1 - r_2)]}{r_1 r_2} \mathrm{d}S \tag{3.34}$$

where now r_i is the distances between a point on the source S and a point P_i on σ_2 (i=1,2) and $I(S)$ is the intensity per unit area. A diagram depicting the relevant quantities for the Van Cittert-Zernike theorem is shown in figure 3.4.

We are interested in the spatial coherence of light reaching σ_2. Equations 3.20 and 3.34 may be used to derive:

$$\mu(P_1, P_2) = \frac{J_{12}}{\sqrt{J_{11} J_{22}}} = \frac{1}{\sqrt{I(P_1) I(P_2)}} \int_{\sigma_1} I(S) \frac{\exp[ik(r_1 - r_2)]}{r_1 r_2} \mathrm{d}S. \tag{3.35}$$

Equation 3.35 bears a resemblance to the Huygens-Fresnel integral for diffraction. Inspired by this point, the Van Cittert-Zernike theorem states that the CCF (evaluated when P_1 is fixed and P_2 is allowed to vary) of an extended, monochromatic, incoherent source, can be found by evaluating the amplitude of a diffraction pattern, centred on P_2 but evaluated at P_1, of an aperture illuminated by a wave of amplitude the same as the *intensity* distribution of the incoherent source, with a wavefront converging on P_2.

As a further simplification, we may make the paraxial approximation, separating σ_2 and σ_1 by a distance far greater than source size. Under this approximation we may write:

$$r_1 - r_2 = \frac{(X_1^2 + Y_1^2) - (X_2^2 + Y_2^2)}{2R} - \frac{(Y_1 - Y_2)y + (X_1 - X_2)x}{Z} \tag{3.36}$$

where $\{X_1,Y_1\}$ and $\{X_2,Y_2\}$ correspond to points P_1 and P_2 and $\{x,y\}$ is a point on the source and Z is the separation between σ_1 and σ_2. This allows us to write:

$$\mu(P_1,P_2) = \frac{\exp(i\psi)\int\int I(x,y)\exp[\frac{-ik(x\Delta X+y\Delta Y)}{Z}]\mathrm{d}x\mathrm{d}y}{\int\int I(x,y)\mathrm{d}x\mathrm{d}y} \tag{3.37}$$

where $\Delta X = X_2 - X_1$, $\Delta Y = Y_2 - Y_1$ and the phase factor ψ is given by

$$\psi = \frac{k(X_1^2+Y_1^2)-(X_2^2+Y_2^2)}{2Z} \tag{3.38}$$

and we recognise the integral in the numerator as a Fourier transform over the incoherent source. This leads to an alternate phrasing of the Van Cittert-Zernike theorem. Namely, the CCF measured in the 'far-field' from a monochromatic, incoherent source is well approximated by the (normalised) Fourier transform of the intensity distribution of the source.

As an example, we consider a source comprised of a uniform disc of incoherent emitters of radius a such that:

$$\begin{aligned} I(x,y) = 1 \quad \text{when} \quad \sqrt{(x^2+y^2)} < a \\ \text{and} \\ I(x,y) = 0 \quad \text{otherwise.} \end{aligned} \tag{3.39}$$

Evaluating equation 3.37 leads to:

$$|\mu|_{\text{disc}} = |\frac{2B_1(\nu)}{\nu}| \tag{3.40}$$

where B_1 is the Bessel function of the first kind, first order and $\nu = \frac{ka}{Z}\Delta P$,

where ΔP is the separation of two test points on σ_2. Equation 3.40 shows that the CCF of radiation from an incoherent disc-shaped source possesses a finite degree of coherence, starting at unity for two coincident points and monotonically decreasing to zero when $\nu = 3.83$. Furthermore, the CCF depends on only the separation of two test points on σ_2 and not on their actual location. This property is known as *shift invariance*.

The spatial coherence can be further quantified by defining the coherence area A_c:

$$A_c = \int\int |\mu| \, \mathrm{d}\Delta x \, \mathrm{d}\Delta y \tag{3.41}$$

where $\Delta x = x_2 - x_1$ and $\Delta y = y_2 - y_1$. For an incoherent disc of radius a we find:

$$A_c = \frac{\lambda^2 Z^2}{\pi a^2} \tag{3.42}$$

or, in other words, the radius of the coherence area increases linearly with distance from the source Z.

3.2.2 The Generalised Van Cittert-Zernike Theorem

In section 3.2.1 we considered the spatial coherence of radiation produced by an incoherent source. The theorem is not applicable to sources possessing partial spatial coherence. An incoherent source emits radiation isotropically, however a great many short-wavelength radiation sources, including HHG, synchrotrons and FELs, produced beamed (low divergence) radiation, implying a certain degree of coherence in the source [99].

Here we will recount work summarised by Goodman [98] in formulating a more generalised version of the Van Cittert-Zernike Theorem, one which defines the spatial properties of radiation from a class of sources characterized by the source CCF and intensity distribution. For the sake of brevity only one transverse spatial dimension is considered. As with the derivation of the Van Cittert-Zernike theorem, we consider a source lying on a plane σ_1, now with transverse extent in the x dimension, emitting radiation to a plane σ_2, some distance z away. The transverse dimension of σ_2 is denoted by X. We limit ourselves to considering (planar) sources which are characterized by a mutual intensity function of the form:

$$J_0(x_1, x_2) = \sqrt{I_0(x_1) I_0(x_2)}\mu_0(x_2 - x_1) \tag{3.43}$$

where the '0' subscript explicitly denotes a property of the source and, as before, I and μ are the intensity and CCF respectively. A source with a mutual intensity function of this form is known as 'quasi-homogeneous'. As with the spatial coherence of radiation from an incoherent source, the CCF of a quasi-homogeneous source is shift invariant. A further simplification can be made by assuming that any structures in the spatial properties of the source are coarse in relation to the source's gross size, specifically:

$$J_0(x_1, x_2) \cong I_0(\bar{x})\mu_0(\Delta x) \tag{3.44}$$

where the new variables are $\Delta x = x_2 - x_1$ and $\bar{x} = \frac{x_2 + x_1}{2}$. It can be shown [98] that for sources of this type the mutual intensity is propagated using a similar

equation to that related to the Fresnel-Huygen's integral:

$$J_p(X_1, X_2) = \frac{1}{(\lambda z)^2} \int \int J_0(x_1, x_2) \exp[-ik(r_2 - r_1)] \mathrm{d}x_1 \mathrm{d}x_2 \tag{3.45}$$

where r_i is the distance between points x_i and X_i. We again make the paraxial approximation, as in section 3.2.1, to address the exponential factor in equation 3.45:

$$\begin{aligned} r_2 - r_1 &\cong \frac{1}{2z}(X_2^2 - X_1^2 + x_2^2 - x_1^2 - 2X_2x_2 + 2X_1x_1) \\ &= \frac{1}{2z}\Big[\bar{X}\Delta X + \bar{x}\Delta x - \Delta X\bar{x} - \bar{X}\Delta x\Big] \end{aligned} \tag{3.46}$$

where $\Delta X = X_2 - X_1$ and $\bar{X} = \frac{X_2 + X_1}{2}$. Thus we may write:

$$\begin{aligned} J_p(X_2, X_1, z) = \frac{1}{(\lambda z)^2} \int \int J_0(x_1, x_2) \\ \exp\Big\{ - i\frac{k}{2z}\Big[(X_2 - x_2)^2 - (X_1 - x_1)^2\Big]\Big\} \mathrm{d}x_1 \mathrm{d}x_2 \end{aligned} \tag{3.47}$$

or equally well:

$$\begin{aligned} J_p(X_2, X_1, z) = \frac{\exp[-i\Psi]}{(\lambda z)^2} \int \int J_0(x_1, x_2) \exp\Big[- i\frac{k}{2z}(x_2^2 - x_1^2)\Big] \\ \exp\Big[- i\frac{k}{z}(X_2x_2 - X_1x_1)\Big] \mathrm{d}x_1 \mathrm{d}x_2 \end{aligned} \tag{3.48}$$

where $\Psi = \frac{k(X_2^2 - X_1^2)}{2z}$. The form of equation 3.47 indicates that, under the paraxial approximation, the mutual intensity function can be propagated using a Fresnel

transform. It can be written in the more compact form:

$$J_p(X_2, X_1, z) = \frac{\exp[-i\Psi]}{(\lambda z)^2}\mathcal{F}\Big[J_0(x_1, x_2)\Big] * \mathcal{F}\Big\{\exp\Big[\frac{ik}{2z}(x_1^2 - x_2^2)\Big]\Big\} \tag{3.49}$$

where $*$ indicates the convolution operation.

The propagated CCF and intensity profile are recovered from J_p through the use of equations 3.20 and 3.19 respectively. Thus, equations 3.47, 3.48 and 3.49 all are expressions for a Van Cittert-Zernike theorem generalised for quasi-homogeneous, partially coherent sources. If the intensity profile and CCF are known at one transverse plane, the generalised theorem allows same quantities to be calculated at any other transverse plane.

If the condition $z > 4\frac{\bar{x}\Delta x}{\lambda}$ is fulfilled we may readily drop the terms containing x_2^2 and x_1^2 in equation 3.46. This process is analogous to discarding the 'Fresnel' term when performing an approximate calculation of the pattern formed from light diffracting from an aperture. Here it enables us to write the relationship between source and propagated properties in terms of Fourier transforms. Substituting into equation 3.45, and changing the variables of integration, gives:

$$\begin{aligned} J_p(X_2, X_1) &= \frac{\mathrm{e}^{-i\psi}}{(\lambda z)^2}\int I_0(\bar{x})\exp\Big[\frac{ik}{z}\Delta X\bar{x}\Big]\mathrm{d}\bar{x} \times \\ &\qquad \int \mu_0(\Delta x)\exp\Big[\frac{ik}{z}\Delta x\bar{X}\Big]\mathrm{d}\Delta x \\ &= \frac{\mathrm{e}^{-i\psi}}{(\lambda z)^2}\mathcal{F}\Big[I_0(\bar{x}), \frac{k\Delta X}{z}\Big]\mathcal{F}\Big[\mu_0(\Delta x), \frac{k\bar{X}}{z}\Big] \end{aligned} \tag{3.50}$$

where $\psi = \frac{k}{z}\bar{X}\Delta X$ and $\mathcal{F}[g(y), k_y]$ denotes the Fourier transform of function $g(y)$

from the domain y to k_y. The propagated intensity is then given by:

$$I_p(X) = J_p(X, X) = \frac{1}{(\lambda z)^2}\mathcal{F}\Big[\mu_0(\Delta x), \frac{kX}{z}\Big] \tag{3.51}$$

and the CCF by

$$\mu_p(\Delta X) = \frac{J_p(X_2, X_1)}{I_p(\bar{X})} = \mathrm{e}^{-i\psi}\mathcal{F}\Big[I_0(\bar{x}), \frac{k\Delta X}{z}\Big] \tag{3.52}$$

where we note that, within the stated assumptions, the propagated intensity depends only on the source spatial coherence, while the propagated CCF depends only on the source intensity profile (as per the original Van Cittert-Zernike theorem described in section 3.2.1).

The main result of section 3.2.1 can be derived as a limiting case of equation 3.47. The CCF of an incoherent source can be expressed as a Dirac delta function:

$$\mu_{\text{inc}} = \delta(\Delta x) \tag{3.53}$$

Substituting into equation 3.47 we obtain:

$$J_p(X_2, X_1) = \frac{e^{-i\psi}}{(\lambda z)^2}\int I_0(\bar{x})\exp\Big[\frac{ik}{z}\Delta X\bar{x}\Big]\mathrm{d}\bar{x} \tag{3.54}$$

and for the CCF:

$$\mu_p(\Delta X) = \frac{e^{-i\psi}}{(\lambda z)^2}\frac{\int I_0(\bar{x})\exp\Big[\frac{ik}{z}\Delta X\bar{x}\Big]\mathrm{d}\bar{x}}{I_{\text{ic}}(\bar{X})} \tag{3.55}$$

which, up to a coordinate transform, is the same result as in equation 3.37.

3.2.3 Gaussian-Schell Model

The generalised Van Cittert-Zernike theorem described in section 3.2.2 provides a firm basis for understanding the propagation of partially coherent light. However, there are very few choices of source shape and coherence which provide analytic expressions for the propagated intensity and CCF. An exception is the class of sources with an intensity distribution and CCF both of Gaussian form. Their propagation characteristics are governed by the so called 'Gaussian-Schell Model' ([119] and references therein), which provides a useful, analytically tractable, example of how the propagated spatial properties depend on those of the source.

We begin by considering a quasi-homogeneous source (with transverse extent in the x dimension) with an intensity profile and CCF given by:

$$\begin{aligned} I_0(x_i) &= \exp\left[\frac{-x_i^2}{2w_{0\mathrm{I}}^2}\right] \\ \mu_0(x_2, x_1) &= \exp\left[\frac{-(x_2 - x_1)^2}{2w_{0\mathrm{C}}^2}\right] \end{aligned} \tag{3.56}$$

where $w_{0\mathrm{I}}$ and $w_{0\mathrm{C}}$ are the widths of the source intensity profile and CCF respectively and $i \in \{1, 2\}$. We introduce a joint source diameter w_{IC}, which will prove algebraically convenient further on:

$$\frac{1}{w_{\mathrm{IC}}^2} = \frac{1}{(2w_{0\mathrm{I}})^2} + \frac{1}{w_{0\mathrm{C}}^2}. \tag{3.57}$$

The source mutual intensity (J_0) is propagated using equation 3.47 giving rise to an analytic expression for the mutual intensity measured some distance z from

the source:

$$J_p(X_1, X_2, z) = \frac{1}{D(z)}\exp[i\psi]\exp\Big[\frac{-(X_2 + X_1)^2}{8w_{\mathrm{I0}}^2 D(z)^2}\Big]\exp\Big[\frac{-(X_2 - X_1)^2}{8w_{\mathrm{IC}}^2 D(z)^2}\Big] \quad (3.58)$$

where

$$D(z) = \Big[1 + \Big(\frac{z}{z_{\mathrm{eff}}}\Big)^2\Big]^{\frac{1}{2}} \quad (3.59)$$

is known as the expansion coefficient and $\psi(z) = \frac{k(x_2^2 - x_1^2)}{2R(z)}$ is a phase factor and $R(z)$ is the wavefront radius of curvature:

$$R(z) = z\Big[1 + \Big(\frac{z_{\mathrm{eff}}}{z}\Big)^2\Big] \quad (3.60)$$

where z_{eff} may be thought of as an effective Rayleigh range:

$$z_{\mathrm{eff}} = k w_{0\mathrm{I}} w_{\mathrm{IC}}. \quad (3.61)$$

The propagated intensity profile is found from J_p through:

$$I_p(X) = J_p(X, X) = \frac{1}{D(z)}\exp\Big[\frac{-X^2}{2W_{\mathrm{pI}}^2(z)}\Big] \quad (3.62)$$

where W_{pI} is the propagated intensity width, given by:

$$W_{\mathrm{pI}}(z) = w_{0\mathrm{I}} D(z) = (w_{0\mathrm{I}}^2 + \Theta_{\mathrm{I}}^2 z^2)^{\frac{1}{2}} \quad (3.63)$$

and Θ_{I} is the effective intensity angular divergence:

$$\Theta_I = \frac{1}{2kw_{0\mathrm{C}}}(4 + q_{\mathrm{IC}}^2)^{\frac{1}{2}} \tag{3.64}$$

and q_{IC} is the 'coherent fraction':

$$q_{\mathrm{IC}} = \frac{w_{0\mathrm{C}}}{w_{0\mathrm{I}}} \tag{3.65}$$

a convenient measure of how coherent the source is: the larger the coherent fraction, the higher the spatial coherence over the central (most intense) part of the source. In a more practical sense, a beam with excellent coherence over its entire transverse extent may be required, so placing the coherence width into context with the intensity width, as it is for the coherent fraction, is important.

The propagated CCF is derived from J_p:

$$\begin{aligned}\mu_p(X_1, X_2, z) &= \frac{J_p(X_2, X_1)}{\sqrt{J_p(X_2, X_2)J_p(X_1, X_1)}} \\ &= \exp[i\psi]\exp\Big[\frac{-(X_2 - X_1)^2}{2W_{\mathrm{pC}}^2(z)}\Big]\end{aligned} \tag{3.66}$$

where W_{pC} is the width of the propagated CCF and is given by:

$$W_{\mathrm{pC}} = w_{0\mathrm{C}}D(z) = (w_{0\mathrm{C}}^2 + \Theta_{\mathrm{C}}^2 z^2)^{\frac{1}{2}} \tag{3.67}$$

where Θ_{C} may be thought of as the angular width of the CCF:

$$\Theta_{\mathrm{C}} = \frac{1}{2kw_{0\mathrm{I}}}(4 + q_{\mathrm{IC}}^2)^{\frac{1}{2}} \tag{3.68}$$

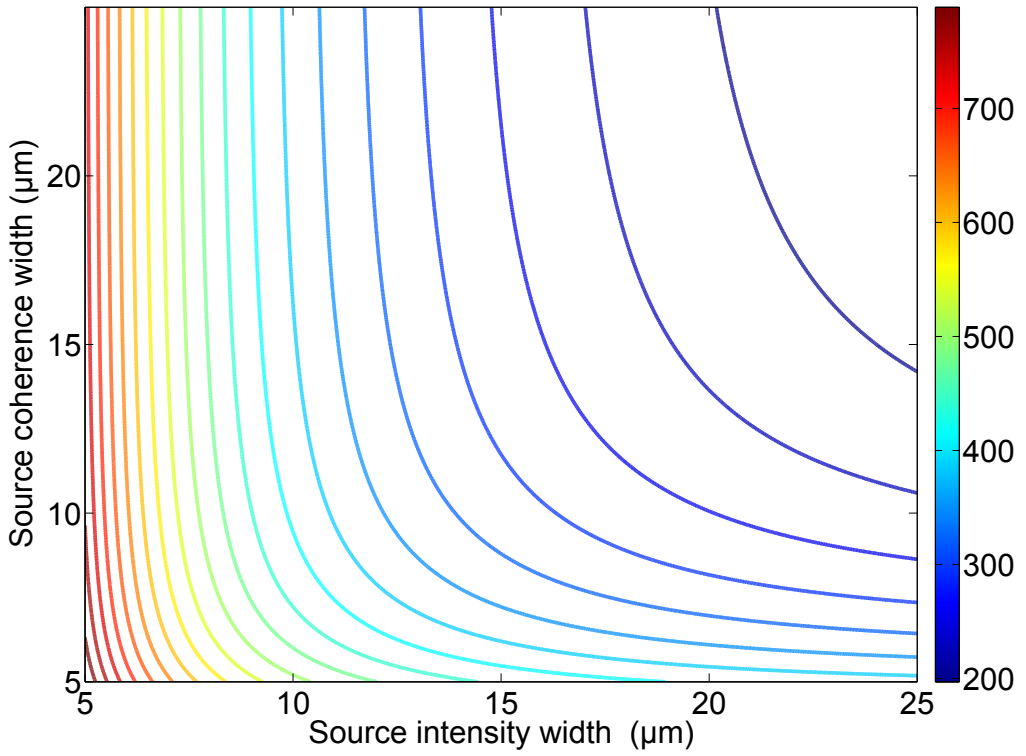

Figure 3.5: The propagated intensity width (W_{pI}) as a function of source intensity width ($w_{0\mathrm{I}}$) and source coherence width ($w_{0\mathrm{C}}$), calculated using the Gaussian-Schell model (all three quantities are shown in microns). Each contour line corresponds to a particular propagated intensity width given by its colour in the colour bar. Each point on a given contour line corresponds to a possible combination of $w_{0\mathrm{C}}$ and $w_{0\mathrm{I}}$. For instance, the same propagated beam width can be produced by large source with poor coherence (lower right of plot) or a small source with good coherence (upper left of plot). The calculation was made for $\lambda = 32$ nm wavelength radiation at a longitudinal distance of $z = 0.72$ m from the source location.

Unsurprisingly, we find that both the intensity profile and CCF maintain Gaussian profiles throughout propagation. A more striking result of the model relates to the coupling of the intensity and coherence properties after propagation. Both W_{pI} and W_{pC} depend on both the source intensity and CCF widths. This is evidenced in figure 3.5 where combinations of $w_{0\mathrm{I}}$ and $w_{0\mathrm{C}}$ that produce the same propagated W_{pI} value are shown. The results were calculated from the analytic expressions given above, for radiation of wavelength 32 nm, propagating a distance of 0.72 m away from the source.

Previously, we addressed two extreme source scenarios: the Gaussian beam (a fully coherent source, see section 3.17) and an incoherent source (section 3.37). The transition from the beamed, low-divergence radiation of the former, to the isotropic emission of the latter coincides with the change of the source CCF from perfect coherence to fully incoherent. It is clear from this line of reasoning that the source spatial coherence must influence both the propagated intensity width (equivalently the divergence) and (naturally) the propagated spatial coherence as well. The Gaussian-Schell model details explicitly the coupling between the intensity and coherence properties of the radiation, from source through to propagation. This effect is not observed with the generalised Van Cittert-Zernike theorem when the 'Fresnel-like' terms are dropped, as in equation 3.2.1, which results in the removal of this coupling.

Within the Gaussian-Schell model the ratio of the propagated intensity and coherence widths is found to be equal to the coherent fraction of the source and thus is a quantity invariant with propagation:

$$\frac{w_{\mathrm{pC}}}{w_{\mathrm{pI}}} = \frac{w_{0\mathrm{C}} D(z)}{w_{0\mathrm{I}} D(z)} = \frac{w_{0\mathrm{C}}}{w_{0\mathrm{I}}} = q_{\mathrm{IC}}. \tag{3.69}$$

Although the width of the CCF increases with propagation distance, so to does the intensity width at the same rate. Practically speaking, the 'useful' part of a beam, that which possesses a high degree of spatial coherence ($|\mu| > 0.66$ for instance), does not change with free space propagation. Effectively, the beam becomes neither more nor less coherent over any distance away from the source.

3.3 Temporal Characterization Techniques

The defining characteristic of an ultrashort pulse is its duration (temporal extent). For pulses a few nanoseconds or longer, the duration may be measured by using a photodiode and a (sufficiently) fast oscilloscope. However, in the ultrafast regime, with femtosecond duration pulses, the electronic response of a material is too slow to sample the pulse electric field accurately and a different approach is required. The most common device found in laboratories makes use of autocorrelaton. A 'gate' is required for sampling the pulse on a shorter time scale than its duration. In autocorrelation this gate is provided by a replica of the pulse. Typically, the pulse and the replica are overlapped in a nonlinear crystal, with one being delayed with respect to the other. The second harmonic signal measured as a function of the delay between pulse and replica is given by:

$$I_{SHG}(\tau) = \langle |E(t)E(t-\tau)^*|^2 \rangle \tag{3.70}$$

allowing the pulse delay (τ) to be mapped to the time domain of the pulse in a process taking advantage of the near instantaneity of the non-linear process. In order to recover the pulse duration the temporal envelope shape must be assumed

(typically Gaussian or Sech^2) in order to scale the width of the autocorrelation trace. Furthermore, (second-order) autocorrelation produces a time-symmetric trace,[1] meaning that the direction of time is not encoded into the experimental signal. Thus, pulses which are not symmetric with respect to the time axis may be measured incorrectly.

The ubiquity of the intensity autocorrelator for pulse duration measurement stems from both the simplicity of its operation (it is composed of readily available optical components) and the ease by which the experimental signal is analysed. A full temporal characterization of the field, E_t, however, requires much more than measurement of the width of the pulse envelope. A diagnostic sensitive to the temporal phase is necessary in order to truly characterize the pulse. For light in the visible and near infrared spectrum, two popular methods have emerged (as well as numerous variants) to achieve this goal: namely SPIDER (Spectral Phase Interferometry for Direct Electric-field Reconstruction) and FROG (Frequency Resolved Optical Gating).

3.3.1 SPIDER

The SPIDER technique is a specific implementation of spectral interferometry aimed at performing pulse metrology by retrieving the spectral phase of a field. Two pulse replicas are delayed with respect to the original pulse which is itself strongly chirped by a dispersive delay line. The three pulses (one chirped, two delayed) are mixed in a non-linear crystal, producing a sum-frequency signal. The large chirp means that each delayed pulse is up-converted with a quasi-cw field

[1] An autocorrelation of a higher order process, as demonstrated by Collier et al. [42], does not suffer from this limitation.

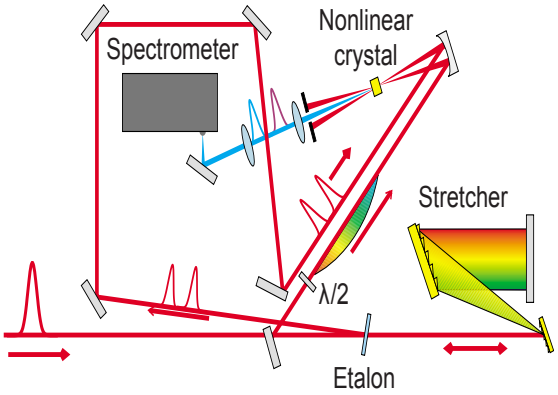

Figure 3.6: A diagram of a generic implementation of a SPIDER. $\lambda/2$ denotes a half-wave plate. Image taken from [122]

of different frequency (ω' for one, $\omega' + \Omega$ for the other). This creates two output pulses which are spectrally sheared. The two sheared pulses are then interfered on a spectrometer, producing a frequency resolved fringe pattern. The phase of the fringes, adjusted for a linear term, gives the spectral phase of the pulse up to an arbitrary offset (which is identified as the carrier envelope offset). The pulse spectrum may be retrieved, or measured independently. Full characterization in the spectral domain (spectrum and spectral phase) is sufficient for full temporal characterization, owing to the Fourier relation between the two domains.

3.3.2 FROG

At its most basic, the FROG (Frequency Resolved Optical Gating) technique may be thought of as a frequency-resolved autocorrelation. The aim of the method is to produce an experimental trace of the laser pulse in the time-frequency domain; at each pulse delay a spectrum is registered or, equivalently, at each frequency an autocorrelation is performed. This is analogous to the function of a musical

score, where time is indicated along the length of the score and tone (frequency) is encoded in the vertical position of the notes. The image of the score is enough to recover the piece of music it describes, provided, of course, the player is sufficiently skilled.

The temporal pulse envelope and phase are recovered from a measured FROG trace by application of a phase retrieval algorithm, typically of the class of *generalised projections algorithms*. Practically speaking, the algorithms retrieve a physically possible pulse (i.e. one that does not violate any laws of physics) that corresponds most closely to the measured trace.

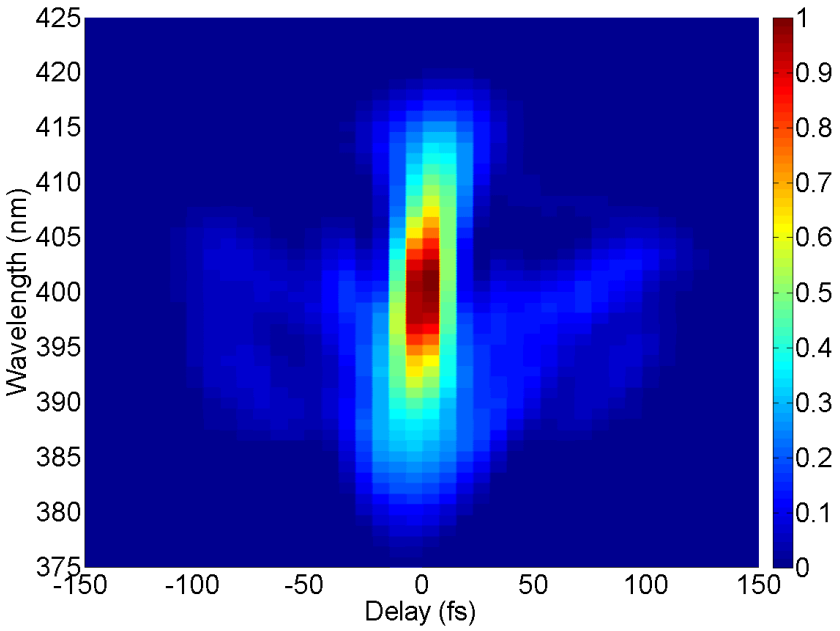

Figure 3.7: Experimental trace measured using a FROG variant known as GRENOUILLE [69]. The colour bar indicates the (normalised) intensity recorded by the CCD. A commercially available implementation of the generalised projections algorithm retrieved a pulse duration of 15.9 fs with a FROG error (rms difference in measured and retrieved traces) of 2%.

There have been many experimental implementations and variations of the FROG technique. The one most closely related to autocorrelation is the second harmonic FROG. In this variant the pulse and its replica are overlapped in a nonlinear crystal, just as in an autocorrelator, but now the second harmonic field is dispersed and imaged by a spectrometer producing the requisite time-frequency trace. Such a device, as described, suffers from a few fundamental limitations. Specifically, there is an ambiguity in the direction of time: a given pulse and its time-reversed replica produce the same trace. Additionally, if the pulse is composed of several temporal peaks, the phase between peaks is only known up to an additive factor of $n\pi$, where n is an integer. That said, FROG, and its variants, offer a simple and robust means of fully characterizing an ultrashort pulse.

3.4 Spatial Characterization Techniques

The major technical feat which must be overcome to perform temporal characterization of ultrashort pulses stems from the brevity of the object being measured: a femtosecond is a staggeringly short interval of time in the context of known natural phenomena. For spatial characterization, different difficulties emerge. With radiation in the XUV and SXR spectrum, of great scientific interest for its penetrative and spectroscopic properties, the size of the wavelength itself can be a problem, especially when diffraction from an aperture is required, since smaller wavelengths require smaller apertures. Another problem specific to short-wavelength light is the lack of robust and high optical quality optics. Lenses and waveplates, commonplace in the visible domain, are rare in the XUV or SXR.

However, the challenges are far from insurmountable and in sections 3.4.1 and 3.4.2 a number of techniques are described for the accurate measurement of the spatial properties of (short-wavelength) light.

3.4.1 Wavefront Measurement

Simply recording the intensity spatial distribution of light with a (2-D) detector, although revealing of many aspects, fails to provide any information on the spatial phase of the radiation in question. Together with the intensity information, the spatial phase allows determination of the time averaged electric field at the plane of characterization. Such knowledge, alongside the tacit assumption of full spatial coherence, allows the forward and back propagation of the field to any plane transverse to the direction of propagation by use, for instance, of the Fresnel-Kirchoff integral. This process allows the estimation of a myriad of other properties such as the minimum waist size, M^2 propagation factor, and Rayleigh range, among others. Consequently, there is an interest in techniques capable of recovering simultaneously both intensity and spatial phase information of light.

A convenient and useful means of analysing the spatial phase distribution comes from expressing it as an infinite sum of orthogonal basis functions. If the Zernike polynomials (Z_i) are employed as the basis set, we may gain some insight into any beam aberrations present in the recorded wavefront. The spatial phase can be expressed as:

$$\Phi(x,y) = \sum_{\mathrm{i}=0}^{\infty} c_{\mathrm{i}} Z_{\mathrm{i}}(x,y) \tag{3.71}$$

where c_i are weighting coefficients. In practice, the sum may be terminated at

some reasonable number (up to the eighth order has been employed in one study [45]). What is more, each of the higher order Zernike polynomials conveniently map to a well-known optical aberration. For instance, a strong weighting of polynomials Z_3 and Z_5 indicates the presence of astigmatism [56]. Thus tracking the value of c_3 and c_5, in a fit of equation 3.71 to the experimentally recovered wavefront, allows real-time minimisation of this particular aberration, as successfully shown by Flöter et al. in their optimisation of the focal quality from an ellipsoidal mirror at the FLASH FEL facility [19]. Furthermore, the 'quality' of the wavefront may be assessed by removing the spherical term, as found using the Zernike polynomials, and evaluating any residual fluctuations in the spatial phase with transverse coordinate. Authors typically quote a root mean squared (rms) deviation of the wavefront from the perfect, non-aberrated case, in terms of a fraction of the wavelength, with an rms deviation of $\frac{\lambda}{n}$ equal to a phase deviation of $\frac{2\pi}{n}$. Marcheval's criterion [4] states that if the rms deviation of the wavefront is smaller than $\frac{\lambda}{14}$, the beam may be regarded as diffraction limited. Naturally, a means of measuring the wavefront with an accuracy better than $\frac{\lambda}{14}$ is required in order to make this determination.

3.4.1.1 Shack-Hartmann Sensor

A popular device for measuring the wavefront and intensity distribution of light is the Shack-Hartmann sensor. Perhaps best known for its use in ophthalmic surgery in measuring aberrations of the eye, a similar device in fact has its origins in attempts to compensate for atmospheric distortions in astronomy [113]. For visible light, the Shack-Hartmann sensor is formed from a grid-like arrangement of micro-lenses, with a detector placed behind at a distance equal to the lens

focal length. Illumination of the lenslet array produces a series of beamlets that in turn form a grid-like pattern of spots on the detector.

The relative intensity of the spots provides information on the intensity illuminating each individual micro-lens. Thus, a discretised picture of the 2-D transverse intensity distribution may be reconstructed from the measurement. The location of a particular spot is related to the local gradient in spatial phase at its parent micro-lens location. Specifically the local gradient in the spatial phase $\left(\frac{\delta\phi}{\delta x}_i\right)$ at lenslet i, located at position x_i, is given by:

$$\frac{\delta\phi}{\delta x}_i = \frac{2\pi\Delta X_i}{\lambda f} \tag{3.72}$$

where λ is the wavelength of the incident light, f is the focal length of the lenslet and ΔX_i is the displacement of the focal spot measured on the detector. A reference wave, providing a known wavefront, is needed in order for the spot displacement to be calibrated. Typically, illumination of a small pinhole (placed prior to the lenslet array), providing a spherical wavefront is used. Once calibrated, the transverse spot displacement, as measured on the detector without the pinhole present, is used with equation 3.72, allowing the wavefront to be recovered through integration of the spatial phase gradient, along with interpolation over the discretised map of points. A complimentary measurement of the far-field beam irradiance coupled with a Shack-Hartmann sensor has been shown to provide a more accurate characterization of beam parameters, even including information on the spatial coherence [115].

For light in the XUV/SXR spectrum, there are no materials which can be formed into effective lenses for use in a traditional Shack-Hartmann sensor. How-

ever, various groups [19, 45, 95] have shown that a grid of pinholes punctuating an opaque substrate just as well follow the measurement principle described above (referred to as Hartmann sensors, to distinguish them from lenslet arrays). Without any focussing elements, the requirement of placing the detector one focal distance from the array is relaxed. The wavefront is recovered with greater accuracy for a large array-detector distance, since the smallest possible spatial phase gradient, corresponding to the smallest lateral spot displacement, may be measured when the array-detector distance is maximised. However the array-detector distance must be small enough so that each spot is composed (for the most part) of light from a single lenslet. Clearly, a compromise is necessary in setting the array-detector distance to satisfy accurate retrieval of both the wavefront and intensity distribution.

The Shack-Hartmann sensor benefits from the ability to be used as a single-shot diagnostic: the spatial properties may be recorded from a single CCD exposure, requiring no scanning of parts or parameters. This is a marked advantage for characterizing light sources which show appreciable shot-to-shot variation (for instance free electron lasers based on the SASE principle [89]). A potential disadvantage of Shack-Hartmann type devices comes from considering the spectrum of the incident light. The discussion up to now has presumed monochromatic illumination. However if the light has a broadband and/or a complex structured spectrum (i.e. supercontinuum generation or HHG) then the beam properties recovered represent a spectral average. Furthermore, at best, depending on the complexity of the incident spectrum, one might observe a blurring or spreading of the detected array of spots, impacting on the accuracy with which the wavefront and intensity distribution is retrieved. At worst, little accurate information of

the beam may be recorded if the cross-talk (spatial-overlap) of adjacent spots on the detector is sufficiently severe. That said, it is possible to perform a spectrally resolved measurement of the intensity distribution alone, as shown by Praeger et al., if an iterative algorithm is used, aided by some prior knowledge of the incident spectrum [62].

In the XUV/SXR spectral region, Hartmann sensors have been used to measure the spatial properties of HHG [95] as well as radiation from the free electron laser FLASH [19]. Gautier et al. [95] used a device constructed from a 100 μm thick nickel plate, into which, 80 μm wide holes were drilled, each separated from its neighbouring hole by 380 μm. A grid of 51 by 51 holes was employed, with the detector (CCD) placed 20 cm downstream of the array apertures. The authors used metallic filters to focus their study on the wavefront quality of a beam composed of high harmonic orders 23-29 of the 800 nm driving beam, generated in a long (8 mm thick) argon-backed gas cell. After fitting Zernike polynomials to the recovered wavefront, the authors reported a residual rms phase error of $\frac{\lambda}{6.67}$, with a measurement accuracy estimated to be $\sim \frac{\lambda}{50}$: the aberration was larger than Marcheval's criterion for a diffraction limited beam by approximately a factor of two. The dominant aberration was identified as astigmatism and the authors noted that this was also present in the driving beam, but to a much larger degree. This correlation of the presence of aberrations, in both driving laser and harmonic beam, was also observed in a similar study [27], where the driving laser astigmatism was controlled by a deformable mirror. These studies beg the question of what quantitative relationship, if any, links aberrations of the fundamental with those of the generated high harmonics? This is a question of importance for the production of high quality XUV beams for seeding free elec-

tron lasers, for instance [22]. In a later study conducted by Lohbreier et al. [45], again using a Hartmann sensor to measure the wavefront of HHG, the authors deliberately introduced aberrations onto the driving laser using a spatial light modulator. They found no clear correlation between aberrations on the fundamental and those measured on the HHG wavefront, contrary to previous work. They suggested that difference in gas target design between their study and those beforehand may have given rise to their different conclusions. The authors also conceded that different conclusions from different studies imply that the relationship between driver and HHG spatial properties is complex and, as yet, not well understood.

3.4.1.2 SWORD

The power of the Hartmann sensor for performing accurate, single-shot measurements of beam wavefront and intensity is well evidenced in the previous section. Indeed, its application to the characterization of HHG allowed not only optimisation of the harmonic wavefront, but also raised questions about the generation process, through probing the inheritance of aberrations from driving laser to harmonic field. Yet little information can be garnered on the spectral dependence of the spatial properties of HHG. The presence of such coupling between the spectral and spatial domains would have a deleterious effect on both the quality of the harmonic focus as well introducing a longitudinal position dependent pulse duration [34]. To address this issue, a new characterization technique was devised and demonstrated by Frumker and colleagues, that they named SWORD (Spectral Wavefront Optical Reconstruction by Diffraction), capable of performing a spectrally resolved measurement of the intensity and wavefront of light [33]. The

method is simple in its execution: one need only to scan a small aperture (a thin slit in their demonstration) transversely across the beam, with the resultant diffraction pattern produced at each aperture position recorded on a CCD. In a

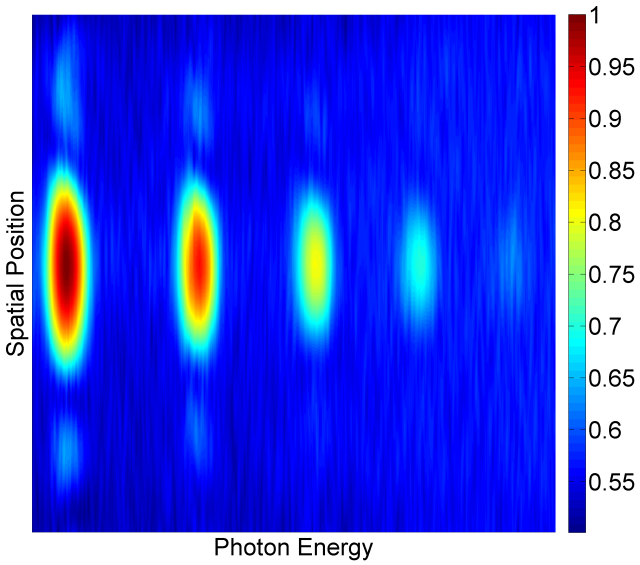

Figure 3.8: Single CCD exposure, taken during the course of a SWORD scan. The horizontal direction encodes spectral information, the vertical shows diffraction from the thin slit evidenced by the typical sinc^2 pattern. Harmonic orders 23-31 (from left to right) of the 800 nm wavelength driving laser are displayed. The (normalised) intensity is given by the colour bar on the right of the figure.

manner with obvious parallels to the Shack-Hartmann sensor, the intensity and spatial phase gradient at a particular slit location are found through the intensity and position of the recorded diffraction pattern. The position of the diffraction pattern (the centroid), when adjusted for the location of the slit, must be integrated (summed) to recover the wavefront. Specifically, the spatial phase is found

using:

$$\Phi(x)_n = \frac{2\pi}{\lambda} \sum_{i=0}^{n} \delta x \frac{X_i - x_i}{d} \tag{3.73}$$

where δx is the distance between two adjacent slit positions in a scan (the step size), X_i is the measured diffraction pattern position, x_i is the slit position and d is the slit-detector distance. The intensity of the light at position i is simply found from the integrated signal measured by the CCD for the slit located at x_i.

The spectral dependence of the spatial properties may be simultaneously measured by placing a diffraction grating (or a similar optic) after the slit, such that the beam is spectrally dispersed orthogonal to the slit scanning direction, as observed on the CCD. The only requirement of the incident light is that it shows spatial coherence over the length scale of the slit width. The slit width itself is chosen so that it is small enough to cause measurable diffraction by light with a wavelength the same as the radiation source. Also, the smaller the slit width, the smaller the area over which the wavefront is sampled for a particular slit location. However, the slit must be wide enough that sufficient signal is measured by the CCD over the complete transverse span of the scan.

A SWORD scan produces, for each spectral component, a series of diffraction patterns. An example single CCD exposure is shown in figure 3.8. The spectral (dispersed in the horizontal direction) and spatial (single slit diffraction in the vertical direction) properties are clearly encoded.

The intensity and spatial phase for q=23 (driven by an 800 nm wavelength fundamental beam) recovered using SWORD, are shown in figure 3.9. The intensity and phase show no significant scatter about the lines of best fit, and agree

with the functional forms of HHG spatial properties reported in both [33] and [34].

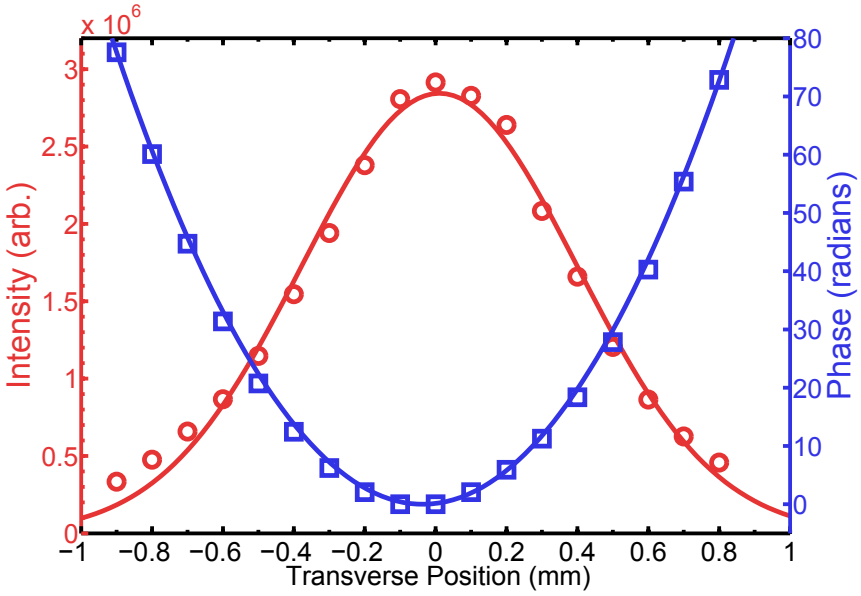

Figure 3.9: An example of the recovered spatial properties for a single harmonic order (q=23 from a driving wavelength of 800 nm) using the SWORD technique. Intensity is shown with red circles, spatial phase with blue squares. The red line shows a Gaussian function (with FWHM of 0.92 mm) fitted to the intensity data. The blue line shows a parabola fitted to the phase data, as per a divergent wavefront. The errorbars are the same size or smaller than the symbol size for all data points.

The ability to measure the spectral dependence of spatial properties is of specific importance for broad-bandwidth sources such as HHG. Minimisation of any coupling between the spectral and spatial properties offers the potential of maximising the peak intensity produced by a focussed harmonic beam, through localising energy in both space and time. This point was eloquently demonstrated in the calculations of Frumker et al., where they showed that the order dependence of harmonic wavefront curvature would lead to a dramatic temporal evolution of

the resultant attosecond pulse train about the harmonic focal plane [34].

The SWORD technique is not without certain weaknesses. One potential drawback, shared with the Hartmann sensor, relates to the fact that the wavefront measurement involves integration of the spatial phase gradient. The gradient itself is averaged over the slit width and no direct measure of the phase is performed. Thus, both techniques are one step removed from the quantity of interest compared to a method which measures the spatial phase directly. A second downside comes from the need for the slit to be scanned across the beam. Single-shot measurement is not possible, so the properties of the source are required to not change significantly over the duration of the scan. Finally, the SWORD technique makes no account for the spatial coherence of the illuminating radiation. Measurement of this important property would need to be performed separately to allow for a more complete characterization.[1] That said, the simplicity and accuracy of the technique, as well as the ability to measure spectrally dependent spatial properties, stand strongly in favour of its utility for metrology, especially for light in the XUV/SXR spectrum.

3.4.1.3 Other Wavefront Characterization Techniques

A variety of alternate methods have been described capable of measuring the wavefront and intensity profile of light in the XUV/SXR spectrum. Lateral shearing interferometry was used by Austin et al. to measure the wavefront and intensity profile in the near-field (at the source location), by interfering high order harmonics from two spatially separated laser foci [28]. Lee et al. used a

[1] A more detailed discussion of another potential weaknesses of SWORD is found in the appendix.

holographic technique interfering a harmonic beam with one diffracted from a pinhole, so called point diffraction interferometry, allowing measurement of the far-field spatial phase [29]. Both techniques suffer from complexity in both the experimental deployment and post-processing of data, not found (to such a degree) in either Hartmann or SWORD techniques.

For x-ray free electron lasers (XFELs), producing high brilliance radiation with photon energies in excess of 1 keV, the challenge of performing accurate characterization is even greater. Despite the potential for the focussed XFEL beam to damage materials, a number of techniques have been successfully demonstrated. In the hard x-ray region, Schropp et al. used a ptychographic technique: measuring the diffraction patterns formed from a focussed beam impinging on nanometer-scale structured objects [17]. They demonstrated that it is possible to recover the full caustic (intensity and phase information) of the beam, including any aberrations. Although the best results were obtained after averaging over a few hundred FEL pulses, the technique could be used single-shot. Rutishauser et al. were also able to characterize hard x-ray pulses from an FEL by using what they described as a 'grating interferometer': a pair of transmission gratings were used, placed one after the other, with the second rotated with respect to the first [83]. The combination created a Moiré pattern which was recorded and used to retrieve the wavefront and source location, again in a single-shot manner.

3.4.2 Characterizing the Degree of Spatial Coherence

The description of coherence given in section 3.2 demonstrates that the degree of spatial coherence of a source is an important property governing the propa-

gation of radiation. Furthermore, experimental methods which depend on good correlation of light across the beam, such as holography and coherent diffractive imaging, rely on the spatial coherence being high (and well characterized). As such, techniques for measuring the degree of spatial coherence are desired.

3.4.2.1 Thompson-Wolf method

The most direct means of characterizing the spatial coherence of light comes from sampling the CCF at a range of test point separations. This can be achieved by measuring the interference pattern produced by a pair of slits. As identified in equation 3.28, the fringe modulation depth (visibility) can be related to the magnitude of the CCF evaluated for a point separation equal to the slit spacing (s). Although authors sometimes regard measurement using one slit pair, placed centrally with respect to the beam centre, as sufficient to determine the degree of spatial coherence [73], true characterization requires the CCF to be measured at *all possible* pinhole separations (and orientations) across the 2-D transverse extent of the beam. If, however, it can be assumed that the CCF is axially symmetric, then only point separations in one transverse dimension across the beam need be measured. The situation is simplified even further if shift invariance of the CCF is assumed. Then, the series of interference patterns, produced by slit pairs with a differing separation, each placed in the centre of beam, is enough to characterize the spatial coherence. Such a procedure is known as the 'Thompson-Wolf' method [118], after the authors of the study first demonstrating its application to partially coherent light.

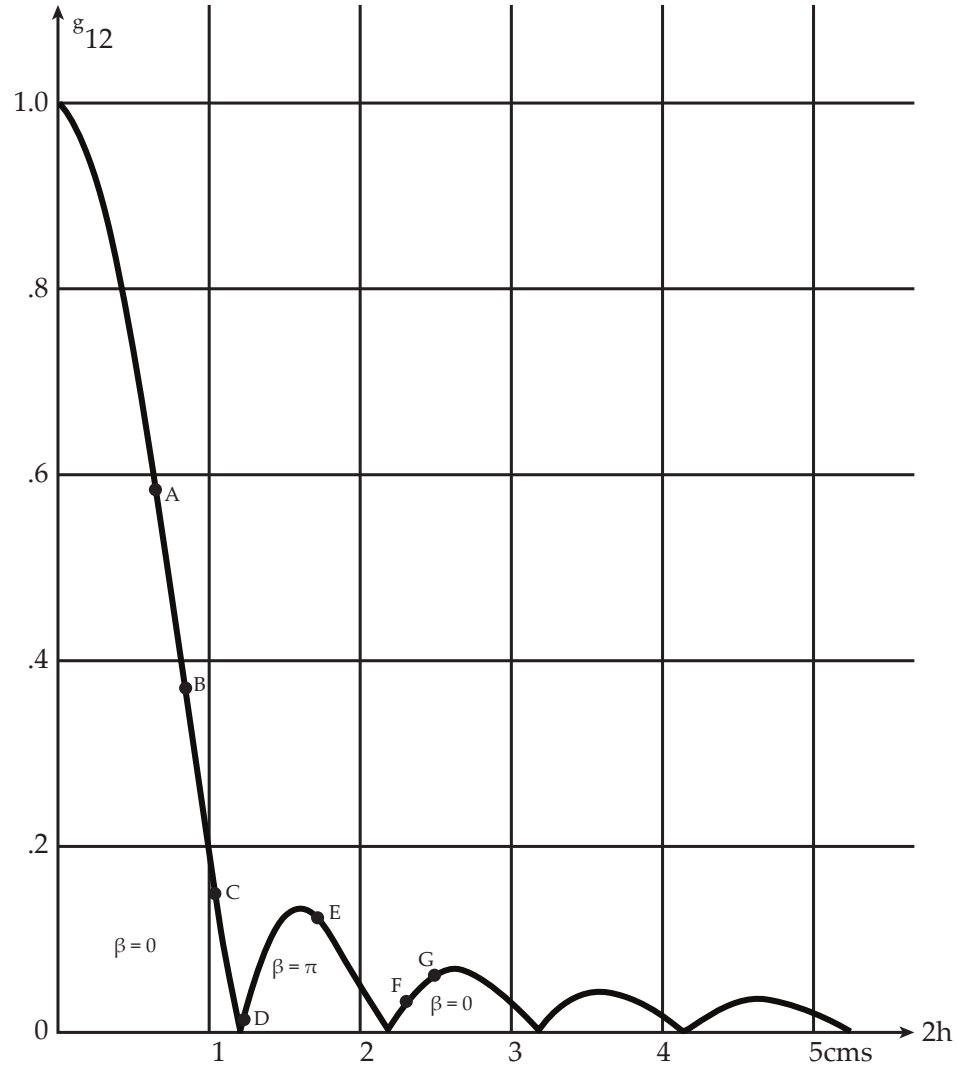

Figure 3.10: Figure (edited to improve clarity) originally published in [118], showing the first application of the Thompson-Wolf method for spatial coherence characterization. The points labelled A - G are measured values of the magnitude of the CCF (g_{12} in their notation) for a spectrally and spatially-filtered mercury vapour lamp. A fit derived from the Van Cittert-Zernike theorem for an incoherent disc source is shown by the thick black line.

3.4.2.2 Other Spatial Coherence Characterization Techniques

An alternate, non-interferometric approach to characterize the CCF was described by Tran and co-authors [26]. They recorded the intensity distribution of x-rays from an undulator source at multiple longitudinal locations. The source was treated as quasi-homogeneous, allowing the recorded beam propagation to be modelled on the basis of the mutual intensity function and hence the CCF was recovered. A similar experimental procedure was used by Mey et al. to characterize the FEL FLASH through measurement of the four dimensional Wigner function [87]. In both studies the authors we able to retrieve the CCF of the assumed monochromatic radiation field, however the requirement of shifting the detector (in the case of [26] by over nearly a meter in distance) is experimentally inconvenient.

For high harmonic generation, measuring the interference from a Fresnel mirror has been shown to provide spatial coherence information [54]. The 13^{th} and 15^{th} harmonic orders generated in xenon were collimated and steered onto a two-part mirror. The two parts of the mirror were angled to produce interference detected in the far-field. Such a method allows the CCF to be measured at a fixed point separation, at all transverse positions across the beam simultaneously. In other words, the shift invariance of the CCF could be determined single shot. Characterizing different point separations requires changing the Fresnel mirror-detector distance, thus the technique suffers a similar drawback to the work of Tran et al. described above.

3.5 Spatial Coherence of HHG (Theory)

The spatial coherence of high harmonic generation has been a topic of interest to researchers for some time. The production of near fully coherent XUV light, as demonstrated by Bartels et al. [72], proved that HHG has marked benefits over alternate, plasma-based radiation sources, while at the same time opening the door for a number of potential applications. Other studies have shown that the spatial coherence of HHG can be degraded by either increasing the level of ionization in the medium [86] or, in the case of a CEP-stable mid-IR driving laser, through a time-dependent spectral shift in the harmonic field [37].

The work presented in this thesis, among other studies, would benefit from the development of an analytic model of the spatial coherence of the harmonic radiation source. Here we attempt to construct such a model. Although not including all of the potential complexities associated with HHG, the analytic form allows the order dependence of the harmonic spatial coherence to be estimated explicitly. The derivation developed below closely resembles that presented by Ditmire et al. in [86], up to a small difference in notation. The authors of that study focussed on the process of partial coherence being passed from the fundamental beam to the harmonic field. Here we extend their work by attempting to account for effects related to the intensity-dependent dipole phase of the harmonic emission as well.

We begin with the generic case of a field $E(X,t)$ described by:

$$E(X_i,t) = E_i = A_0\epsilon_x(X_i)\epsilon_t(t)\exp\Big[i\phi(X_i,t)\Big] \tag{3.74}$$

where ϵ_x and ϵ_t are real, envelope functions for the spatial and temporal parts of

the field, respectively. We have explicitly assumed that the spatial and temporal parts are separable: the pulse does not possess any space-time coupling. The CCF evaluated at the locations X_1 and X_2 is given by equation 3.20. It can be expressed as:

$$\mu_{12} = \frac{\langle E_1 E_2^* \rangle}{\sqrt{\langle |E_1|^2 \rangle \langle |E_2|^2 \rangle}} \tag{3.75}$$

where, as before, the angled brackets indicate a time average. Using equation 3.74 we find:

$$\begin{aligned} \mu_{12} &= \frac{A_0^2 \epsilon_x(X_1)\epsilon_x(X_2)\langle \epsilon_t^2 \exp[i(\phi_1 - \phi_2)]\rangle}{A_0^2 \epsilon_x(X_1)\epsilon_x(X_2)\langle \epsilon_t^2 \rangle} \\ &= \frac{\langle \epsilon_t^2 \exp[i(\phi_1 - \phi_2)]\rangle}{\langle \epsilon_t^2 \rangle} \\ &= \frac{\langle \epsilon_t^2 \rangle \langle \exp[i(\phi_1 - \phi_2)]\rangle}{\langle \epsilon_t^2 \rangle} \\ &= \langle \exp[i(\phi_1 - \phi_2)]\rangle = \langle \exp[-i\Delta\phi]\rangle \end{aligned} \tag{3.76}$$

where ϕ_i is the phase evaluated at location X_i, $\Delta\phi = \phi_2 - \phi_1$, and in the third line we have assumed that changes in the temporal envelope of the field are not correlated with changes in the phase.

Assuming $\Delta\phi$ is small, only terms up to the square of $\Delta\phi$ in the Taylor series are retained:

$$\exp(-i\Delta\phi) \approx 1 - i\Delta\phi - \frac{\Delta\phi^2}{2!} \tag{3.77}$$

hence:

$$\mu_{12} = 1 - i\langle\Delta\phi\rangle - \frac{1}{2}\langle\Delta\phi^2\rangle \tag{3.78}$$

and for the CCF magnitude:

$$|\mu_{12}| \approx \sqrt{1 - \langle\Delta\phi^2\rangle + \langle\Delta\phi\rangle^2 + \frac{\langle\Delta\phi^2\rangle^2}{4}}. \tag{3.79}$$

We will neglect the higher order term $\frac{\langle\Delta\phi^2\rangle^2}{4}$ and use the binomial expansion to write:

$$\begin{aligned} |\mu_{12}| &\approx 1 - \frac{1}{2}\Big(\langle\Delta\phi^2\rangle - \langle\Delta\phi\rangle^2\Big) \\ &= 1 - \frac{V(\Delta\phi)}{2} \end{aligned} \tag{3.80}$$

where $V(\Delta\phi)$ denotes the variance of $\Delta\phi$. Equation 3.80 agrees with our expectations for the CCF: in the case where the phase variations are correlated, $\Delta\phi$ is a constant, hence $V(\Delta\phi) = 0$ and $|\mu| = 1$, i.e. the wave is spatially coherent.

In section 2.4 the following expression was used for the phase of the harmonic field:

$$\phi_q = q\phi_0 + \phi_\mathrm{d} \tag{3.81}$$

where ϕ_0 is the phase of the fundamental and ϕ_d is the dipole or intrinsic intensity-dependent phase, first introduced in section 2.4. Hence $\Delta\phi_q = q\Delta\phi_0 + \Delta\phi_\mathrm{d}$ and

by using the basic properties of the variance operation we find:

$$\begin{aligned} V(\Delta\phi) &= V(q\Delta\phi_0 + \Delta\phi_\mathrm{d}) \\ &= V(q\Delta\phi_0) + V(\Delta\phi_\mathrm{d}) + 2C(q\Delta\phi_0, \Delta\phi_\mathrm{d}) \\ &= q^2 V(\Delta\phi_0) + V(\Delta\phi_\mathrm{d}) + 2qC(\Delta\phi_0, \Delta\phi_\mathrm{d}) \end{aligned} \tag{3.82}$$

where $C(A, B)$ denotes the covariance of the functions A and B. Assuming that the phase differences in the fundamental field are not correlated with those of the dipole phase yields:

$$|\mu_q| = 1 - \frac{1}{2}\Big[q^2 V(\Delta\phi_0) + V(\Delta\phi_\mathrm{d})\Big]. \tag{3.83}$$

Equation 3.83 contains the two possible contributions that may degrade the coherence of the harmonic source: partial coherence is transferred from the fundamental beam to harmonic field *and* a phase decorrelation arises from the difference in the dipole phase experienced across the beam's extent.

The CCF of the partially coherent fundamental beam (μ_0), in the limit of a small deviation from full coherence, obeys equation 3.80:

$$|\mu_0| = 1 - \frac{V(\Delta\phi_0)}{2} \tag{3.84}$$

where the '0' subscript indicates a property of the fundamental beam. Hence:

$$V(\Delta\phi) = 2(1 - |\mu_0|). \tag{3.85}$$

The dipole phase difference can be written as:

$$\begin{aligned}\Delta\phi_d &= -\alpha\Big[I_0(X_2) - I_0(X_1)\Big] \\ &= \alpha\Big[I_0(X_1) - I_0(X_2)\Big]\end{aligned} \tag{3.86}$$

where α is a constant which depends on the trajectory of the harmonic emission and I_0 is the intensity of the fundamental: $I_0(X_i) = A_0^2\epsilon_x(X_i)^2\epsilon_t^2$. The variance of the dipole phase difference is then:

$$\begin{aligned}V(\Delta\phi_{\mathrm{d}}) &= \langle\Delta\phi_{\mathrm{d}}^2\rangle - \langle\Delta\phi_{\mathrm{d}}\rangle^2 \\ &= \alpha^2\Delta I_{\mathrm{X}}^2\Big[\langle\epsilon_t^4\rangle - \langle\epsilon_t^2\rangle^2\Big] \\ &= \alpha^2\Delta I_{\mathrm{X}}^2 V(\epsilon_t^2)\end{aligned} \tag{3.87}$$

where $\Delta I_{\mathrm{X}} = A_0^2\Big[\epsilon_x(X_1)^2 - \epsilon_x(X_2)^2\Big]$ can be thought of as the difference in the fundamental intensity sampled at locations X_1 and X_2, normalised to the temporal peak of the laser pulse. It should be noted that we have implicitly assumed that the harmonic pulse, like the fundamental beam, does not possess any space-time coupling. However, owing to the non-perturbative nature of the high harmonic process, with both the intensity and phase of the emission depending on the fundamental intensity, the temporal duration of the harmonic pulse is almost certainly dependent on the transverse position [53]. It is expected that this space-time coupling will lead to a further degradation in the harmonic spatial coherence, not accounted for here.

Bringing together equations 3.85 and 3.87 we arrive at expression for the CCF

of the harmonic radiation source:

$$|\mu_q| = 1 - q^2(1 - |\mu_0|) - \frac{1}{2}\alpha^2 \Delta I_{\mathrm{X}}^2 V(\epsilon_t^2). \tag{3.88}$$

In the case of coincidental points ($X_2 = X_1$), $|\mu_0| = 1$ and $\epsilon_x(X_1)^2 = \epsilon_x(X_2)^2$, hence $\Delta I_{\mathrm{X}} = 0$ and $|\mu_q| = 1$, as expected.

Equation 3.88 has a number of interesting features. The harmonic coherence is observed to depend on the quantum trajectory through α, with longer trajectories possessing poorer coherence. Also, the contribution from the dipole phase means the harmonic CCF is not shift invariant since ΔI_q does not (generally) depend on the point separation $X_2 - X_1$ only. To illustrate, consider a fundamental beam with an intensity profile that possesses radial symmetry. When the harmonic CCF is sampled at two locations satisfying $X_2 = -X_1$, i.e. symmetric with respect to the beam centre, the contribution to the harmonic CCF from the dipole phase vanishes, since $\Delta I_X = 0$. For non-symmetric positions the contribution is non-zero. The importance of this point is emphasised in section 4.4.3.

In order to produce a coherent harmonic field, equation 3.88 presents two conditions that must be satisfied:

1. The fundamental field must be coherent ($|\mu_0| = 1$).

2. There must be little variation of the fundamental beam intensity across the transverse region where the harmonics are emitted.

Therefore, one might expect a highly coherent harmonic beam to be produced by a coherent laser producing a uniform 'flat-top' focal spot in a medium with minimal ionization.

Chapter 4

Scanning Interference Measurement for Integrated Transverse Analysis of Radiation (SCIMITAR)

In the previous chapter different methods were described for measuring the spatial properties of light. The SWORD technique [33], devised and demonstrated by Frumker and colleagues, was highlighted due to the potential of performing a spectrally resolved characterization of beam spatial properties. This ability is important for radiation sources such as high harmonic generation, where evidence suggests that, generally, the radiation spatial properties will be dependent on harmonic order (wavelength) [33, 71, 85]. However, the SWORD technique is only able to measure the beam intensity and spatial phase, while the spatial coherence of the light source remains unknown.

To address this specific shortcoming of SWORD a new method for performing spatial metrology has been devised, that we have named Scanning Interference Measurement for Integrated Transverse Analysis of Radiation (a.k.a. SCIMITAR) [108]. As will be shown, the SCIMITAR technique is able to retrieve the

same information as a SWORD scan, whilst simultaneously performing a detailed characterization of the spatial coherence of the radiation.

4.1 Measurement Principle

In a similar vein to SWORD, SCIMITAR is a scanning technique which makes use of a diffracting aperture to perform beam characterization. It is a specific implementation of a variable-separation two-pinhole interferometer. The pinholes are formed by the use of two apertures: one shaped like a tilted 'X' (hereafter referred to as the 'X-slit', see figure 4.1) and another shaped like a thin horizontal slit.

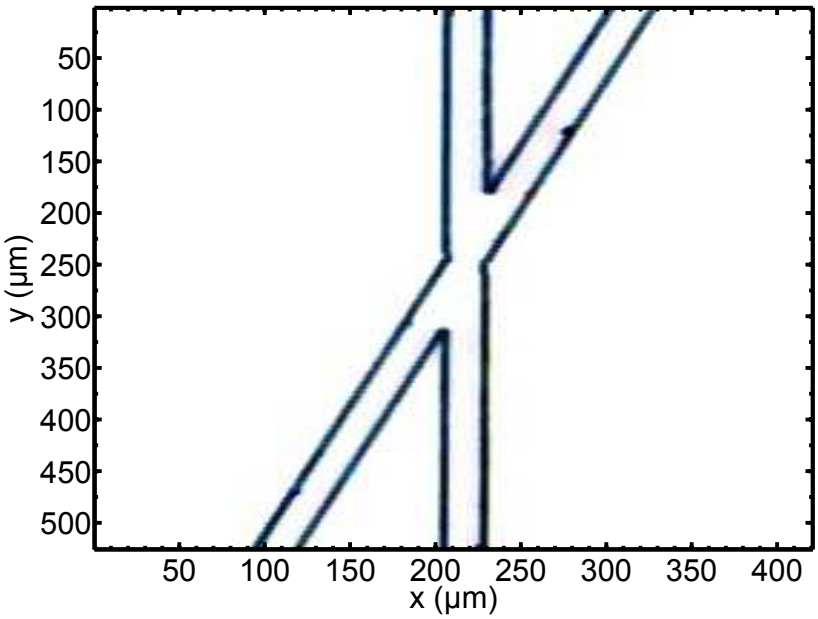

Figure 4.1: Microscope image of the central portion of the X-slit used in experiments described in this thesis. The colour of the raw image has been inverted and adjusted to emphasise the shape of the aperture edge. The X-slit horizontal width is 20 microns everywhere but at the centre, where it is observed to be wider.

When placed one after the other their combination forms a pinhole pair.[1] Translation of the X-slit in the vertical direction changes the (horizontal) separation of the pinholes. In our case the X-slit is tilted (formed of one vertical 'bar' and one angled 'bar'), meaning that one pinhole of the pair remains stationary (at the beam centre) during the course of a scan (hereafter the referred to as the 'static' pinhole), while the other pinhole (hereafter the 'moving' pinhole) is effectively moved by vertical translation of the X-slit.

A SCIMITAR scan involves recording the interference patterns produced over a range of pinhole separations. In section 4.2, it is shown that the beam properties are encoded in the measured fringe patterns and may be retrieved through Fourier domain analysis.

4.1.1 Aperture Design

There are a few aspects to note regarding the design of the apertures used for SCIMITAR. A tilted X-slit is used since, when combined with the horizontal slit, it produces a pinhole pair where the location of one pinhole remains stationary throughout the course of scan. This is important as it is assumed that the contribution to the interference patterns from light from the stationary pinhole does not change over the duration of the measurement. Changes to the interference pattern with pinhole separation are considered to be only due to the 'moving' pinhole and hence only the beam properties at the moving pinhole location are encoded.

The horizontal widths of the bars forming the X-slit define the horizontal

[1] The longitudinal separation (z') of the two apertures must be less the Rayleigh range of the formed pinholes: $z' < \frac{\pi a^2}{\lambda}$, where a is the pinhole diameter and λ the wavelength of illumination.

extent of the formed pinholes whereas the horizontal slit height defines the pinhole vertical extent. The smaller the formed pinhole, the smaller the area of the beam the pinhole samples, influencing the precision of the measurement. Furthermore, the pinhole width (a) also affects the footprint of the experiment, since it is one parameter (along with the radiation wavelength) that defines the minimum distance the detector must be placed to record interference fringes. However, smaller pinholes mean a lower photon flux reaches the detector, requiring a longer exposure time per acquisition, prolonging the length of the measurement and increasing the sensitivity of the results to (temporal) fluctuations in the source properties.

It should also be noted that the combination of X-slit and horizontal slit produces one square pinhole ('static') and one shaped like a parallelogram ('moving'). In principle this could influence (and complicate) the produced interference pattern. However, choosing a small interior angle of the X-slit (the angle between the vertical and angled bars is 9.9° in our case) allows the deviation of the shape of the moving pinhole from the ideal square form to be minimised.

Failure to correctly orientate the X-slit,[1] results in not only an inaccurate measurement of the slit separation (after reading off the X-slit vertical position) but also means the 'static' pinhole can no longer be assumed to remain fixed throughout the scan. Hence, care must be taken to ensure that the 'vertical' bar of the X-slit is parallel to the direction in which it is translated.

[1] Orientation here refers to rotation of the X-slit in the plane the aperture lie in.

4.2 Analysing Fringe Patterns

Analysing the interference patterns produced by a SCIMITAR scan is aided by deriving the analytic form of the fringe pattern itself. We begin by considering two pinholes drilled into an otherwise opaque screen lying on a plane labelled by σ_1. The pinholes have a width a and are centred on $x = 0$ (labelled pinhole 1) and $x = s$ (labelled pinhole 2), respectively. The field reaching a point X on a plane σ_2 (the detector plane), some longitudinal distance z from σ_1 is given by:

$$E(X) = \int_{-\frac{a}{2}}^{\frac{a}{2}} A_1 \exp(ik_0 r_1 + i\phi_1) dx + \int_{s-\frac{a}{2}}^{s+\frac{a}{2}} A_2 \exp(ik_0 r_2 + i\phi_2) dx \tag{4.1}$$

where A_i and ϕ_i are the field amplitude and phase sampled by pinhole i, r_i is the distance between pinhole i and a point X on σ_2 ($i \in \{1, 2\}$) and k_0 is the wavenumber of the illuminating radiation.[1] A diagram of a two-pinhole interferometer arranged this way is shown in figure 4.2

Under the familiar Fraunhofer approximation r_1 and r_2 can be written as:

$$\begin{aligned} r_1 &\approx z + \frac{X^2}{2z} \\ r_2 &\approx z + \frac{X^2}{2z} + \frac{Xx}{z} \end{aligned} \tag{4.2}$$

substituting into 4.1 gives:

$$E(X) = \exp\left(ik_0 z + \frac{iX^2}{2z}\right)\left[\int_{-\frac{a}{2}}^{\frac{a}{2}} A_1 \exp(i\phi_1)\mathrm{d}x + \int_{s-\frac{a}{2}}^{s+\frac{a}{2}} A_2 \exp\left(i\frac{k_0 Xx}{z} + i\phi_2\right)\mathrm{d}x\right] \tag{4.3}$$

A detector lying on σ_2 is sensitive to the intensity $I(X) = \langle E(X)E(X)^* \rangle$. After

[1] The intensity and phase at each pinhole are assumed to not vary across the extent of the pinhole itself.

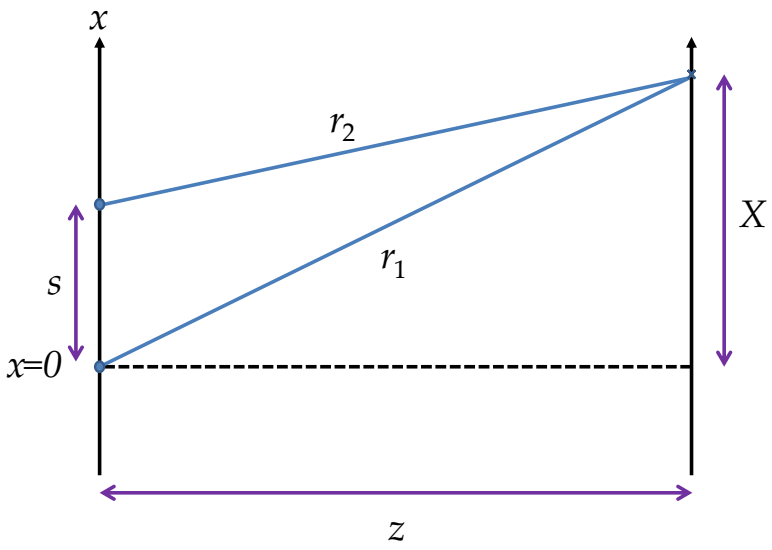

Figure 4.2: Diagram of the experimental geometry for two-pinhole interference.

evaluating the integral in 4.3 the measured (intensity) pattern takes the form:

$$I(X) = a^2(I_1 + I_2)\mathrm{Sinc}\left[\frac{k_0 a}{2z}\left(X - \frac{s}{2}\right)\right]^2 \left\{1 + \frac{2\sqrt{I_1 I_2}}{I_1 + I_2}|\gamma|\mathrm{Cos}\left[\frac{k_0 s}{z}\left(X - \frac{s}{2}\right) + \Delta\phi\right]\right\}$$

$$= \epsilon(X)\left\{1 + \mathcal{V}\mathrm{Cos}\left[\frac{k_0 s}{z}\left(X - \frac{s}{2}\right) + \Delta\phi\right]\right\} \quad (4.4)$$

$$= \epsilon(X)\left\{1 + \mathcal{V}\mathrm{Cos}\left[\frac{k_0 s}{z}X - \frac{k_0 s^2}{2z} + \Delta\phi\right]\right\} \quad (4.5)$$

where I_i is the intensity sampled by pinhole i, $\Delta\phi = \phi_2 - \phi_1$, γ is the complex coherence factor (CCF) as defined in chapter 3, $\mathcal{V}$ is the fringe visibility and $\epsilon(X)$ may be thought of as the envelope of the fringe pattern created by diffraction from the pinholes.

Measuring the spatial phase of a radiation field using a two pinhole interferometer is by no means a new idea. Indeed Born and Wolf outlined the concept

in their textbook 'Principles of Optics' in 1980 [4]. To retrieve the wavefront the fringe phase must be extracted. This can easily be achieved in the Fourier domain, as first described by Takeda et al. [117]. Variations on their method have found use in spectral interferometry with the SPIDER technique [101] and also for measuring refractive index changes in partially ionized media [81]. To begin, the Fourier transform of equation 4.4 is taken:

$$\begin{aligned}\mathcal{F}\{I(X)\} = \mathcal{F}\{\epsilon(X)\} + \mathcal{F}\left\{\epsilon(X)\frac{\mathcal{V}}{2}\exp\left[\frac{ik_0 s}{z}\left(X-\frac{s}{2}\right)+i\Delta\phi\right]\right\} \\ +\mathcal{F}\left\{\epsilon(X)\frac{\mathcal{V}}{2}\exp\left[-\frac{ik_0 s}{z}\left(X-\frac{s}{2}\right)-i\Delta\phi\right]\right\} \qquad (4.6)\\ = DC + SB\left(\frac{k_0 s}{z}\right) + SB\left(-\frac{k_0 s}{z}\right) \qquad (4.7)\end{aligned}$$

where $\mathcal{F}\{...\}$ denotes the Fourier transform. For 'well-resolved' interference patterns[1], the absolute value of equation 4.6, plotted as function of the reciprocal space coordinate k, takes a distinctive form shown in the lower plot of figure 4.3. The three terms in equation 4.6 each form a distinct peak in the Fourier domain: a central 'DC' spike at zero spatial frequency flanked by two side-bands centered at plus and minus the fringe spatial frequency $\left(k = \frac{k_0 s}{z}\right)$. The separation of the peaks in the Fourier domain allows each term in equation 4.6 to be addressed individually.

Takeda et al. described a process for retrieving the phase $\Delta\phi$ from a fringe pattern of the form of equation 4.4. The algorithm can be described as follows:

[1] Well-resolved here means both the number of fringes under the diffraction envelope is large enough (>3 typically) and that the detector samples each fringe with a sufficient number of pixels (>4 typically).

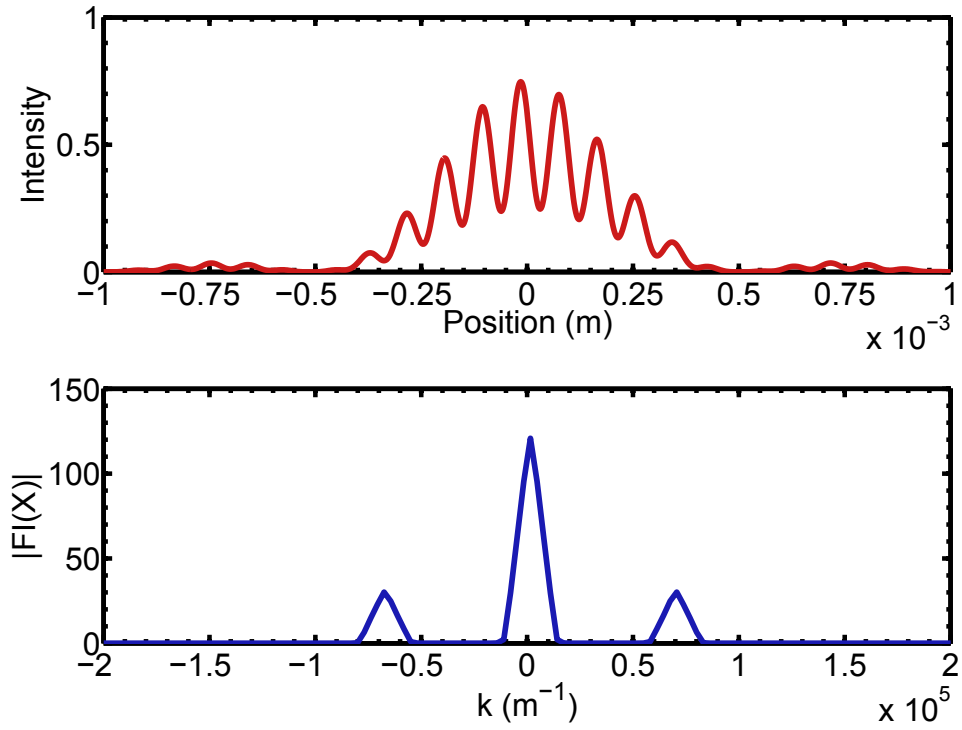

Figure 4.3: Upper plot: calculated fringe pattern produced by two 20 μm wide pinholes, separated by 350 μm, illuminated by $\lambda = 32$ nm light, recorded $z = 1$ m away. Illuminating conditions corresponding to $I_1 = I_2 = 1$, $\mathcal{V} = 0.5$ and $\Delta\phi = \frac{\pi}{3}$ were used. Lower plot: absolute value of the (spatial) Fourier transform of the fringe pattern from the upper plot, showing the formation of three distinct peaks.

1. Sideband isolation

   A single sideband $[SB(k)]$ of the Fourier transformed fringe pattern is filtered from the rest of the signal.

2. Shift to zero spatial frequency

   The isolated sideband is shifted to zero spatial frequency $[SB(k) \rightarrow SB(k - \frac{k_0 s}{z})]$.

3. Inverse transform

   The isolated, shifted sideband is inverse Fourier transformed back into real space.

4. Phase extraction

   The phase of the fringe pattern is extracted using:

$$\Phi_r = \mathrm{Arg}\Big\{\mathcal{F}'\Big[\mathrm{SB}\Big(k - \frac{k_0 s}{z}\Big)\Big]\Big\} \tag{4.8}$$

   where Arg{...} denotes the argument of the complex number enclosed in the braces and $\mathcal{F}'[...]$ is the inverse Fourier transform.

Considering the argument of the cosine in equation 4.5, we find that the extracted phase is equal to, in the case of SCIMTIAR, $\Phi_r = \Delta\phi - \frac{k_0 s^2}{2z}$. The first term, $\Delta\phi$, is equal to the difference in phase sampled locally by each pinhole: $\phi_2 - \phi_1$. Since, during the course of a SCIMITAR scan, one pinhole remains fixed in location, ϕ_1 is a constant, and thus $\Delta\phi$ records the beam spatial phase, evaluated at the location of pinhole 2, up to a constant offset.

Inspection of equation 4.6 shows that other properties of the illuminating radiation may be recovered from the fringe pattern. The peak at zero spatial

frequency [DC(k)] may be written as:

$$DC(k) = \mathcal{F}[\epsilon(X)] = (I_1 + I_2)\mathcal{F}\left\{a^2 \text{Sinc}\left[\frac{k_0 a}{2z}\left(X - \frac{s}{2}\right)\right]^2\right\}. \tag{4.9}$$

The maximum value of DC(k) is $I_1 + I_2$. Analogous to the situation for phase retrieval, the static pinhole of a SCIMITAR scan renders I_1 a constant, thus the maximum value of DC(k) can be used to recover the beam intensity profile through evaluation of I_2.

Additional information is contained in the filtered, shifted sideband [SB($k - \frac{k_0 s}{z}$)]. It can be shown that the fringe visibility can be found from:

$$\frac{|\mathcal{F}'[\text{SB}(k - \frac{k_0 s}{z})]|}{\mathcal{F}'[\text{DC}(k)]} = \frac{\mathcal{V}}{2}. \tag{4.10}$$

Knowledge of $\mathcal{V}$ and the intensity profile is all that is required for the determination of the complex coherence factor through equation 3.28. Hence, the extended form of the Fourier domain phase retrieval method described above, when applied to interference patterns produced by a SCIMITAR scan, allows the simultaneous recovery of the beam intensity profile, spatial phase and spatial coherence of light.

The success of the phase retrieval method is contingent on two-principle factors. Firstly, in step two of the algorithm, the sideband is shifted in the Fourier domain, in a process which essentially removes the fast-beating fringes from the single-slit diffraction envelope. However, it is feasible that the sideband can be translated by some incorrect additional amount, labelled here by δk. It can be shown that the retrieved phase is now given by $\Phi_r = \Delta\phi - \frac{k_0 s^2}{2z} - \delta k X$. In principle the slope of the phase, $\delta k X$, can be identified and removed from each recorded

fringe pattern.

A second potential systematic error comes from the original interference fringes. The Takeda method extracts a phase equal to $\Delta\phi - \frac{k_0 s^2}{2z}$, thus in order to gain access to the beam spatial phase the second term (we will call it the 'parabolic offset') must be removed. This introduces a potentially troublesome source of error, particularly for SCIMITAR, where the centre of the pinhole pair, and thus the centre of the whole interference pattern, changes for each pinhole separation measured. This means that $-\frac{k_0 s^2}{2z}$ takes a different value for each SCIMITAR data point. In principle, knowledge of the X-slit's shape and vertical position[1] allows $\frac{s}{2}$ to be estimated quite accurately, while the location of the sideband in Fourier space yields $\frac{k_0 s}{z}$, since this is just the spatial frequency of the interference fringes. Combining the two quantities allows the parabolic offset in Φ_r to be corrected for. It is noted that the visibility and intensity profile are insensitive to both errors in centering the side-band in reciprocal space and lateral shifts of the whole interference pattern.

The Takeda method (like nearly all other phase retrieval techniques, see [96] for more on this) yields a wrapped phase value: one that is bounded between $-\pi \leq \Phi_r \leq \pi$. This can be understood from fact that $\Im\{\ln[\exp(i\phi)]\}$ yields values of ϕ between the same bounds, where $\Im\{...\}$ denotes the imaginary part of the quantity enclosed by the braces. To retrieve the true phase value an integer multiple of 2π radians needs to be added (or subtracted) to the wrapped phase value. In the case of the wavefront of a diverging (converging) beam, the phase can increase (decrease) by many multiples of π over the transverse distance considered. A variety of algorithms to unwrap phase, in both one and

[1] Vertical position relative to that of the horizontal slit.

two dimensions, are widely available [96]. However, unwrapping will (potentially) fail if the phase difference between two consecutive data points is larger than 2π. In the case of SCIMITAR, care must be taken to not space data points too coarsely, especially at large pinhole separations (corresponding to large distances from the beam centre) where the spatial phase is expected to change more rapidly with position because of the quadratic phase offset identified earlier in this section.

4.3 Limitations

The SCIMITAR technique is subject to limitations in both the scope and accuracy of the retrieval of the beam spatial properties. The interferometric nature of the measurement is one source of such limits. There is a minimum distance the two-pinholes may be separated that can give rise to measurable interference fringes. In the Fourier domain, this is manifest as the 'collision' of the sidebands with the 'DC' term for small pinhole separations. The consequence of this effect is most apparent in the intensity profile recovery (see figure 4.7 for an example), where a clear gap in the data points is observed when the pinholes were too close to retrieve meaningful information. One might expect that intensity (but not coherence) information should still be recorded at small/zero pinhole separations, however we found this did not hold in our experiments. Imaging the X-slit itself with a microscope revealed that, due to resolution limitations in the laser machining process, the X-slit was up to 100% wider at its centre than elsewhere. The microscope image captured using a CCD is shown in figure 4.1, clearly displaying this widening at the slit centre. This meant that data patterns recorded for the very smallest pinhole separations could not be compared with the rest of the data

set.

Several factors affect the maximum pinhole separation that can be employed. Detectors, such as CCDs, are formed of an array of pixels. Interference fringes are modulations in the spatial domain, so, in order for the pattern to be imaged accurately, it must be sampled with sufficient resolution. For pinholes separated by s, illuminated by radiation of wavelength λ and a pinhole-detector distance z, the fringe spacing is $\Delta X = \frac{\lambda z}{s}$. If we demand that the fringes are separated by no less than m pixels of width w, then we may write an expression for the maximum permissible pinhole separation:

$$s_{\max} = \frac{\lambda z}{mw} \tag{4.11}$$

which, for experimental parameters pertinent for the SCIMITAR demonstration described in this chapter ($\lambda = 30$ nm, $z = 1.22$ m and $w = 20\ \mu$m), and for $m = 4$, equation 4.11 yields $s_{\max} = 610\ \mu$m. In the case of SCIMITAR, the maximum pinhole separation is also the maximum distance from the beam centre that information can be retrieved on the wavefront and intensity distribution. In other words the spatial properties over distances greater than $s_{\max}$ from the centre cannot be accurately measured.

Another limitation arises from the finite fringe visibility. In section 4.2 the Fourier domain sideband was used to extract the fringe phase. However the magnitude of the sideband depends on the visibility of the fringe pattern. Hence, locating the sideband in the presence of experimental noise becomes challenging when the fringe visibility is low. Low visibility can be caused by both poor spatial coherence and a large difference in the relative beam intensity values sampled by

the two pinholes. If the sideband is not identified and isolated successfully our analysis method is invalid. In the extreme limit, no fringes would be observed for incoherent illumination and thus phase retrieval is impossible.

A further issue with SCIMITAR is related to drifts and fluctuations in the light source itself. They can be characterized by their inherent time-scales: fast fluctuations on the order of some fraction of the CCD exposure time and slower drifts on the scale of some fraction of the scan duration. In the presence of fast fluctuations in the source pointing for instance, one would expect that for a relatively long CCD exposure time interference fringes might wash out. Considering a longer time scale, a drift in the intensity and/or phase sampled by the 'static' pinhole would mean that data points taken at the beginning of a scan could not be accurately compared to those acquired later in time. Consequently, a radiation source with relatively stable properties (both on short and long timescales) is needed.

4.4 First Experimental Demonstration

The SCIMITAR technique was demonstrated by characterizing the spatial properties of HHG from a gas cell. A diagram of the experimental arrangement is found in figure 4.4. Laser pulses with a repetition rate of 1 kHz, an energy of 180 μJ and pulse duration of approximately 40 fs (determined by a single-shot autocorrelator) were focussed by a f/11.8 lens into a gas cell. The cell was formed from a hollow nickel tube, sealed at one end with vacuum compatible epoxy and pressed to an approximate thickness of 1 mm. It was backed, from the open end, by 170 mbar of argon. The focussed laser beam drilled both entrance and

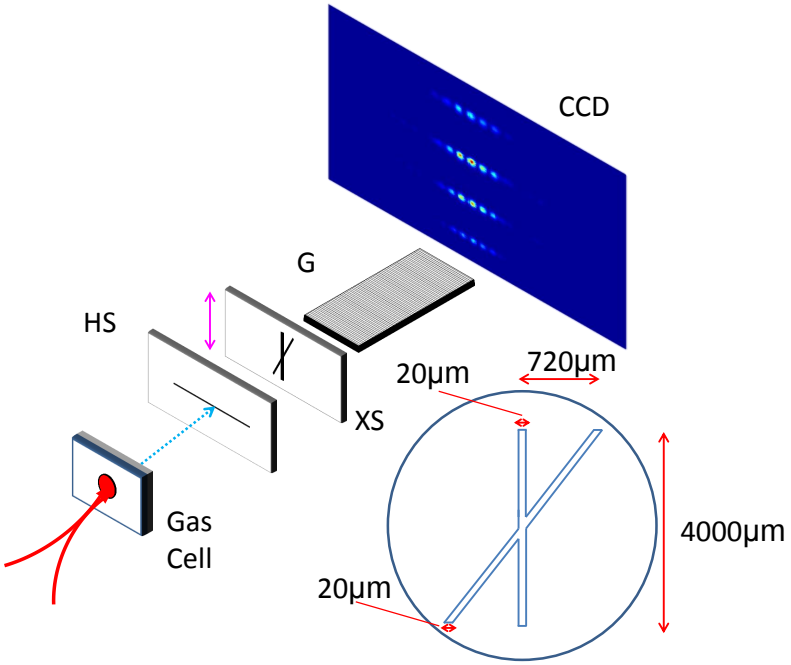

Figure 4.4: Diagram of SCIMITAR experimental layout. The laser beam (red line) is focused in to a gas cell, producing high harmonics (blue dotted line) which propagate to the SCIMITAR diagnostic, composed of a horizontal slit (HS) and X-slit (XS). The resultant interference patterns are imaged in a grating spectrometer, composed of a diffraction grating (G) and CCD. The inset shows a schematic of the X-slit.

exit holes into the thin walls of the tube. The interaction of the intense laser pulse with the argon produced high harmonic radiation. The X-slit and horizontal slit were placed ≈ 0.62 m downstream of the gas target. After the residual infrared beam was blocked using a 200 nm thick aluminium filter, orders up to $q = 29$ were observed using a flat-field XUV spectrometer, composed of a spherical variable-line-spaced grating (ruled with 1200 lines/mm) and a cooled, x-ray CCD (Pixis XO, Princeton Instruments). The CCD was placed approximately 1.22 m downstream of the X-slit. An example CCD exposure, recorded for a pinhole separation of 193 μm, is shown in figure 4.5.

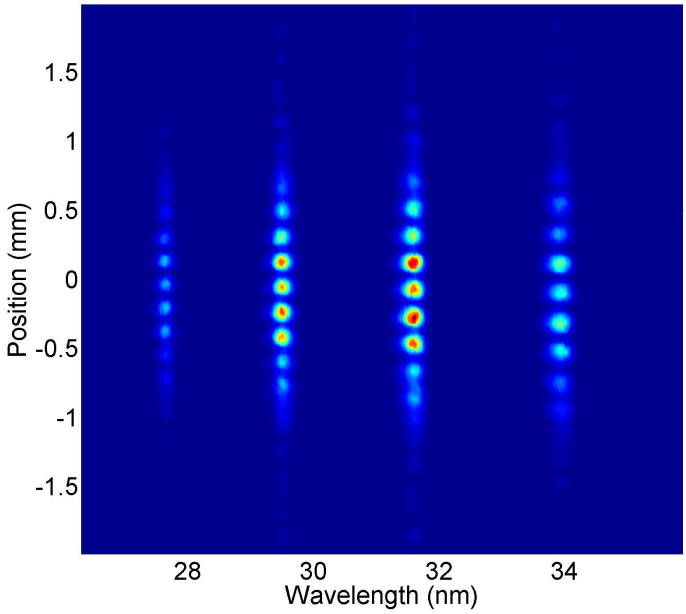

Figure 4.5: Example CCD acquisition, recorded during the course of a SCIMITAR scan, for a pinhole separation of 193 μm. A 45 second exposure was employed, corresponding to the harmonic signal from approximately 45,000 consecutive laser shots.

The X-slit was mounted on a vertical translation stage driven by an electric

motor. The vertical position of the X-slit (y) was read off from a mechanical clock gauge. Knowledge of the X-slit design, in particular the angle between the two slits which form the aperture, allowed the (relative) pinhole separation to be determined from the slit vertical position using $s = (y - y_0)\tan(\theta)$, where y_0 is the vertical position corresponding to zero pinhole separation and θ is interior angle made between the horizontal and angled bars of the X-slit. The zero pinhole separation vertical position (y_0) can be determined experimentally from the recorded series of interference patterns. A convention is used here, where negative (positive) values of s correspond to the case where one pinhole is to the right (left) of the central pinhole, as observed by the impinging light.[1]

In the experimental run described here, 28 different pinhole separations were employed, ranging from $s = -465$ μm to $s = 479$ μm. Measurable interferograms were observed for four harmonic orders (23, 25, 27, 29) at each pinhole separation.[2] An example interference pattern for $q = 25$ is shown in the upper plot of figure 4.6. The lower plot shows the high harmonic spectrum, found by integrating over the interference signal in the spatial domain. A thin nickel mesh was used to support the aluminium filter which introduced additional modulations to the recorded fringe pattern (see the upper plot of 4.6). However, owing to the use of Fourier domain analysis, the influence of the mesh could be isolated and filtered without adversely affecting the quality of the desired two-pinhole interference patterns.

In order to benchmark the fidelity of the SCIMITAR technique for recovering the beam intensity and spatial phase profiles, a SWORD measurement was

[1] This convention is maintain throughout this thesis, although on occasion ΔX is used in place of s.

[2] Owing to the absorption properties of argon orders lower than $q = 23$ were not observed.

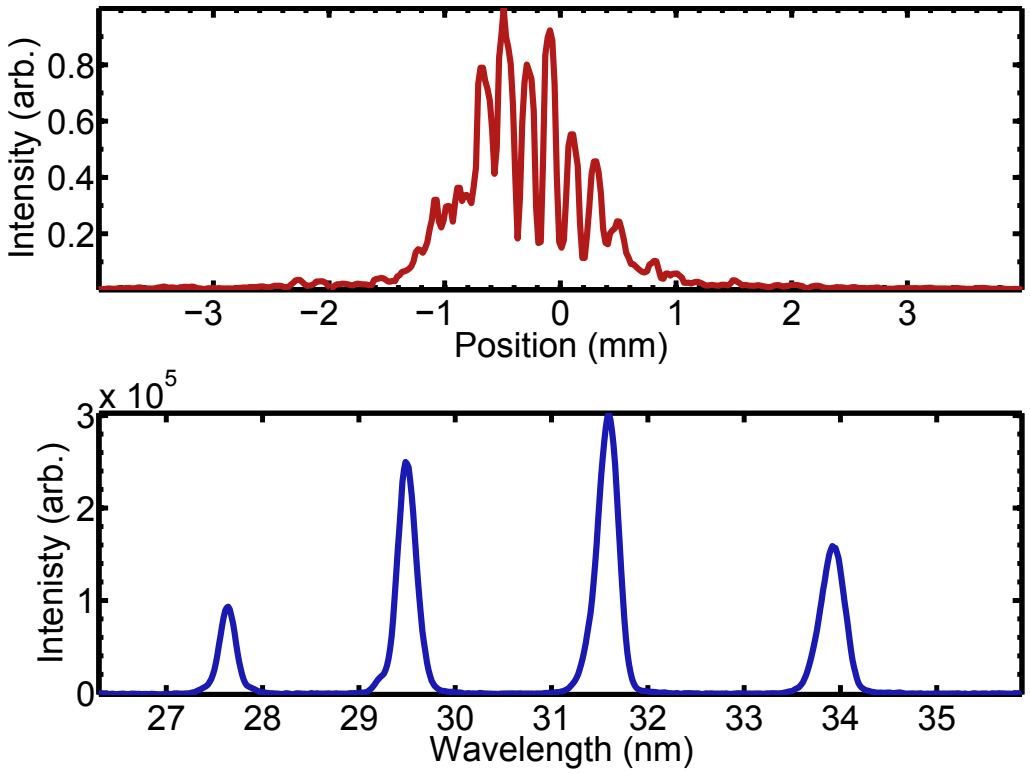

Figure 4.6: Upper plot: an example of a two-pinhole interference pattern for $q = 25$, taken during the SCIMITAR scan. The presence of the filter mesh contributes to the observed asymmetry of the pattern. Lower plot: experimental high harmonic spectrum, showing from left to right harmonic orders 29, 27, 25 and 23.

made immediately after the SCIMITAR scan. Both the X-slit and the horizontal slit were removed and replaced with a single 20 μm wide pinhole, attached to a mechanical vacuum manipulator, the position of which was determined by a micrometer. Such an arrangement allowed the pinhole to be scanned horizontally across the beam. At each pinhole position a diffraction pattern was recorded using the same imaging spectrometer as used for the SCIMITAR measurement.

4.4.1 Recovered Harmonic Intensity Profile

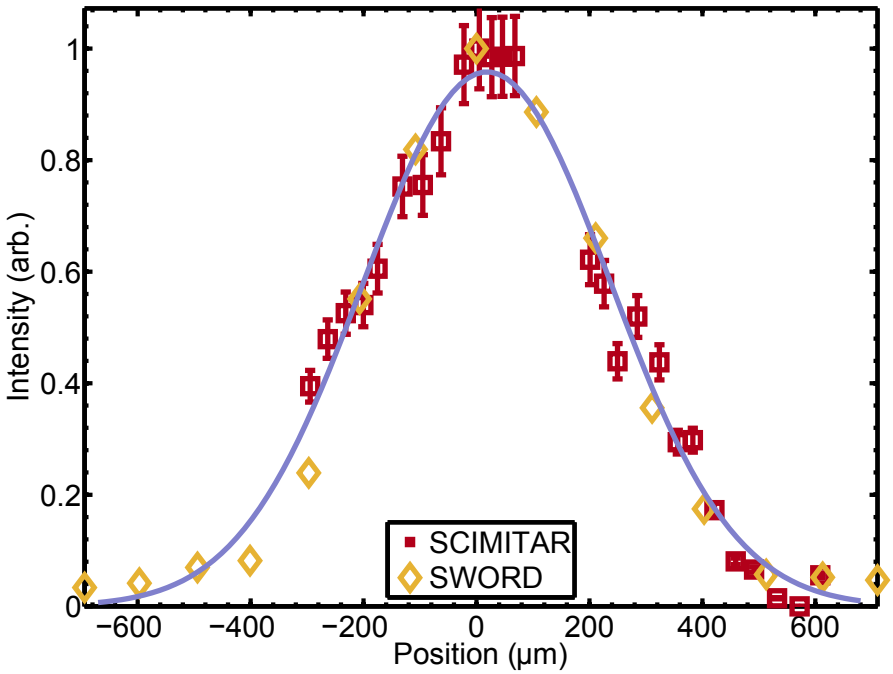

Figure 4.7: Recovered intensity profile for $q = 23$. The red squares correspond to the SCIMTAR data points. The gold diamonds are SWORD data points taken under the same experimental conditions. The error on the SWORD data points was found to of the order of 1 % and thus smaller than the symbol size. The mauve solid line is a Gaussian fit to the SCIMITAR data, with a full width at half maximum (FWHM) of 515 $\pm$ 29 μm.

The transverse intensity profiles were recovered for the four harmonic orders using both the SCIMITAR and SWORD methods. The results of the two measurements, for $q = 23$, are overlaid in figure 4.7.

The harmonic beam profile is observed to be well described by a Gaussian function, having a similar shape to previously reported results [28, 33, 70]. Excellent quantitative agreement between SCIMITAR and SWORD is found, validating the former technique. The SCIMITAR errorbars were calculated by fixing the pinhole separation and taking four consecutive acquisitions. The errorbar size is equal to the standard error from the four measurements. The error was extrapolated to all other data points by assuming an identical fractional error for each point.

A gap in the SCIMITAR data is located around 100 μm is due to the pinhole separation being too small there to retrieve accurate information on the beam intensity. This was due to limitations in the precision of the laser machining of the X-slit as evidenced in figure 4.1. We will refer to the transverse position of the X-slit centre as the 'zero-separation location' (x_0).[1] Ideally this gap in the data should correspond with the beam centre. The only consequence of the small transverse misalignment of the X-slit transverse position here is that a smaller signal is measured for a given CCD exposure time compared to the case where the static pinhole is aligned exactly at the central, most intense, part of the harmonic beam.

[1] Equivalently this is the location of the static pinhole.

4.4.2 Recovered Harmonic Wavefront

Extracting the phase of the fringe patterns produced by the SCIMITAR scan yields $\Phi_r = \Delta\phi - \frac{k_0 s^2}{2z}$. The parabolic offset was evaluated and removed, alowing $\Delta\phi$ to be evaluated. By unwrapping the phase $\Delta\phi$, the beam spatial phase profile was recovered.

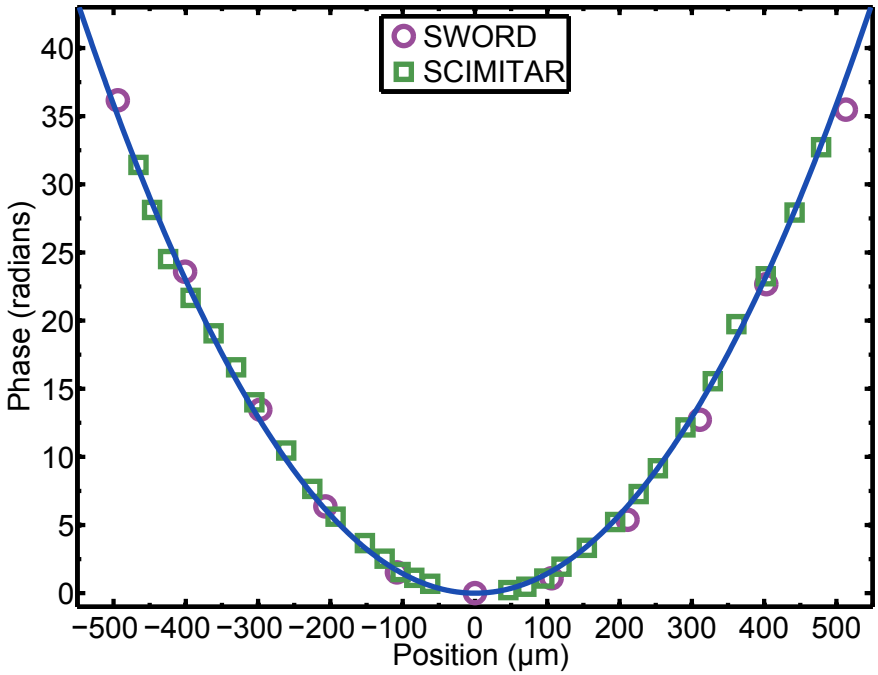

Figure 4.8: Harmonic spatial phase profile retrieved using SCIMITAR (green squares) and SWORD (purple circles) for $q = 23$. A parabolic fit to the SCIMITAR data is given by the blue solid line. The fit corresponds to a wavefront with a radius of curvature (R_p) of 0.630 ± 0.013 m. Errorbars are smaller than the symbol size for all data points.

The wavefront recovered using both SCIMITAR and SWORD is shown in figure 4.8. Excellent agreement is again observed between SCIMITAR and SWORD data. A parabola was fitted to the SCIMITAR data, shown by the blue line in figure 4.8, corresponding to a wavefront with a radius of curvature (R_p) equal to

0.630 ± 0.013 m.[1] This is in good agreement with the measured distance between the gas cell and X-slit of 0.62 m. The spectral variation of R_p is explored later in chapter 5.

4.4.3 Recovered Harmonic CCF

For each harmonic order the fringe visibility was extracted as a function of pinhole separation. The CCF (μ) was calculated from equation 3.28. In figure 4.9 the variation of $|\mu|$ with pinhole separation is shown for $q = 23$.

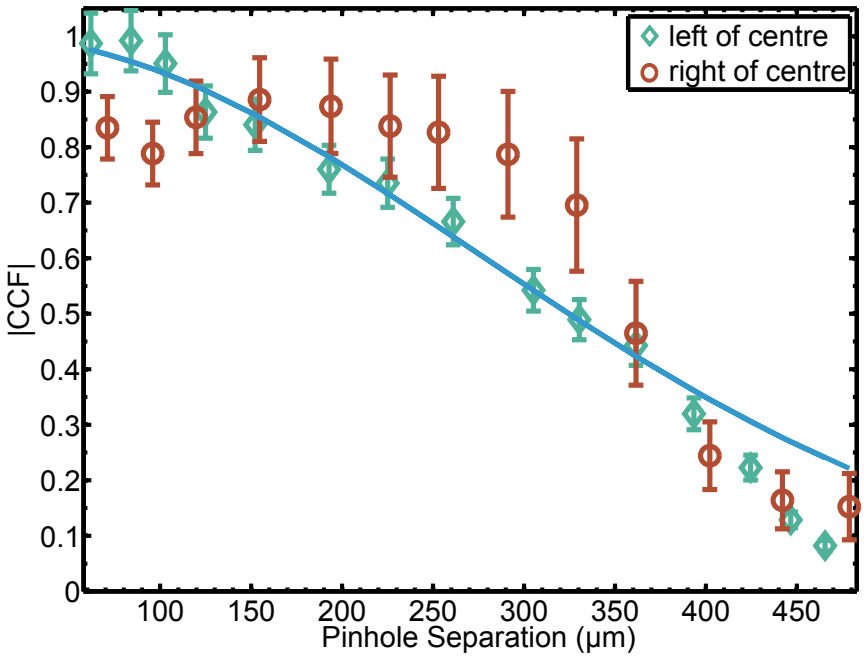

Figure 4.9: Absolute value of the complex coherence factor (CCF) for $q = 23$. The variation both left (green diamonds) and right (brown circles) of the static pinhole is shown. The solid blue line is a Gaussian fit to all data points of FWHM $649 \pm 47\mu$m. The errorbars are calculated (and extrapolated) from the variation recorded over 4 measurements at single fixed pinhole separation ($s = -261\mu$m.)

[1]The subscript 'p' denotes a quantity in the plane at which the SCIMITAR (or SWORD) measurement was made: the *propagation* plane.

To recap: during a SCIMITAR scan one pinhole remains at the beam centre, allowing the CCF variation with pinhole separation to be measured both left and right of the beam centre. Since a 45 second CCD exposure was used for each data point, each CCF data point represents the average over approximately 45,000 harmonic pulses.

In figure 4.9, generally, the CCF decreases as the pinhole separation increases. This is consistent with a partially coherent field, where the strength of correlation at two test points falls off with increasing point separation. There is a slight difference in the CCF measured for the left and right halves of the beam which is not quite accounted for by the experimental uncertainty of the measurement, quantified by the errorbars in figure 4.9. This result implies that the harmonic CCF is not shift invariant, since figure 4.9 shows that specifically $|\mu(s)| \neq |\mu(-s)|$. The left of centre CCF (green diamonds) monotonically decreases with position, whereas the right of centre CCF (brown circles) increases up until $s = 200\,\mu$m before falling monotonically with increasing pinhole separation.

The possibility of an asymmetry in the harmonic CCF has not been reported previously, in large part because of the way spatial coherence has been measured. Studies by Bartels et al. [72] and Ditmire et al. [85] made use of slit pairs, each with a different slit separation, aligned such that the midpoint between the pair coincided with the centre of the harmonic beam. This arrangement would not record any potential asymmetry in the CCF.

In section 3.5 an expression was derived for the CCF of a source of high harmonic radiation. Although the model deals with the generation process and SCIMITAR measures the propagated radiation (away from the source), the model may still shed light on the results presented in this chapter. Specifically, it pre-

dicts that if pinholes are placed symmetrically (locations 'L' and 'R' in figure 4.10), as they were for the studies of Bartels and Ditmire, the measured CCF would be larger than if they were placed otherwise[1]. This is due to the dipole phase contribution to the degradation of the harmonic CCF being minimised in 'symmetric' case. Measuring the spatial coherence with one pinhole at the centre and another elsewhere in the beam (locations 'M' and 'S' in figure 4.10), as is the case for SCIMITAR, would yield a comparatively smaller CCF value. Such a result is also predicted by the theoretical work of Salieres et al. [71] in their numerical modelling of the HHG process.

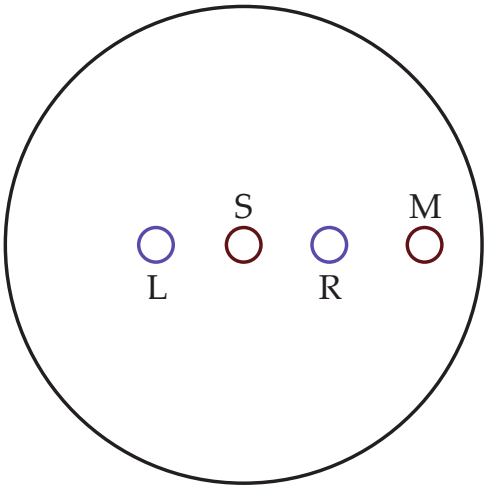

Figure 4.10: Diagram showing the positioning of two pinhole pairs with respect to a beam represented by the large black circle. The pinholes labelled 'L' and 'R' are typical of Thompson-Wolf type experiments where pinholes are positioned symmetrically about the beam centre. Pinholes labelled 'M' and 'S' are typical for SCIMITAR.

In our case, the measured asymmetry in spatial coherence may originate from different generation conditions left and right of the beam centre, either through small asymmetries in the focal spot distribution or a gradient in the gas pressure,

[1] Assuming the pinholes remain fixed in their separation.

as considered in [86]. Alternatively, the fact that the 'static' pinhole was not located at the centre of the beam may be important. Owing to a small transverse misalignment of the X-slit, the 'static' pinhole in our case was located just off of the beam centre (position 'L' in figure 4.10). For a shift-invariant beam this misalignment would have no effect on the CCF measurement, but here the clear asymmetry in μ presented in 4.9 implies the CCF depends on the relative position of the two test points and not just their separation alone.

Closer inspection of figure 4.9 shows that $|\mu|$ increases around $s = 200\,\mu$m for the CCF right of centre. Owing to the slight misalignment of the X-slit, for this particular data point only were the pinholes equidistant from the centre of the beam. To be clear, in this one case only their locations are closer to the 'L' and 'R' positioning than 'M' and 'S', as per figure 4.10. The model for the harmonic coherence properties found in section 3.5 predicts that sampling the CCF symmetrically about the beam centre ('L' and 'R' locations) would yield a higher value of μ than if the pinholes were placed as at $x_1 = 0$ and $x_2 = s$ ('M' and 'S' locations). This is because the dipole phase contribution to the harmonic coherence is minimised for any two locations equidistant from the beam centre. The asymmetry we observe in the harmonic CCF, including the peak at $s = 200\,\mu$m, may well directly result from the effect of the dipole phase on the harmonic spatial coherence.

It is worth mentioning that previous measurements of the spatial coherence of HHG typically recorded interference patterns at only a few pinhole separations, for example the studies of Ditmire et al. [85] and Bartels et al. [72]. In both cases, only a very coarse sampling of the spatial coherence variation with pinhole separation was made. This is compared with the present work in which the CCF

was measured at 28 different pinhole separations. Such a detailed measurement allows us to observe features like the local peak in the spatial coherence for the right of centre CCF around $s \approx 200\,\mu$m.

4.4.4 Variation with Harmonic Order

For the sake of brevity, only the spatial properties of $q = 23$ have been shown so far. However, the same information was acquired for orders 25, 27 and 29. The intensity full width at half maximum (W_{pI}), wavefront radius of curvature (R_{p}) and FWHM of a Gaussian function fitted to the CCF (W_{pC}) are summarised in table 4.1. An additional parameter, the coherent fraction, $q_{\mathrm{IC}} = \frac{W_{\mathrm{pC}}}{W_{\mathrm{pI}}}$, is included in the fifth column.

Harmonic Order	R_{p} (m)	$W_{\mathrm{pI}}(\mu\mathrm{m})$	$W_{\mathrm{pC}}(\mu\mathrm{m})$	q_{IC}
23	0.630 ± 0.014	515 ± 29	649 ± 47	1.26 ± 0.12
25	0.635 ± 0.021	424 ± 37	633 ± 38	1.49 ± 0.16
27	0.659 ± 0.027	414 ± 27	574 ± 37	1.38 ± 0.13
29	0.642 ± 0.025	414 ± 48	528 ± 32	1.28 ± 0.17

Table 4.1: Table showing the variation with harmonic order of the spatial phase radius of curvature (R_{p}), intensity width (W_{pI}), coherence width (W_{pC}) and coherent fraction (q_{IC}).

Broadly speaking, R_{p} increases, W_{pI} decreases and W_{pC} also decreases with harmonic order, however quantitative relationships between q and these properties are not clear due to only four harmonic orders being measured. In addition, we find q_{IC} is approximately equal for $q = 23 - 29$ and always greater than one. Practically speaking this means that the most intense part of the beam possesses high coherence. A more detailed investigation of the spectral dependence of the harmonic spatial properties is reported in chapter 5.

4.5 Summary

In this chapter a new technique for characterizing the spatial properties of light has been described, called SCIMITAR. Through recording the interference patterns produced by a variable-separation two-pinhole interferometer the beam intensity profile, spatial phase profile and CCF can be measured. Including a diffraction grating in the arrangement allows the spectral variation of the beam properties to be investigated.

To demonstrate SCIMITAR the spatial properties of HHG driven by 40 fs duration laser pulses were measured. The results were validated by performing a SWORD measurement under the same experimental conditions. Excellent agreement between the two techniques was observed. The harmonic intensity profiles were found to be close to Gaussian in shape while the harmonic wavefronts were well described by parabolas of differing degrees of curvature. A small difference in the CCF measured left of centre compared to right of centre may be explained as resulting from the effect of the harmonic dipole phase on the spatial coherence.

Chapter 5

Order Dependent Spatial Properties of HHG

The coupling between different degrees of freedom of an ultrashort pulse of light can be both a hindrance and a help depending on the experimental situation. In the case of high harmonic generation, the strongly non-perturbative nature of the XUV emission means that different frequency components of the spectrum may be generated under different conditions within the medium. This can give rise to, for instance, a spectral dependence of the spatial properties of HHG, as explored by Frumker et al. [34] with their study of the wavefront and intensity profiles of high harmonics generated in nitrogen. In this chapter their work is repeated and extended, by considering a new spectral region and, through SCIMITAR, an additional beam property: the spatial coherence. Furthermore, the coupling between spectral and spatial domains within the HHG source itself will be explored by application of the Gaussian-Schell model.

In chapter 4 the results of the first demonstration of the SCIMITAR technique were described, where the spatial characterization of harmonic orders 23–29 was undertaken. In order to simultaneously characterize both more numerous and higher order harmonics, modifications to the experimental arrangement were re-

quired.

A number of approaches to extending the HHG cut-off frequency ($\nu_{\max}$) are neatly encompassed in equation 2.6, which can also be expressed as:

$$E_{\max}[\text{eV}] = h\nu_{\max} = I_{\text{p}} + 2.99 \times 10^{-13} I_0[10^{14}\ \text{W cm}^{-2}]\lambda^2[\mu\text{m}] \tag{5.1}$$

where h is Planck's constant, I_{p} is the ionization potential of the atom, I_0 is the peak laser intensity and λ is the fundamental wavelength. Increasing $\nu_{\max}$ can be achieved by increasing I_{p}, either through using pre-ionization to generate harmonics from ions[1] or through using a different generating gas (neon and helium both have a higher ionization potential than argon, for instance). However, both situations are accompanied by a decrease in the expected photon flux, owing to unfavourable phase-matching conditions and/or reduced single atom response.

Alternatively, the scaling of the ponderomotive potential with driving laser wavelength can be used to increase the cut-off. However, a longer laser wavelength leads to a longer electron excursion time, allowing for more quantum diffusion of the wavepacket and, in turn, a lower recombination probability, affecting the efficiency of conversion of the IR laser light into the XUV. This can be compensated, somewhat, through the fact that the phase-matching pressure is higher for longer wavelengths [88], potentially providing a larger harmonic signal. However, the technical demand of producing high energy, short duration pulses with wavelengths much longer than 1 micron is significant, with complex multi-stage optical parametric amplifiers the preferred method [20].

Naively, one might expect that simply increasing the energy in the laser pulses

[1] Preionization changes the atomic charge state the returning electron encounters and effectively increases I_p in equation of 5.1.

driving the HHG source would lead to an increase in the harmonic cut-off through the scaling with I_0, and this would be true for the case of a single atom. However, in the macroscopic picture, increasing I_0 also gives rise to an increase in the level of ionization. As was shown in section 2.3.1, phase-matching in HHG is limited to certain (low) levels of ionization. Simply increasing the pulse energy leads to the ionization of a larger fraction of atoms by the time the highest pulse intensities are reached, hindering phase-matching of the highest harmonic orders. In combination with this temporal aspect is a deleterious spatial effect whereby the fundamental beam is defocussed by the refractive index profile created by the population of free electrons. Therefore the peak laser intensity which may be achieved in vacuum is not possible in the presence of a gas.

Alternatively, I_0 may be increased by decreasing the pulse duration. On the rising edge of the pulse the number of free electrons increases around the temporal peaks of the laser cycle. For shorter pulses (with fewer cycles) a higher peak intensity can be achieved before the ionization fraction reaches too high a level for phase-matching to occur. Thus, the use of shorter duration laser pulses can provide a means of increasing the harmonic cut-off and 'out-running', so to speak, the deleterious effects of ionization.

5.1 Pulse Compression

Temporal pulse compression was chosen as the route to extend the harmonic cut-off for experiments described in this chapter. The durations of pulses produced by commercial femtosecond laser amplifiers tend to be close to transform limited and are generally longer than 30 fs in duration. In order to further decrease the pulse duration the bandwidth must be increased. Additionally, the spectral phase of the

broadened pulse must be manipulated to compress the wide bandwidth to as short duration as possible. Previously, two main techniques have been demonstrated for producing so called 'few-cycle' (pulse duration < 12 fs for $\lambda = 800$ nm) laser pulses, with energies of several hundred microjoules.

Filamentation of femtosecond pulses is a widely studied phenomena with applications in weather manipulation [103] and remote sensing [124]. When a pulse is focussed into an extended region of gas, self-guiding can occur through the production of a stable filament. The competition of self-focussing from a positive second order effect ($\propto n_2 I$) with a fourth order self-defocussing effect ($\propto n_4 I^2$) can lead to the formation of a long region where the pulse is confined close to the optical axis. The non-linear interaction present in the filament can lead to self-phase modulation. This is turn may broaden the pulse spectrum and alter the spectral phase [65]. The correct combination of both can lead to pulse compression in one step, producing pulses with durations shorter than 7.4 fs [84], or with additional external spectral phase compensation, the production of shorter than 6 fs pulses [25]. However questions remain over the long term stability and repeatability of the technique, coupled with the presence of severe space-time coupling in the generated pulses [18].

An alternate approach to pulse compression, utilised in experiments described in this chapter, separates the broadening and spectral phase compensation into two distinct steps and is capable of producing pulses shorter than 5 fs in duration [61]. The laser beam is coupled into a long, thin, hollow-core glass fibre (HCF) filled with a noble gas. The extended interaction region and adjustable gas pressure offer control over the self-phase modulation (SPM) which takes place in the fibre (see figure 5.1 for the effect of SPM on the spectrum of a $\tau \approx 40$ fs dura-

tion laser pulse). The spectrally broadened pulse is re-collimated and reflected

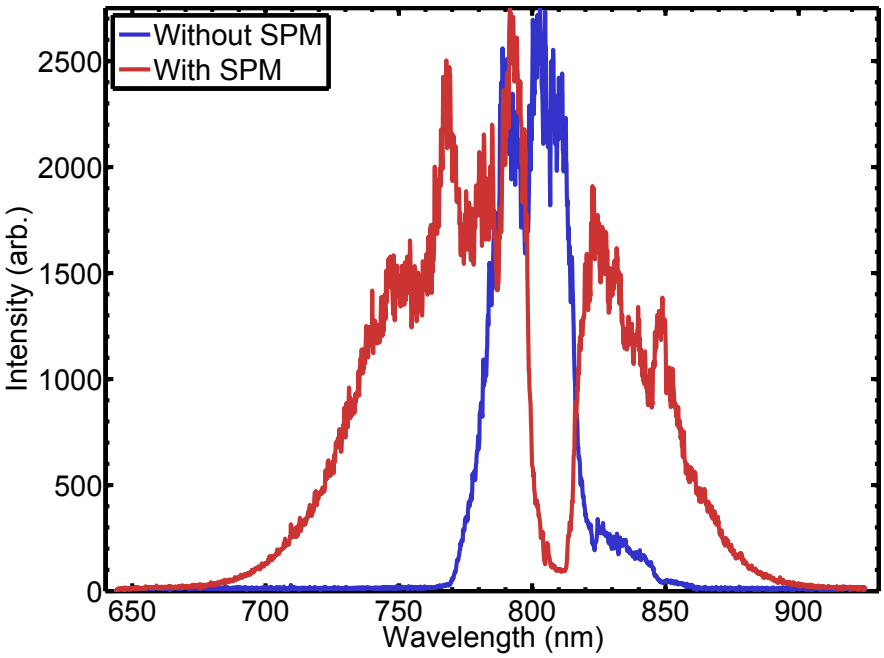

Figure 5.1: Laser spectrum with (red line) and without (blue line) self-phase modulation. In the former case the HCF was differentially pumped, with the exit backed with 300 mbar of argon. In the latter case the fibre was evacuated to a pressure < 1 mbar.

off a set of specially engineered, chirped mirrors [77]. Each reflection imparts a fixed amount of (negative) chirp, compensating (to some degree) for the spectral phase acquired during propagation through the fibre. Fine tuning of the chirp is possible through changing the insertion of a thin, glass pair of wedges. This technique also benefits from producing beams with excellent, aberration free spatial distributions, since propagation through the fibre acts as a spatial filter.

In order to mitigate the onset of ionization effects in the HCF (for instance, mode-coupling from ionization-induced defocussing) , a pressure gradient can be set up, with the entrance of the fibre evacuated to low pressure and the exit of the

fibre backed by a noble gas. The benefits in terms of both increased transmission and enhanced spectral broadening have been described by Robinson et al. [50], who showed that the duration of the generated, near transform-limited pulses could be tuned by changing the backing pressure.

For a pulse with a Gaussian temporal envelope, in the absence of dispersion, the frequency bandwidth gained ($\Delta\omega$) after propagating a distance L in a differentially pumped fibre with an exit pressure of p_L is given by [50]:

$$\Delta\omega = \frac{\kappa\zeta p_L}{\sqrt{L}} \int_0^L \sqrt{z}\exp(-\alpha z)\mathrm{d}z \tag{5.2}$$

where ζ is the coupling coefficient, α is the absorption coefficient and

$$\kappa = \frac{0.86\omega_0\eta_2 P_0}{\tau_0 c A_{\text{eff}}} \tag{5.3}$$

where ω_0 is the laser angular frequency, η_2 is the nonlinear coefficient, P_0 is the laser peak power, τ_0 is the initial pulse duration, c is the speed of light (in vacuum) and A_{eff} is the effective mode area of the fibre. The Fourier-limited bandwidth (τ_{FL}) of a (Gaussian) pulse of bandwidth ω is given by $\tau_{\text{FL}} = 0.44 \times 2\pi/\omega$. In the presence of SPM the Fourier-limited pulse duration can be written as:

$$\begin{aligned} \tau_{\text{FL}} &= \frac{0.44 \times 2\pi}{\omega_1 + \Delta\omega} \\ &= \frac{2.76}{\omega_1 + \kappa' p_L} \end{aligned} \tag{5.4}$$

where ω_1 is the pre-SPM laser bandwidth and $\kappa' = \Delta\omega/p_L$ as per equation 5.2.

5.1.1 HCF Compressor Performance

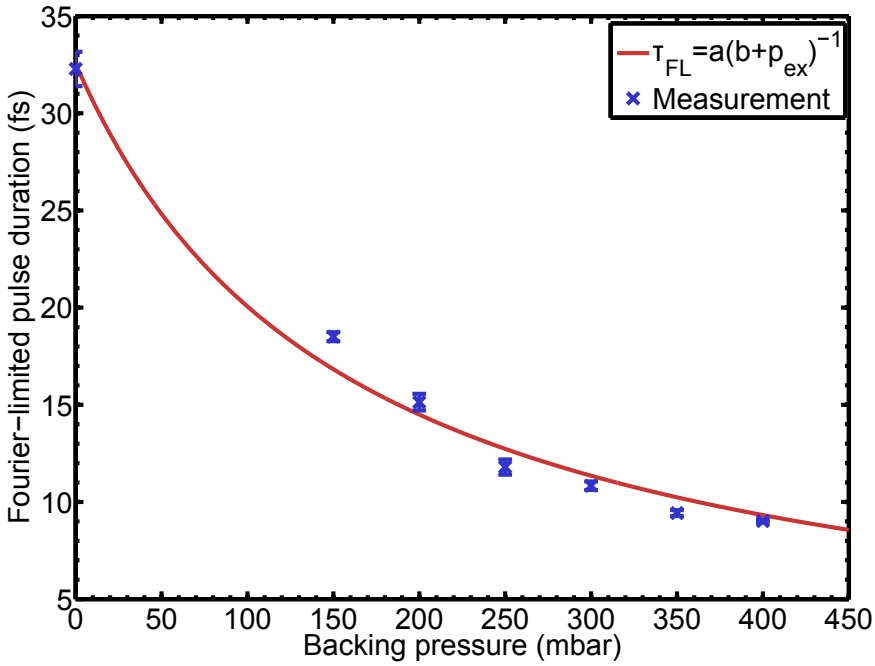

Figure 5.2: Deduced Fourier-limited pulse duration (calculated from the measured spectrum) as a function of the hollow fibre gas pressure (blue crosses). Errorbars display the standard error from five spectrum acquisitions; each single acquisition is the sum of approximately 100 laser shots. The solid line is a fit of equation 5.4.

Pulses with an initial duration of 40 fs, produced by a Titanium:Sapphire CPA laser system, were spectrally broadened in a hollow core fibre (with a length of 1 m and a 250 μm inner diameter), differentially filled with argon. A set of chirped mirrors enabled spectral phase compensation: each reflection imparted -40 fs mm^{-1} of group velocity dispersion (typically eight reflections are required to achieve the shortest pulse durations). The spectral broadening was investigated by measuring the laser spectrum after the fibre exit as a function of backing pressure. The (FWHM) transform-limited pulse duration was calculated by inverse

transforming (the square root of) the recorded spectrum. The variation of the transform-limited pulse duration with backing gas pressure is shown in figure 5.2.

Pressures beyond 500 mbar were not used owing to the observation of degradation in the laser spatial profile measured after the fibre exit, possibly due to the onset of ionization effects. Nonetheless, figure 5.2 shows pulse durations below 10 femtoseconds should be achievable if proper chirp compensation were employed. Furthermore, the close fit of equation 5.4 to the transform-limited pulse duration, shown by the red line in figure 5.2, indicates that the system should produce laser pulses with an easily tunable duration. It should be noted that even shorter pulses have been produced using similar equipment by other research groups [50, 61], however, in our case, where we need only to extend the harmonic cut-off, pulse durations in the region of 10–15 fs were sufficient.

5.1.2 Measuring Few-cycle Pulses

In section 3.3, techniques for measuring the temporal properties of ultra-fast laser pulses were described. An additional technical issue arises when attempting to characterize pulses in the 'few-cycle' regime: the broad spectral bandwidth challenges the performance of optics used within characterization devices. In experiments described in this thesis a commercial implementation of a variant of the FROG device known as GRENOUILLE[1] was used, with a quoted minimum measurable pulse duration of 9 fs [69]. The GRENOUILLE produces an experimental trace which may be thought of as a frequency-resolved autocorrelation. A generalised projection algorithm is used to retrieve the pulse temporal information. In addition, the GRENOUILLE can measure the beam spatial chirp (its

[1] Grating Eliminated No-nonsense Observation of Ultrafast Incident Laser Light E-fields.

presence causes the experimental trace to rotate) and pulse front tilt (causes a shift along the 'time' axis of the trace). In this section any pulse durations quoted were read directly from the GRENOUILLE software, following careful alignment of the device.

5.2 Observed Cut-off Extension

The high harmonic spectra produced by the compressed and characterized laser pulses were investigated. The new experimental arrangement is depicted in figure 5.3.

Beyond the addition of the HCF and chirped mirrors, other modifications to the beamline were made. Prior to the fibre, a home-built laser pointing stabiliser was installed. In addtion, flow-meters were added to regulate the gas flow in to both the HCF and HHG gas cell. Previously the steering optics used in the beamline were mainly broadband[1] coated dielectric mirrors. They we all replaced with equivalent ultra-broadband[2] metallic coated mirrors to match the broadened laser spectrum while minimising GVD. The focussing lens was replaced with a spherical mirror with a radius of curvature of 0.75 m (corresponding to a focal length of 0.375 m). To avoid astigmatism, the beam was reflected at a small angle of incidence ($\approx 1.6^\circ$ in our case). It can be shown, under the small angle approximation, the longitudinal separation of foci in the horizontal and vertical directions (Δf) as a fraction of the Rayleigh range (z_r) can be expressed as:

$$\frac{\Delta f}{z_r} \approx \frac{\pi \theta^2 D^2}{8 f \lambda} \tag{5.5}$$

[1] Nominally covering the wavelength range 750–1100nm.
[2] Covering the wavelength range 550–1250 nm.

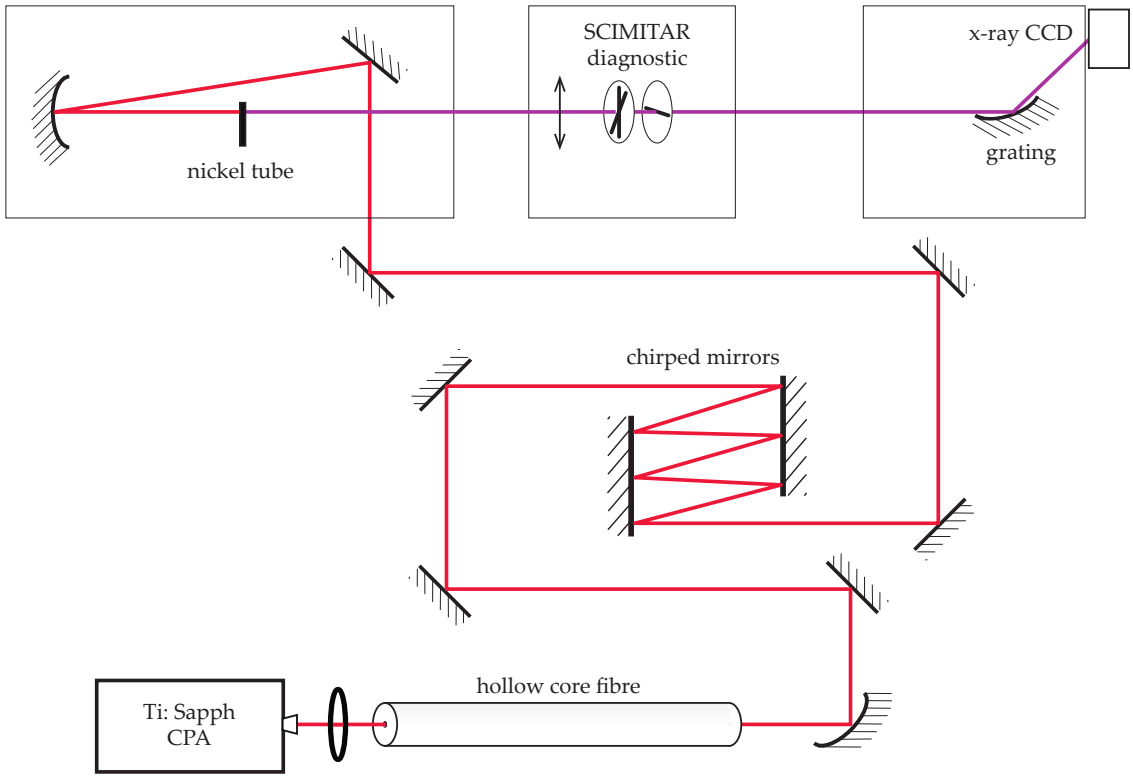

Figure 5.3: Diagram of the experimental arrangement after the installation of the hollow fibre compressor. Laser pulses from a chirped pulse amplifer are focused into the hollow fibre. The beam exiting the fibre is re-collimated before being sent through a set of chirped mirrors and then on to the experimental vacuum chambers. All mirrors are coated for low GVD in the spectral region around 800 nm.

where θ the angle of incidence on a focussing mirror of focal length f and D is the unfocussed beam diameter. For parameter values relevant to our experimental arrangement, equation 5.5 gives $\frac{\Delta f}{z_r} \approx 0.016$, indicating the astigmatism introduced by the new focussing geometry is insignificant.

The pulse duration was measured as a function of the pressure in the hollow core fibre. In the beam path between the pick-off and the GRENOUILLE entrance a thin glass plate was inserted, equal in thickness to the window of the vacuum chamber, balancing out the dispersion of the two paths. HCF backing pressures of 120, 200 and 450 mbar produced pulse durations (FWHM) of 32 fs, 22 fs and 14 fs respectively.[1] During these measurements the energy of the laser pulses exiting the HCF remained within 1% of 255 μJ.

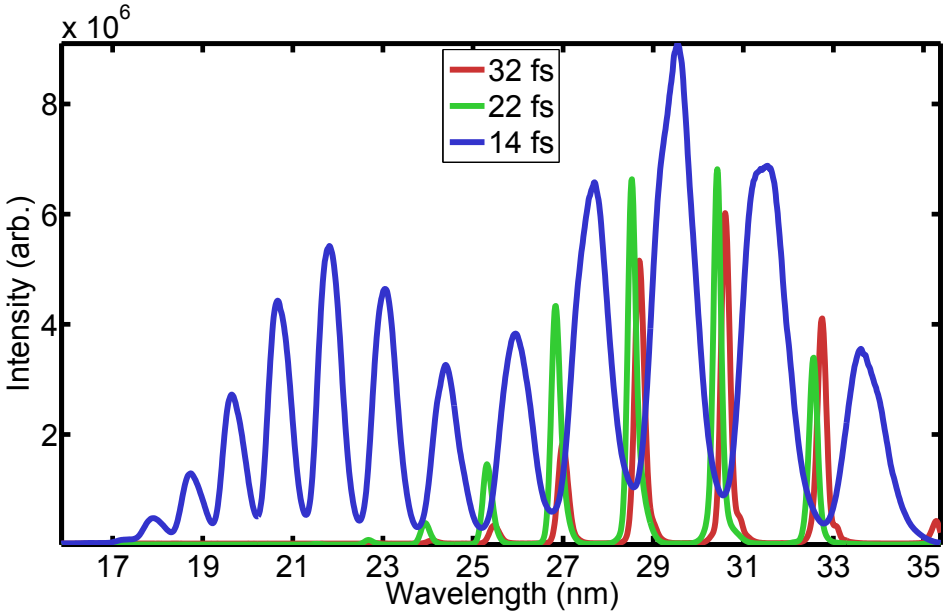

Figure 5.4: Measured high harmonic spectrum for driving laser pulses of various durations. The harmonic cut-off is observed to increase to shorter wavelengths (higher photon energies) as the pulse duration is decreased.

[1]The number of reflections from the chirped mirrors was fixed to eight.

High order harmonics were generated using driving pulses with the three durations described above. In these experiments the gas cell comprised a pressed nickel tubed, backed with 83 mbar of argon, placed close to the laser focus. HHG spectra for the three different pulse durations are shown in 5.4.

The highest photon energies were observed for the shortest pulses, with the cut-off for harmonics driven by 14 fs duration pulses extending up to the aluminium L-edge located at 17.1 nm. Looking closer at the location of the spectral peaks in figure 5.4, it is clear that each harmonic q lies to the blue (shorter wavelength) side of $\lambda_q = \frac{\lambda_0}{q}$, where λ_q is the harmonic wavelength. The spectral shifting of the harmonics is most likely in response to both a dynamic blue-shift to the harmonic brought about by the intensity dependent phase [38] in combination with a small blueshift of the fundamental after propagation through the gas-filled hollow fibre.

Pulses as short as 12 fs were recorded with the GRENOUILLE but with a larger 'FROG-error' (evaluated by the software). This may be due to either the pulse possessing a complex space-time structure that challenged the convergence of the FROG algorithm, or it could be be that for these conditions the bandwidth of the pulse was close to being too large for the GRENOUILLE. In addition, the shortest pulse durations were accompanied with degradation of the transverse spatial profile of the laser pulses. Nonetheless, with the very shortest driving pulses, harmonic orders well beyond the aluminium L-edge were observed (after replacing the aluminium filter with zirconium). A cut-off extension to wavelengths as short as 14 nm was recorded, albeit while using neon as the generating gas and at the expense of a smaller harmonic flux (compared to the when argon was used).

The spectrum generated by the 14 fs pulse presents some interesting attributes. At the low energy end, it encompasses a broad absorption feature in neutral argon (the generating gas) around 35 nm. At the high energy end it reaches the L-edge of aluminium. In the spectrum between the two absorption edges a clear 'dip' is observed around 24 nm. This has been identified as the 'Cooper-minimum' by Worner et al. [40] and has been the target of both experimental and theoretical studies [43, 47]. This feature was originally identified in the energy spectrum of photo-ionized electrons [10], where it was explained as resulting from interference of different ionization channels. The recombination step in HHG may be thought of as the time-reversed process of photo-ionization with the resultant minimum in the photon spectrum appearing at a roughly similar energy to its photoelectron counterpart.

The decrease in harmonic intensity for the final few orders is consistent with harmonics situated in the cut-off part of the HHG spectrum. As such, the harmonic spectrum obtained with 14 fs driving pulses is suitable for comparing the spatial properties of plateau and cut-off harmonic orders.

5.3 Spatial Properties of HHG Driven by Few-cycle Pulses

The high order harmonics produced in argon from 14 fs duration laser pulses were used to the study spectral dependence of the spatial properties of HHG. The radiation was characterized using the SCIMITAR technique described in chapter 4. Interference patterns at 35 unique pinhole separations were recorded

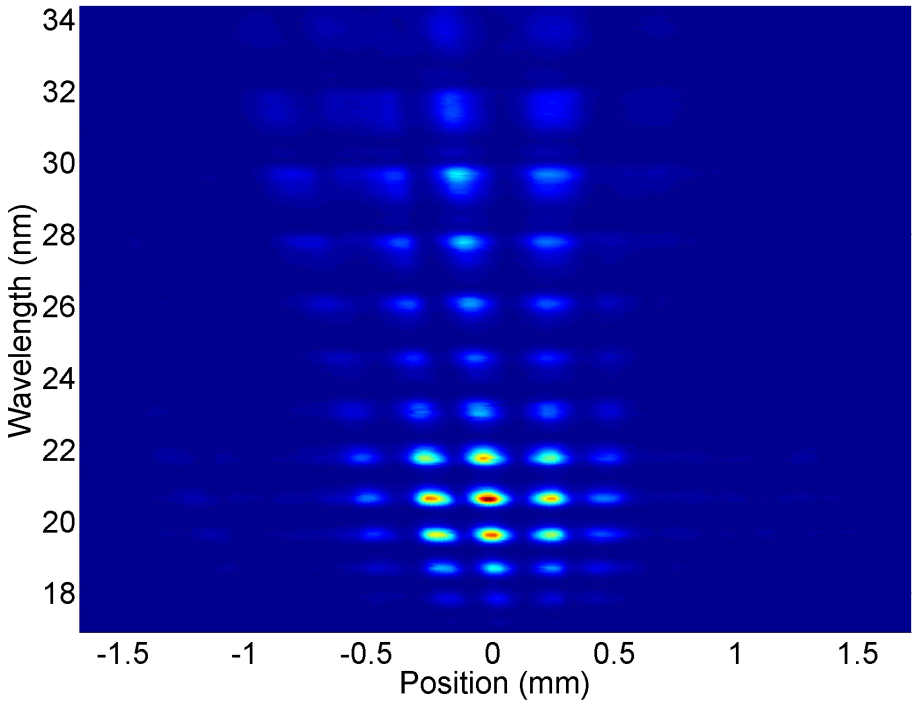

Figure 5.5: Example CCD acquisition (45 second exposure) taken during the course of the SCIMITAR scan for $s = -100\,\mu$m. Two-pinhole interference occurs in the horizontal direction, whereas the individual harmonic orders are resolved in the vertical direction.

using the same X-slit and horizontal slit as before. A nickel tube gas cell was pressed to an outer diameter of approximately 1.4 mm, backed with 83 mbar of argon and positioned close to the estimated focal plane. The harmonics were allowed to propagate approximately 0.72 m to the X-slit, and then, via a grating, to a CCD detector a further 1.22 m downstream of the harmonic source. The residual IR fundamental light was filtered with a 200 nm thick aluminium foil, prior to entry into the spectrometer. An example of a typical CCD acquisition is shown in figure 5.5.

5.3.1 Harmonic Intensity Profile

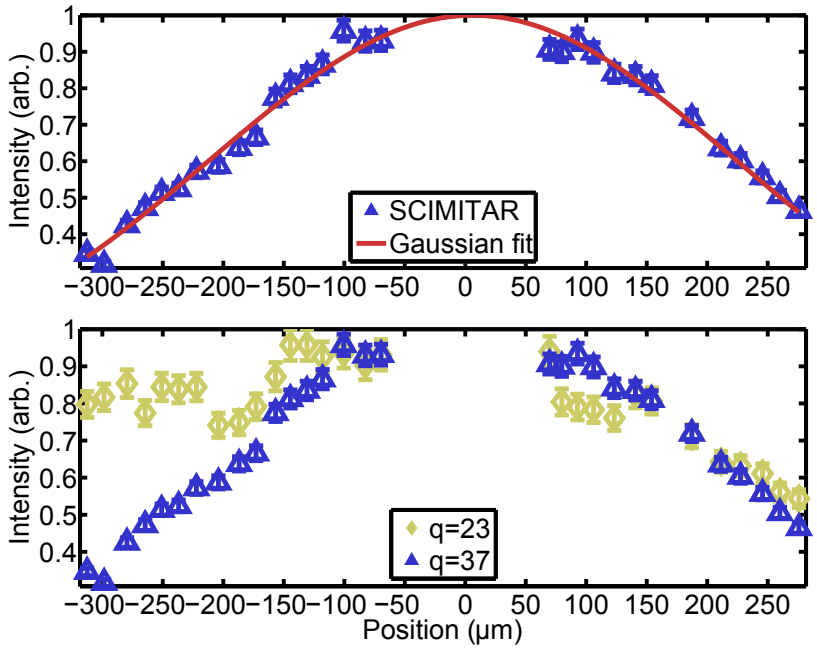

Figure 5.6: Upper plot: retrieved intensity profile of $q = 37$ (blue triangles) and Gaussian fit (red solid line), with a FWHM of 509 μm. Lower plot: comparison of the intensity profiles of $q = 23$ (gold diamonds) and $q = 37$ (blue triangles). The former presents a broader, less uniform shape compared to the latter.

Figure 5.6 shows the retrieved intensity profile for $q = 37$, together with a Gaussian fit to the data. This functional form was observed for all harmonic orders, with the exception of the two lowest ($q = 23$ and $q = 25$).

The lower plot of figure 5.6 shows a comparison between the retrieved intensity profiles of the 23^{rd} and 37^{th} harmonic orders. A clear difference is observed, with $q = 23$ being less uniform and broader. The marked difference between the broad, irregular $q = 23$ profile and the smooth, symmetric, Gaussian-like profile of the $q = 37$ is addressed later on.

5.3.2 Harmonic Wavefront

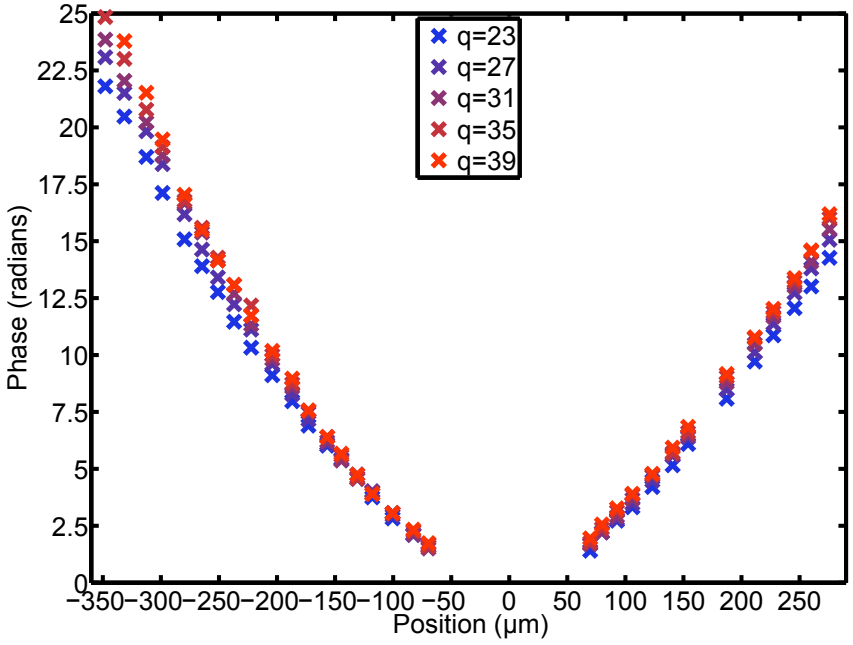

Figure 5.7: Retrieved transverse phase profiles of harmonic orders 23, 27, 31, 35 and 39. The wavefront is found to be parabolic with some spectral variation in the phase curvature. Errorbars are smaller than the symbol size for all data points.

The spatial phase profiles of the 11 harmonic orders observed were retrieved from the measured fringe patterns. Figure 5.7 shows a selection of data for five of the orders studied. The wavefronts were found to be parabolic, as before, with a small variation with harmonic order. The wavefront radius of curvature (R_p) was found to vary between 0.608 $\pm$0.033 ($q = 23$) and 0.724 $\pm$0.052 m ($q = 35$), compared to the X-slit – detector distance of 0.72 $\pm$0.05 m. The specific variation of R_p with order is addressed further on.

5.3.3 Harmonic Spatial Coherence

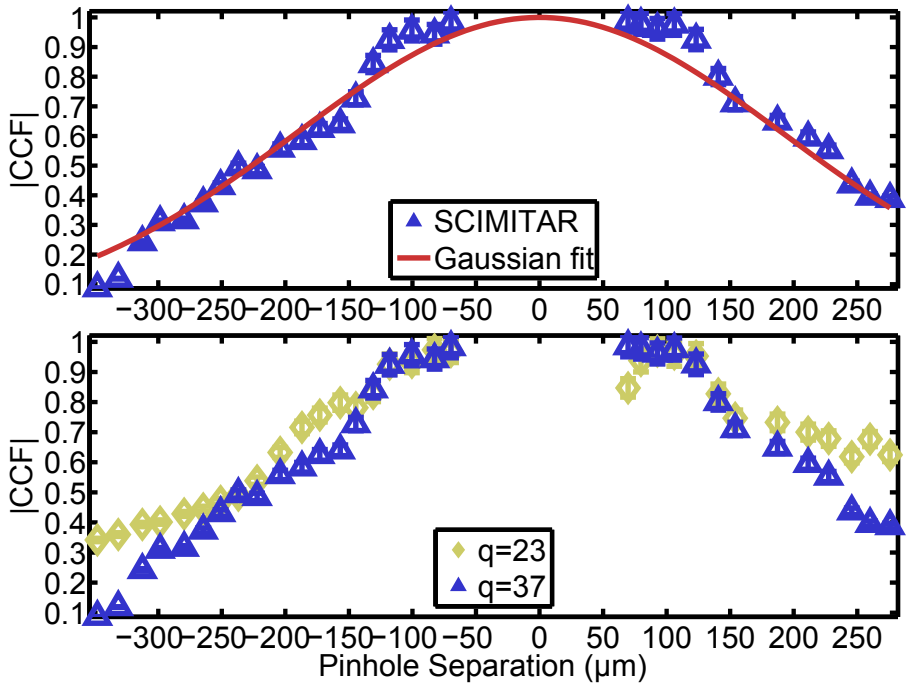

Figure 5.8: Upper plot: Recovered absolute value of the harmonic CCF for $q = 37$ (blue triangles) plotted as a function of pinhole separation along with a Gaussian fit (red solid line). Lower plot: recovered CCF magnitude for both $q = 23$ (gold diamonds) and $q = 37$ (blue triangles).

As was the case in section 4.4.3, the harmonic CCF was recovered by combining the fringe visibility with recovered beam intensity profile. The upper plot of figure 5.8 shows the CCF of $q = 37$, along with a Gaussian fit (FWHM=453 μm). Small deviations from a Gaussian profile are evident at $s = \pm 130$ μm, a feature which is addressed in more detail in chapter 6. The difference in the profiles of the CCF for low ($q \leq 25$) and higher-order ($q \geq 27$) harmonics is less pronounced than is the case for the transverse intensity profiles, as shown in the lower plot of figure 5.8.

5.4 Order Dependence of Harmonic Spatial Properties

The primary aim of the work described in this chapter is to quantify the spectral dependence of HHG spatial properties. Previous work has established that the width of the intensity profile [70], spatial phase curvature [34] and degree of spatial coherence [86] can vary (sometimes quite considerably) with harmonic order. Using SCIMITAR, we may measure the spectral dependence of all three quantities simultaneously in order to build a more complete picture of the origin of such coupling between the spectral and spatial domains.

5.4.1 Intensity Width

The variation of the width of the intensity profile was investigated as a function of harmonic order. To find the width of a given intensity profile, the data was interpolated, and the first points either side of the beam centre where the intensity

dropped below 76% were found.[1] Of course, it would be more usual to find the width of the profile at the 50% level, as in the full width at half maximum. However, in some cases, $q = 23$ particularly, the intensity did not fall to below 50 % over the transverse distance measured by the SCIMITAR scan. The 76 % level was chosen as the same procedure could be applied to all orders and for the recovered harmonic CCF as well. Assuming a Gaussian form, the full width at 76% can be converted to FWHM through multiplying by the factor $\sqrt{\frac{\log(2)}{\log(100/76)}}$.

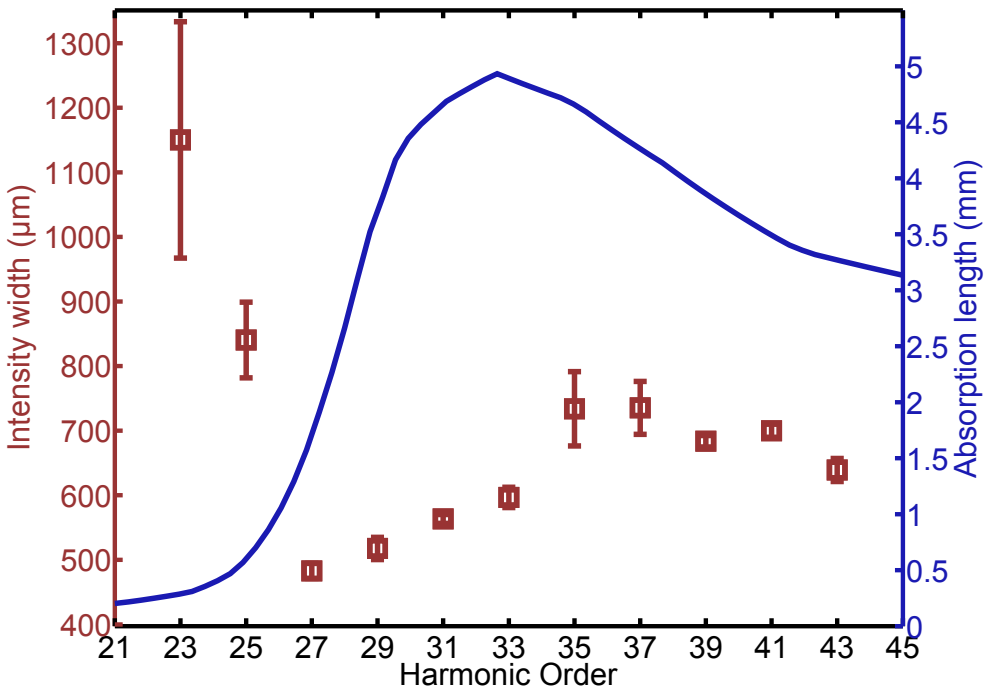

Figure 5.9: Width (FWHM) of the harmonic intensity profile as a function of order (brown squares). The solid blue line is the absorption length in argon (for a pressure of 83 mbar)

The intensity width (W_{pI}), full width at half maximum, is plotted as a function of harmonic order in figure 5.9 with brown squares. Interestingly, W_{pI} appears

[1] Equivalently, the full width at 76% maximum.

to be composed of two distinct regions. Orders 23 and 25 have a much larger intensity width than higher orders. The solid blue line in figure 5.9 shows the absorption length of argon as a function of q. It can be seen that for $q = 23$–25 the absorption length is much shorter than the length of the gas cell, which was approximately 1.4 mm. For $q \geq 27$ there is a broad trend of increasing W_{pI} with q, rolling off at the highest orders. The rolling over of W_{pI} approximately coincides with similar effect in the absorption length, hinting to a link between the two phenomena. We will return to this point further on.

Absorption of the harmonic field has been identified as one of the principle limitations on the conversion efficiency of HHG [32, 63]. In the work of Constant et al. [32] the authors found that the conversion efficiency saturates when the medium length is approximately five absorption lengths (L_{abs}) long, even in the case of perfect phase-matching. Absorption has also been identified as the cause of dramatic spectral shaping of particular harmonic orders coinciding with so called 'Fano resonances' [49]. The relationship between the spatial profile of the harmonic beam and absorption however is not well documented.

Knife-edge measurements of a focussed HHG beam have found it be of good spatial quality, only two times diffraction limited ($M^2 = 2$) [106]. Studies of HHG in capillary waveguides have shown that production of a smooth harmonic transverse intensity profile can coincide with a peak in the harmonic flux due to phase-matching [21], with an irregular profile present under non-optimised generating conditions. Further discussion on the role of phase-matching in shaping the transverse emission is found in section 5.5.

5.4.2 Wavefront Curvature

The wavefront radius of curvature (R_p) was extracted by fitting a polynomial of the form $\phi = A + Bx + Cx^2$ to the spatial phase profiles recovered for each harmonic order. The wavefront curvature (R_p) was evaluated by equating the fit parameter C with $\frac{k}{2R_p}$. A plot of $R_p - z_{\mathrm{gp}}$ (where z_{gp} is the separation between the gas cell and X-slit) as a function of q is shown in figure 5.10.

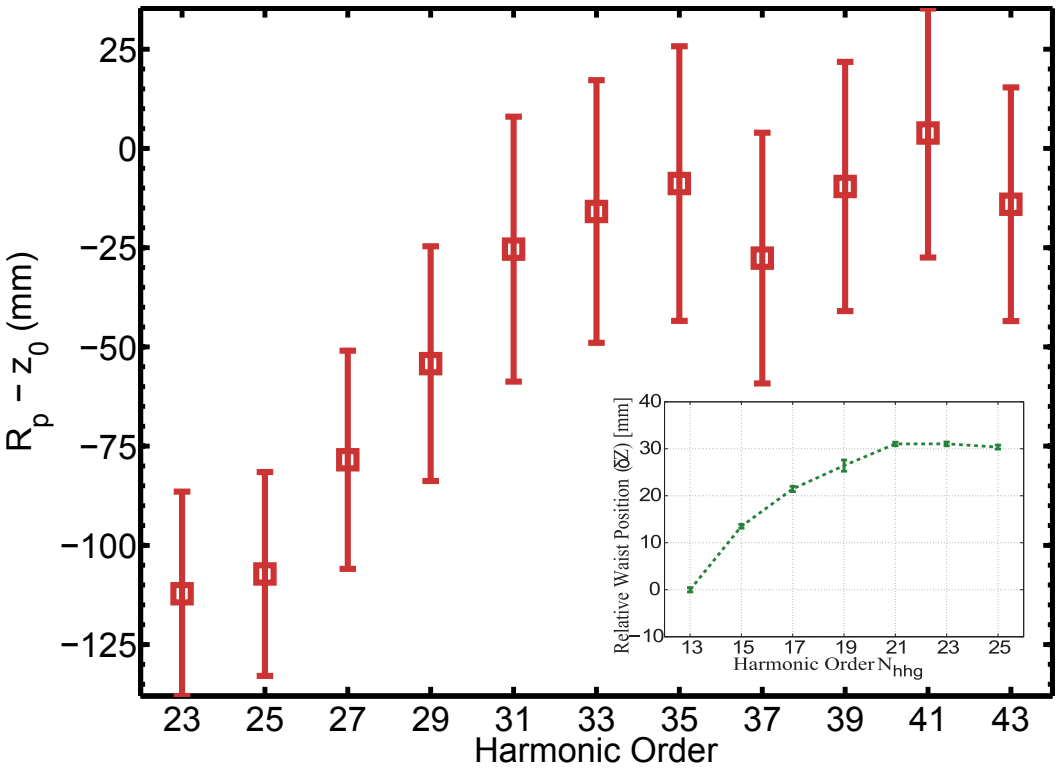

Figure 5.10: The red squares show $R_p - z_{\mathrm{gp}}$ as a function of q, where $z_{\mathrm{gp}} = 0.72$ m is the longitudinal separation between gas cell and X-slit (or equally between the 'generation' and 'propagated' planes). The wavefront curvature was determined by a fit to the experimentally measured spatial phase. The errorbars are 95% confidence intervals of the respective fits. The inset shows a plot taken from the study of Frumker et al. [34]. As with the main figure, $R_p - z_{\mathrm{gp}}$ is plotted as a function of q, measured in this case using the SWORD technique.

For the lower order harmonics, R_p is seen to increase with q. This increase rolls off at the highest harmonic orders. In the inset of figure 5.10, a plot taken from the study of Frumker et al. [34] is shown. They plotted $R_p - z_{\mathrm{gp}}$ as a function of harmonic order retrieved using the SWORD technique, for high harmonics generated in a nitrogen[1] backed gas jet. Despite Frumker et al. using longer duration laser pulses (and thus focussing their study on lower order harmonics) a qualitatively similar spectral variation of R_p was reported.

5.4.3 Coherence Width

In figure 5.8 the magnitude of the CCF for $q = 37$ was plotted as a function of pinhole separation. The width of $|\mu|$ can be used as a measure of the spatial coherence of the radiation. The coherence width (W_{pC}) is defined here as the full width where $|\mu|$ first falls below 0.5. The coherence width is determined using interpolation in exactly the same fashion as was used for the intensity width.

Figure 5.11 shows W_{pC} plotted as a function of q. As for W_{pI}, $q = 23$–25 have aberrant values for W_{pC} compared to the trend for higher harmonic orders. The variation of the coherence width with order for $q = 27$–43 closely follows a q^{-1} relationship, as evidenced by the fit (to orders 27–43 only) shown by the solid blue line. The spectral variation of the CCF width for radiation from a (polychromatic) incoherent, disc-shaped source also scales with q^{-1} (see section 3.2.1). Through equation 3.40, the equivalent incoherent source diameter is found to be 48 microns. However, care is required before drawing any firm conclusions about the nature of the harmonic source. The coherence properties merely match

[1] The ionization potential of molecular nitrogen is 15.581 eV, similar to the ionization potential of atomic argon (15.754 eV).

those of radiation produced by an incoherent source of a particular size. The fact

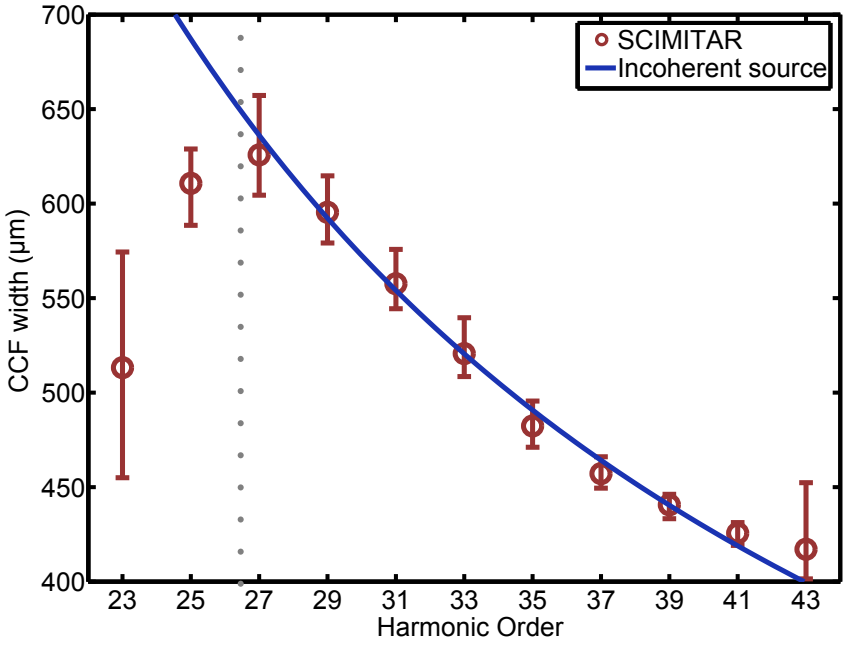

Figure 5.11: The brown circles show the coherence width (full width at half maximum) plotted as a function of harmonic order. The solid blue line is the CCF width variation expected for an incoherent (disc-shaped) source of size 48 microns. The grey dotted line shows the boundary between wavelengths for which the absorption coefficient is smaller (right) or larger (left) than $> 50\%$ absorption per mm.

that we observe low divergence beam[1] (as evidenced by figure 5.9) shows that the harmonic source must be at least partially coherent [123] and that the van Cittert-Zernike theorem is not a physically accurate model for inferring the source properties. Nonetheless, the fact that W_{pC} closely follows a $\frac{1}{q}$ variation with harmonic order allows the prediction of the coherence width for other harmonic orders not observed here, in the limit of a negligible effect by absorption.

[1]The divergence is calculated to be of the order of 1 mrad (at the FWHM level).

5.4.4 Coherent Fraction

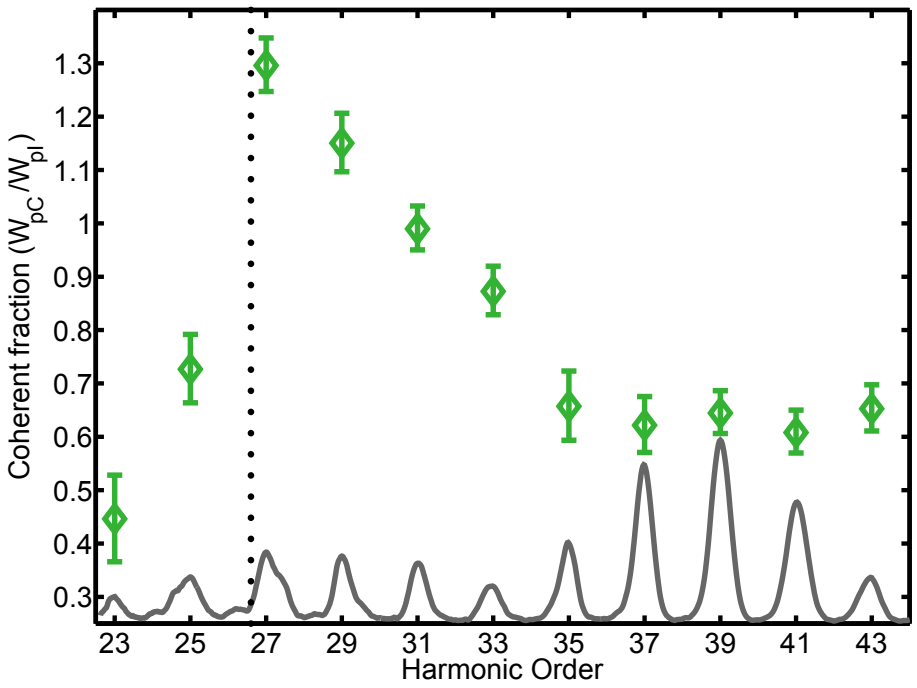

Figure 5.12: The coherent fraction ($q_{\mathrm{IC}} = \frac{W_{\mathrm{pC}}}{W_{\mathrm{pI}}}$) as a function of harmonic order (green diamonds). The black dotted line shows the 50% absorption threshold in argon (the same as the grey dotted line in figure 5.11). The HHG spectrum is shown by the solid grey line.

In section in section 3.2.3, the coherent fraction ($q_{\mathrm{IC}} = \frac{W_{\mathrm{pC}}}{W_{\mathrm{pI}}}$) was identified as a more suitable metric of the spatial coherence of radiation than the coherence width alone. Figure 5.12 shows q_{IC} plotted as a function of q with green diamonds.

We find that q_{IC} varies quite considerably for the harmonic orders observed attaining its maximum value for $q = 27$. The highest five orders ($q = 35$–43) show little variation in q_{IC}. In line with the results of presented in figures 5.9 and 5.11, strongly absorbed harmonics have a low coherent fraction, since they are broader in intensity and narrower in CCF than those which are not absorbed significantly.

If for a particular application the radiation is required to be spatially coherent, it may be useful to know that the lowest order harmonic, not affected by absorption, has the highest coherent fraction.

5.5 Coherence Length

The coherence length (L_c) is an important parameter in nonlinear optics. For an extended gas medium, with length denoted by L_{cell}, the coherence length dictates the maximum longitudinal distance over which harmonics can be generated when $L_{cell} > L_c$. In section 2.3.1 three sources of wavevector mismatch (Δk) were identified: neutral dispersion, plasma dispersion and Gouy phase contributions. Here each component of Δk is evaluated to calculate L_c for $q = 23$–43.

A key parameter for calculating the neutral and plasma dispersion contributions is the ionization fraction (η). Calculations using the ADK formalism [3] provide η as a function of time for the interaction of an intense laser pulse with an atom. Here we assume that a given harmonic q is generated at the instant (t_q) that the laser intensity reaches a sufficiently large enough value, as dictated by the cut-off law (equation 2.6). The value of η for harmonic q is then given by $\eta(t_q)$. For the neutral gas dispersion the difference in the refractive index encountered by fundamental and harmonic is needed. Here the Sellmeir coefficients are used for evaluating the infrared refractive index in neutral argon (n=1.00027962) while the XUV refractive index is approximated to be equal to unity. For the Gouy phase contribution we have assumed that the entrance of the gas cell lies on the laser focal plane, with the exit a further 1.4 mm downstream.

In figure 5.13 the calculated coherence length is plotted. It is found to decrease

with increasing order, similar to calculations performed for HHG from waveguides [111]. The absorption length is also shown in figure 5.13, with purple squares. Our calculations show that for only two orders (23 and 25) is the coherence length longer than the absorption length. In this case, the length over which the harmonic signal builds up is limited by absorption and not dispersion. The converse is true for orders 27+ where the absorption length is longer than both the coherence length and the medium length. For those orders the measured harmonic field is limited to that originating from a length L_c at the end of the medium.

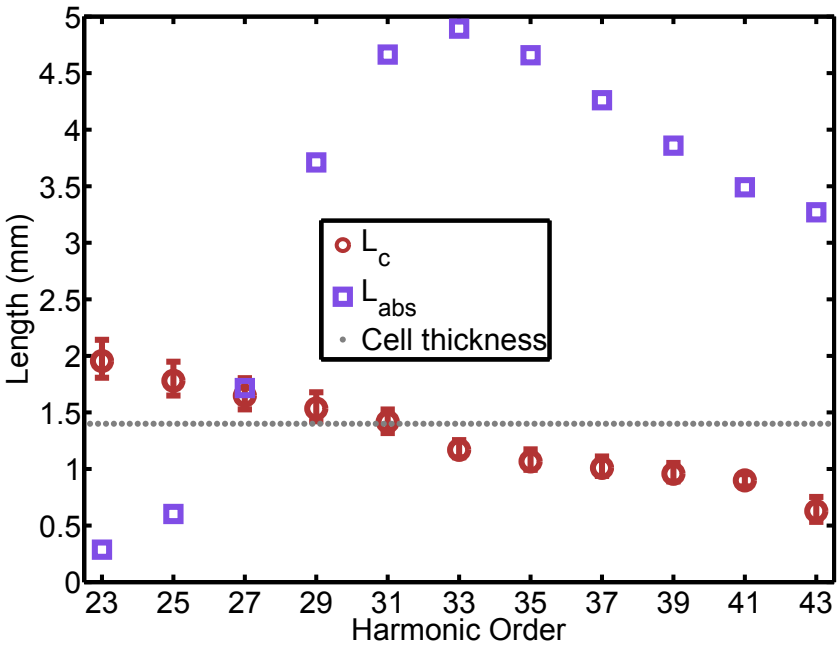

Figure 5.13: Calculated coherence length (brown circles) and absorption length (purple squares) plotted for the range of orders considered. Both quantities are shown for parameters relevant to the experimental conditions. The grey dotted denotes the thickness of the gas cell. The errorbars for L_c were evaluated by varying the peak laser intensity in the calculation for the coherence length within the experimental uncertainty for the pulse energy, duration and spot size.

As a further point, the length of gas cell was set by placing thin ($\approx 400\,\mu$m thick) 'spacers' inside a nickel tube and pressing the tube such that the inner diameter of the cell was the same size as the thickness of the spacers. The spacers were removed before the gas cell was installed. After multiple different lengths were tested, $L_{\text{cell}} = 1.4$ mm was chosen as it provided the brightest harmonic signal while keeping the cell backing pressure to a reasonable level. Our calculation shows that $L_c \approx L_{\text{cell}}$, agreeing with our observation of the bright harmonics for this choice of cell length.

When absorption is large, i.e $L_{\text{abs}} \ll L_{\text{c}}$ and $L_{\text{cell}} > L_{\text{abs}}$, contributions to the harmonic field from atoms at locations everywhere but at the very end of the medium are absorbed and not measured. In this case propagation effects within the cell may be 'cancelled out' by absorption. Indeed, studies of HHG from semi-infinite gas cells by Peatross et al. [112] have shown experimentally that absorption can localise the harmonic emission to the very final part of an extended gas medium. The results presented here suggest that for HHG in argon and when $q < 27$, absorption may act to disrupt the smooth 'build-up' of the harmonic signal associated with phase-matching, leading to the aberrant spatial properties observed for low order harmonics. Detailed 3-D simulations of HHG, including the effects of propagation, could shed more light on this effect.

5.6 Inferring Source Spatial Properties

So far, the presented results have shown the spatial properties of high harmonics measured at a plane 0.72 m downstream from the gas cell (radiation source). The SCIMITAR measurement provides ample information to back-propagate the

harmonic field to the source location. In doing so it is possible to probe the conditions under which the harmonics are generated.

5.6.1 Gaussian Beam

A Gaussian beam may be parameterised by three quantities: the 'apparent' waist size (w_a), the waist longitudinal position[1] (z_ag) and the wavelength (λ_q).[2] All

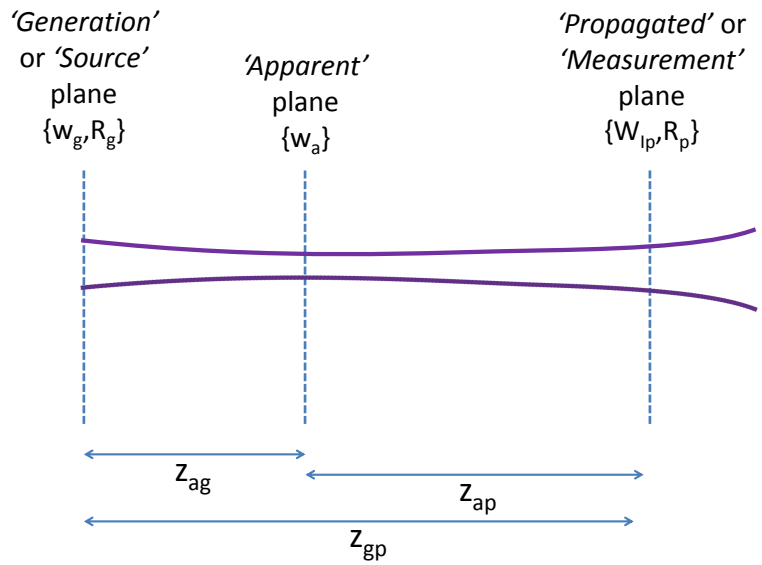

Figure 5.14: Diagram depicting the relative location of the three transverse planes identified in this chapter.

relevant quantities are depicted in figure 5.14. Equations 3.12 and 3.15, which give expressions for the downstream beam width (W_pI) and wavefront curvature

[1]The waist positions are defined relative to some fixed downstream plane, in our case the plane the SCIMITAR scan is made in.

[2]The subscript 'a' refers to the *apparent* radiation origin: for a field measured far from the generating plane, 'a' denotes the plane where the radiation wavefront would be planar.

(R_q) respectively, may be inverted to yield:

$$w_{\mathrm{a}} = \frac{W_{\mathrm{pI}} R_p \lambda_q}{\sqrt{\pi^2 W_{\mathrm{pI}}^4 + R_p^2 \lambda_q^2}} \tag{5.6}$$

$$z_{\mathrm{ap}} = \frac{\pi^2 R_p W_{\mathrm{pI}}^4}{\pi^2 W_{\mathrm{pI}}^4 + R_p^2 \lambda_q^2}. \tag{5.7}$$

In our case we find that $z_{\mathrm{ap}} < z_{\mathrm{gp}}$ for all harmonic orders observed. Propagating backwards to the plane where the harmonic are generated (within the gas cell) gives:

$$R_{\mathrm{g}} = (z_{\mathrm{ap}} - z_{\mathrm{gp}}) \left[1 + \frac{\pi^2 w_{\mathrm{a}}^4}{\lambda_q^2 (z_{\mathrm{ap}} - z_{\mathrm{gp}})^2} \right] \tag{5.8}$$

$$w_{\mathrm{g}} = w_{\mathrm{a}} \sqrt{1 + \frac{\lambda_q^2 (z_{\mathrm{ap}} - z_{\mathrm{gp}})^2}{\pi^2 w_{\mathrm{a}}^4}} \tag{5.9}$$

where R_{g} and w_{g} are the source radius of curvature and beam size in the generation plane.

Treating the harmonic radiation as a Gaussian beam, we may calculate the source intensity size and wavefront curvature using the measured values of W_{pI} and R_q with equations 5.8 and 5.9. The results are shown in figure 5.15. The source intensity width is seen to decrease with harmonic order, with the exception of $q = 23$ and 25. The source wavefront curvature on the other hand, mirrors the trend followed by R_q in figure 5.10, with orders 31–43 showing broadly the same values.

As described in section 2.4, an analytic model the harmonic source phase R_{g} predicted only weak dependence on harmonic order. Austin et al. [28] measured a frequency dependence of the harmonic source curvature using shearing inter-

ferometry, attributing the variation with order as originating from the intensity-dependent phase of the induced harmonic dipole. We may further investigate this phenomenon by use of our model of the harmonic wavefront introduced in section 2.4. To recap, the source wavefront curvature R_{g} at position z in the source (where $z = 0$ denotes the laser focal plane) is given by:

$$R_{\mathrm{g}} = \pi \left\{ \frac{2\alpha\beta}{w_p(z)^2} \left[\frac{hc}{\kappa\lambda_0^2} - \frac{I_{\mathrm{p}}}{q\kappa\lambda_0} \right] + \frac{\lambda_0^2 z}{\pi w_0^2 w_p(z)^2} \right\}^{-1}. \tag{5.10}$$

Referring to figure 5.15, R_{g} was measured to be approximately constant for

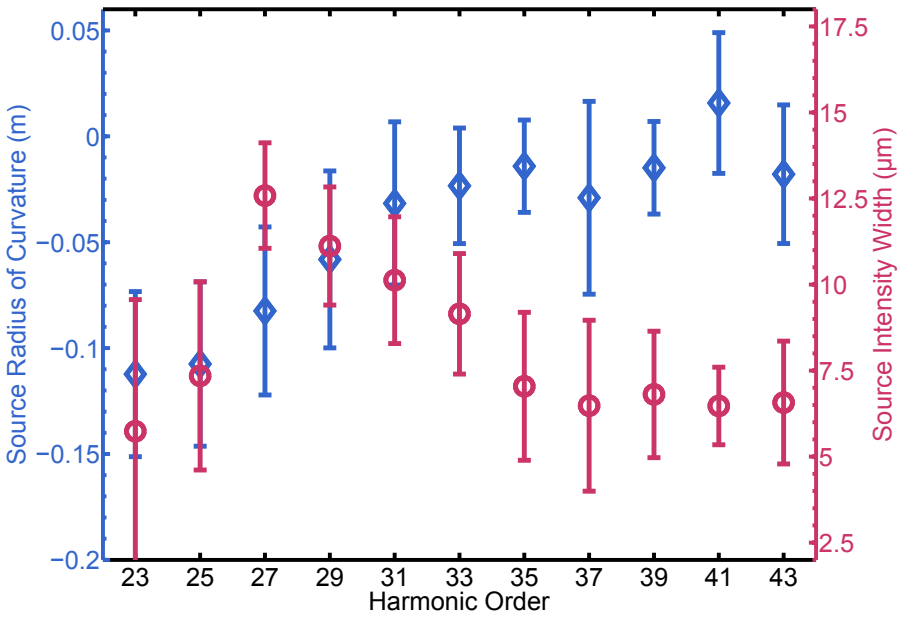

Figure 5.15: The variation of the FWHM source intensity width (pink circles) and source wavefront curvature (blue diamonds) with harmonic order. Both quantities were calculated from the measured values of W_{pI} and R_p using equations 5.8 and 5.9.

the cut-off harmonic orders ($q = 31$ to $q = 43$), having a value of $R_{\mathrm{g}} \approx -25$ mm. In the upper plot of figure 5.16, equation 5.16 is evaluated for parameters

relevant to our experimental conditions: $q = 33$, $\alpha = 1 \times 10^{14}$ cm^{2}W^{-1} and a laser spot size $w_0 = 48\ \mu$m (as measured in situ).[1] The (harmonic) wavefront curvature from either the intensity dependence phase alone (solid orange line) or just the fundamental phase (green dotted line) are also plotted. For the upper plot $\beta = 0.5$, yielding a curvature of approximately -25 mm close to the laser focal plane ($z = -0.9$).

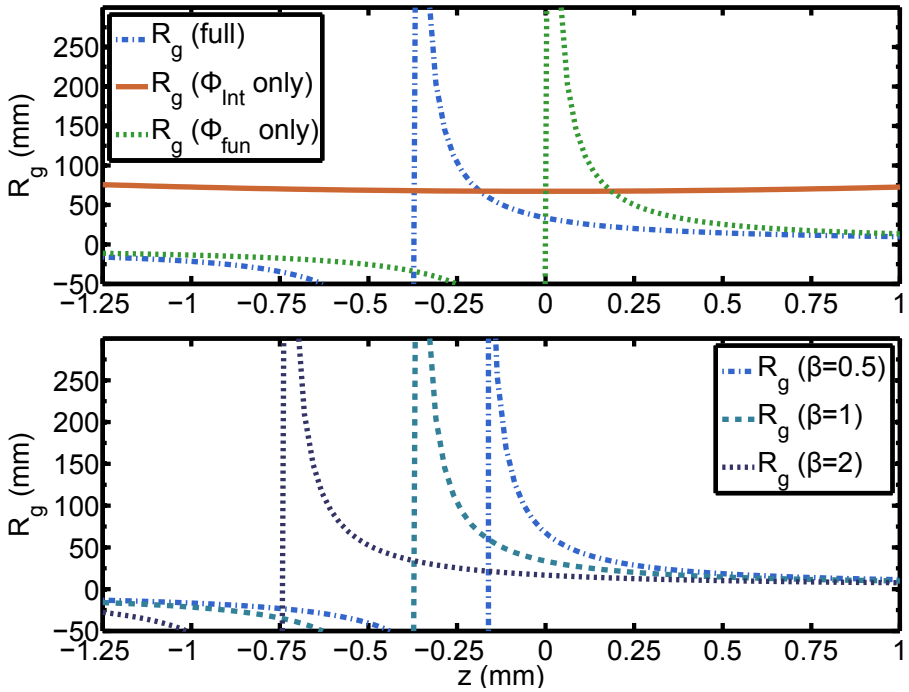

Figure 5.16: Upper plot: source wavefront curvature, as a function of position about the focal the plane, calculated for $q = 33$, $w_0 = 48\mu$m, $\alpha = 1\times10^{14}$cm^{2}W^{-1} and $\beta = 0.5$ using equation 5.10. The full expression is shown by the blue dot-dashed line, whereas the green dotted line shows the curvature from ($q\times$) the fundamental only. The orange solid line shows the curvature from the intensity dependent phase alone. Lower plot: R_g (full expression) plotted for the same values as above but for three different values of β.

The lower plot of figure 5.15 shows R_g plotted for three different values of β.

[1] The alpha parameter was taken from the theoretical work of Gaarde et al. [57].

The position z where R_g is equal to $-25\,\mathrm{mm}$ moves further *upstream* (left in the figure) of the target as β is increased. In our experiments the target was placed *downstream* of the focal plane. Thus, in order for equation 5.16 to better agree with the values of R_g inferred from the SCIMITAR measurement a β value less than one is needed. Since β is the multiple of the minimum laser intensity to generate a harmonic q, it seems unreasonable for it to be smaller than one. This discrepancy indicates the model of the wavefront curvature is not quantitatively accurate.

There are multiple possible reasons why the model fails to account for the measured source curvature accurately. The method for evaluating the intensity at which the harmonic is generated, including the estimation of the β parameter is somewhat simplistic. A more rigorous calculation of I_q may yield closer agreement between theory and experiment. Here we have considered the harmonic wavefront curvature at a single plane defined by z. However the emission originates over a range of z, and so, in more sophisticated model, this should be accounted for. Furthermore, modelling the harmonic beam using Gaussian optics implicitly assumes the radiation is spatially coherent, but our measurements show definitively that it is not so. This will affect the propagation of the harmonic field. Furthermore, the value of w_0 used above was recorded at atmospheric pressure through measuring the fundamental beam caustic. It may be that the real spot size at the focal plane is enlarged by plasma induced defocussing. This may in turn, at the very least, allow β to take a more physically realistic value (i.e. $\beta > 1$).

5.6.2 Gaussian-Schell Model

The Gaussian-Schell model (see section 3.2.3) is a promising method for back-propagating the measured harmonic spatial properties. It is useful to recount some of the aspects of the model to assess its suitability for application to HHG:

1. The CCF and intensity profile of the beam are both Gaussian functions.
2. The CCF is assumed to depend on only on the separation of the two test points.
3. The radiation is assumed to originate from a source with a flat spatial phase profile.

Evidence thus far suggests that each of the three aspects identified above could be called into question for HHG. In particular, the results of section 5.4.2 imply that the harmonics are generated with an initial (order dependent) curvature, violating the planar source requirement. In spite of such differences, the Gaussian-Schell model (GSM) should at least provide a decent approximation of the harmonic source properties, keeping in mind that the above points mean that it forms an incomplete model of the source and the propagation of the radiation it generates. Here, specifically, the GSM is used to investigate the order dependence of the source intensity and coherence widths.

Inverting equations 3.63 and 3.67 and solving for the widths of the source intensity profile ($w_{0\mathrm{I}}$) and source CCF ($w_{0\mathrm{I}}$) yields the following expressions:

$$w_{0\mathrm{I}} = \frac{1}{\sqrt{2}}\sqrt{W_{\mathrm{pC}}^2 - \frac{\sqrt{k^2 W_{\mathrm{pC}}^2\left(-z^2 W_{\mathrm{pC}}^2 - 4z^2 W_{\mathrm{pI}}^2 + k^2 W_{\mathrm{pC}}^2 W_{\mathrm{pI}}^4\right)}}{W_{\mathrm{pI}}^2 k^2}} \tag{5.11}$$

$$w_{0\mathrm{C}} = \frac{1}{\sqrt{2}}\sqrt{W_{\mathrm{pI}}^2 - \frac{\sqrt{k^2 W_{\mathrm{pC}}^2\left(-z^2 W_{\mathrm{pC}}^2 - 4z^2 W_{\mathrm{pI}}^2 + k^2 W_{\mathrm{pC}}^2 W_{\mathrm{pI}}^4\right)}}{W_{\mathrm{pC}}^2 k^2}}. \tag{5.12}$$

The measured (far-field) intensity and coherence widths are inserted into equations 5.11 and 5.12 to calculate the corresponding source quantities.

5.6.3 Harmonic Source Intensity Width

The source intensity width ($w_{0\mathrm{C}}$) was calculated for each harmonic order using the measured propagated intensity and CCF widths (W_{pI} and W_{pC}, respectively) and equations 3.63 and 3.67. In figure 5.17, $w_{0\mathrm{I}}$ is plotted as a function of harmonic order. The harmonic source size is found to decrease with increasing harmonic order. This agrees well with the expectation that higher orders are associated with higher laser intensities, effectively localising the emission closer to the optical axis.

By defining the relationship between the fundamental and harmonic intensities it is possible to derive an expression for the harmonic source size. Naively one might expect HHG to be a perturbative process, similar to lower order nonlinear optical effects like second harmonic generation. In this case the relationship between fundamental intensity (I_0), the harmonic intensity [$I(q\omega)$] takes the following form:

$$I(q\omega) = I_0^q. \tag{5.13}$$

Assuming the fundamental has a Gaussian transverse profile, the FWHM of the

(theoretical) harmonic source intensity width ($w_{0\mathrm{IP}}$) is given by:

$$w_{0\mathrm{I}}(q) = \frac{w_0}{\sqrt{q}} \tag{5.14}$$

where w_0 is the FWHM of the fundamental. Although fitting equation 5.14 to the inferred harmonic source size shows reasonable agreement (see the solid red line in figure 5.17), the fit however yields $w_0 = 189 \pm 4\,\mu$m. Measurement of the fundamental spot size in situ, albeit not under vacuum, found $w_0 = 48 \pm 2\mu$m, in marked disagreement with the fit of equation 5.14. This discrepancy most likely originates from the fact that HHG should not be treated as a perturbative process. Theoretical work has shown that the harmonic source intensity can be

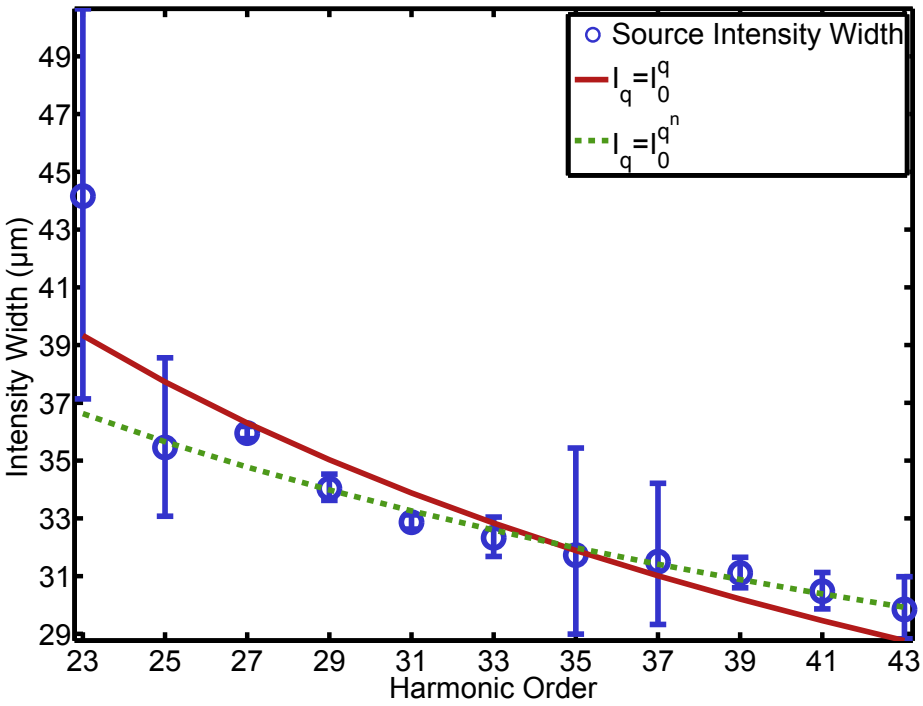

Figure 5.17: Harmonic source diameter (FWHM) deduced using the Gaussian-Schell model (blue circles). The solid red line is a fit according to equation 5.14. The green dotted line is a fit according to equation 5.16.

treated (to a good approximation) instead as $I(q\omega) = I_0^6$ [107]. This would yield a harmonic source size that is independent of order, varying as $\frac{w_0}{6}$. Figure 5.17 however shows clearly that the harmonic source size is a function a q.

We find better agreement to our inferred source size by adopting a modified version of the perturbative form described above. Specifically, if we assume the harmonic intensity can be described by:

$$I(q\omega) = I_0^{\{q^n\}} \tag{5.15}$$

then the source size takes the following form:

$$w_{0\mathrm{IN}} = w_0 q^{-\frac{n}{2}}. \tag{5.16}$$

A fit of equation 5.16 to the inferred source size is shown in figure 5.17. A closer agreement is observed than is the case for the perturbative model. The fit yields a fundamental spot size $w_0 = 100.9 \pm 29.0\mu$m, again larger than that measured independently, but closer than the same parameter derived from the perturbative model fit. The modified perturbative fit found $n = 0.646 \pm 0.162$ best fitted the deduced values of $w_{0\mathrm{I}}$.

5.6.4 Harmonic Source Coherence Width

The harmonic source coherence width (w_{C_p}) was also calculated using the Gaussian-Schell model. The source coherence width is plotted as a function of q in figure 5.18. The trend is qualitatively similar to that presented in figure 5.12. The reason for this is that under the Gaussian-Schell model coherent fraction is invariant

under propagation:

$$q_{\mathrm{IC}} = \frac{w_{\mathrm{pI}}}{w_{\mathrm{pI}}} = \frac{w_{0\mathrm{C}}}{w_{0\mathrm{C}}}. \tag{5.17}$$

The fact that $w_{0\mathrm{I}}$ does not vary considerably with q (see figure 5.17), means it can be treated as very approximately constant. Consequently, equation 5.17 shows that $w_{0\mathrm{C}}$ can be treated as approximately proportional to q_{IC} and will thus show a similar variation with q.

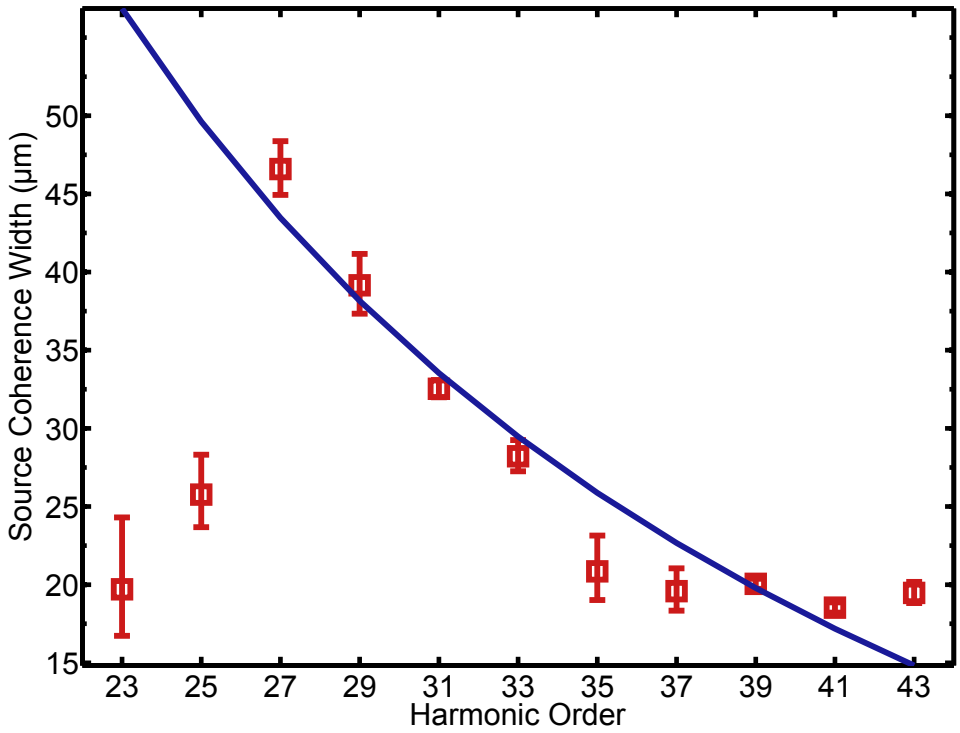

Figure 5.18: Harmonic source coherence width ($w_{0\mathrm{C}}$) calculated using the Gaussian-Schell model (red squares). The solid blue is a fit according to equation 5.21.

Orders $q = 23$ and 25 display a low coherence length compared with the neighbouring harmonics ($q = 27$ and $q = 29$). Figure 5.18 indicates that, in the

frame of Gaussian-Schell model, the aberrant spatial properties of $q = 23$–25, measured downstream of the gas cell with SCIMTIAR, seem to be caused by a relatively depressed harmonic source spatial coherence.

As discussed in section 5.4.1, the spatial quality of a HHG beam can be affected by how well the generation process is phase-matched [21]. In a similar way that the intensity profile may be affected by the longitudinal localisation of the harmonic emission through absorption, the rapid transverse variation in the phase of the dipole may also influence the spatial coherence of the emission. However, more detailed modelling, matched to the experimental conditions found in our experiments, would be required to confirm this.

In section 3.5 a model was developed to quantify the degree of spatial coherence of a high harmonic radiation source. The main result was an expression for the harmonic source CCF:

$$|\mu_q| = 1 - q^2(1 - |\mu_0|) - \frac{1}{2}\alpha^2 \Delta I_{\mathrm{x}}^2 V(\epsilon_t^2). \tag{5.18}$$

To reiterate, the harmonic CCF is degraded by an inherited partial coherence from the fundamental beam as well as from a contribution from the intrinsic dipole phase. In order compare the deduced values of the source coherence width with the predictions of the model, an expression for the FWHM of $|\mu_q|$ as a function of q must be derived from equation 5.18. However, the equation is not tractable and a general form for the source coherence width cannot be obtained. By making some tacit assumptions we may derive an approximate expression. Firstly, we assume that the CCF of the fundamental is a Gaussian function of

point separation (Δx):

$$|\mu_0| = \exp\left(\frac{-\Delta x^2}{\sigma^2}\right). \tag{5.19}$$

Inspection of equation 5.18 reveals that the order dependence of the source coherence width originates from the term related to the fundamental CCF. In the limit where the dipole phase can be neglected the source coherence width (FWHM) can be shown to take the following form:

$$w_{0\mathrm{Cf}} = 2\sigma\sqrt{\log\left(\frac{1}{1-\frac{1}{2}q^{-2}}\right)} \tag{5.20}$$

The dipole phase contribution ($w_{0\mathrm{Cd}}$) alone can be found numerically once a suitable beam size, intensity and α value are used. Here however we assume that since the dipole term is independent of harmonic order it simply acts to reduce the overal source coherence width ($w_{0\mathrm{C}}$) by an (order independent) amount K (with $K \leq w_{0\mathrm{Cf}}$). Thus $w_{0\mathrm{C}}$ can be expressed as:

$$w_{0\mathrm{C}} \approx w_{0\mathrm{Cf}} - K$$
$$w_{0\mathrm{C}} \approx 2\sigma\sqrt{\log\left(\frac{1}{1-\frac{1}{2}q^{-2}}\right)} - K. \tag{5.21}$$

A fit of equation 5.21 to the deduced values of $w_{0\mathrm{C}}$ is shown in figure 3.67 (with σ and K as fit parameters).[1] The fit yielded values of $\sigma = 1.46 \pm 0.40\,\mathrm{mm}$ and $K = 33 \pm 16\,\mu\mathrm{m}$. The large value of σ, relative to the fundamental spot size ($\approx 50\,\mu\mathrm{m}$), indicates that only a very small departure from full coherence in the fundamental is required to give rise to the partially coherent harmonic source. Reasonable

[1] Orders 23 and 25 were excluded from the fit.

agreement between the fit and the deduced values is observed, suggesting the model goes someway to capturing the physics behind the phenomenon of partial spatial coherence in HHG.

5.7 Summary

In this chapter the spectral dependence of the spatial properties of HHG was investigated. Incorporation of an external pulse compression system allowed the harmonic cut-off frequency to be extended while maintaining a high photon flux. The SCIMITAR technique was used to measure the transverse intensity and phase profiles as well as the CCF of harmonic orders 23 – 43. The intensity profile width was found to increase with harmonic order, the coherence width decreases while the wavefront curvature was approximately constant for all but the lowest harmonic orders.

The intensity and coherence widths of $q = 23$ and 25 were significantly different compared to the next highest harmonic orders. We found that for these two orders alone, the absorption length was much shorter than both the calculated coherence length and the gas cell length, suggesting that absorption may play a role in the shaping of the harmonic spatial properties.

By treating the harmonic radiation as a Gaussian beam the intensity width and the wavefront curvature in the radiation generation plane were deduced. An analytic model of the source wavefront curvature agreed with the inferred values only when a fitting parameter (β) was set to a physically unrealistic value. By applying analytic expressions derived for the Gaussian-Schell model, the intensity and coherence widths in the generation plane were deduced. A harmonic intensity

described by $I_q = I_0^{\{q^n\}}$, where I_0 is the fundamental intensity and $n = 0.646 \pm 0.142$ was found to best agree with the harmonic source intensity width. A model accounting for both the effect of a partially coherent fundamental beam and the harmonic intrinsic dipole phase showed reasonable agreement with the deduced values for the harmonic source coherence width.

Chapter 6

Resolving Detailed Structures in HHG Spatial Properties

In chapter 4 it was emphasised that SCIMITAR allows the spatial coherence of light to be measured in fine detail. It stands to reason that sampling the CCF at 30+ unique pinhole separations, as is typical for a SCIMITAR scan, will provide more information than the 3–5 pinhole (or slit) separations used in previous studies on the spatial coherence of HHG [72, 85]. In this chapter we utilise this aspect of SCIMITAR to measure hitherto unreported structures in the spatial properties of high order harmonics.

It is commonly assumed that for partially coherent radiation the magnitude of the CCF ($|\mu|$) decreases with the separation of the two points at which it is measured (ΔX): starting at unity for zero separation and (eventually) falling to zero at some larger distance.[1] We show that under certain experimental conditions the CCF and intensity profile of harmonic radiation both display a marked departure from monotonic behaviour. In particular, the spatial properties are observed to develop distinctive modulations in their transverse extent (for ease, they will

[1] This is not all-encompassing. For instance, the CCF of an incoherent disc-shaped source is only monotonic for separations up to the first zero in the CCF.

be referred to as 'shoulders', for reasons that will shortly be made clear). This chapter details the characterization of such structures and comments on their potential origin. Further, calculations are presented aimed at investigating the effect the CCF modulations may have on coherent imaging experiments.

6.1 Emergence of Structures in Spatial Properties

The spatial properties of high order harmonics generated by 22 fs duration fundamental pulses were characterized using SCIMITAR. After setting the backing

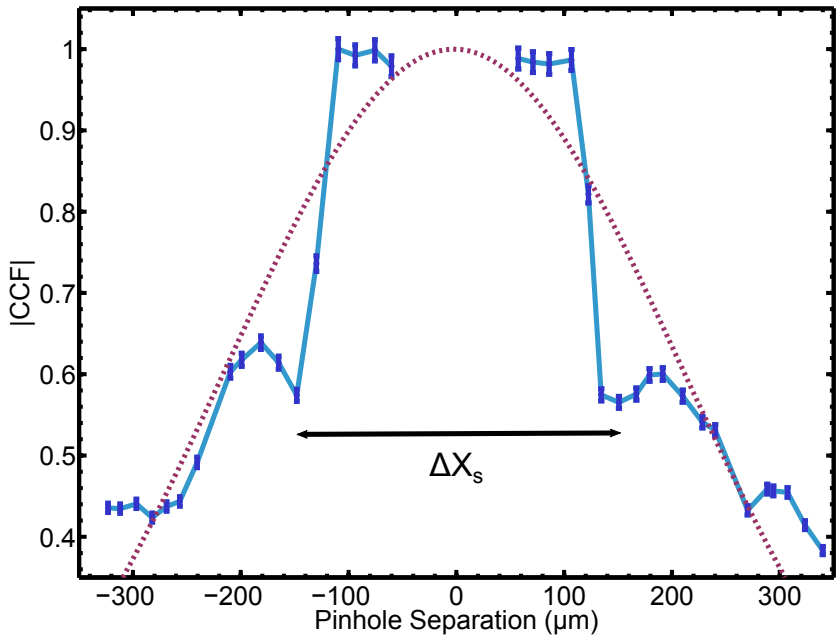

Figure 6.1: The CCF magnitude for $q = 29$ is plotted with purple dots. The dotted brown line is a Gaussian fit to all data points. The solid blue line serves to guide the eye. A clear departure from monotonic behaviour is observed for separations near $\Delta X = \pm 150\,\mu$m and $\Delta X = \pm 275\,\mu$m.

pressure in the HCF to 300 mbar, the pulse duration was measured to be 21.8

fs (FWHM) using a GRENOUILLE. The harmonic cut-off was observed to lie around $q = 37$, a decrease from that reported in the previous chapter. Using the same experimental arrangement as depicted in figure 5.3, a SCIMITAR scan was performed. Under these experimental conditions the recovered intensity profile and CCF were found to possess clear 'structures', not seen in harmonics generated by 14 fs duration pulses. An example of this new phenomenon is shown in figure 6.1, where $|\mu|$ is plotted for $q = 29$.

In figure 6.1, deep modulations occur symmetrically at $\Delta X = \pm 150$ μm and again at $\Delta X = \pm 275$ μm. A Gaussian fit is overlaid on the data to emphasise the departure from monotonic behaviour. The errorbars were calculated by fixing the pinhole separation and taking four consecutive acquisitions. The error (σ_μ) was

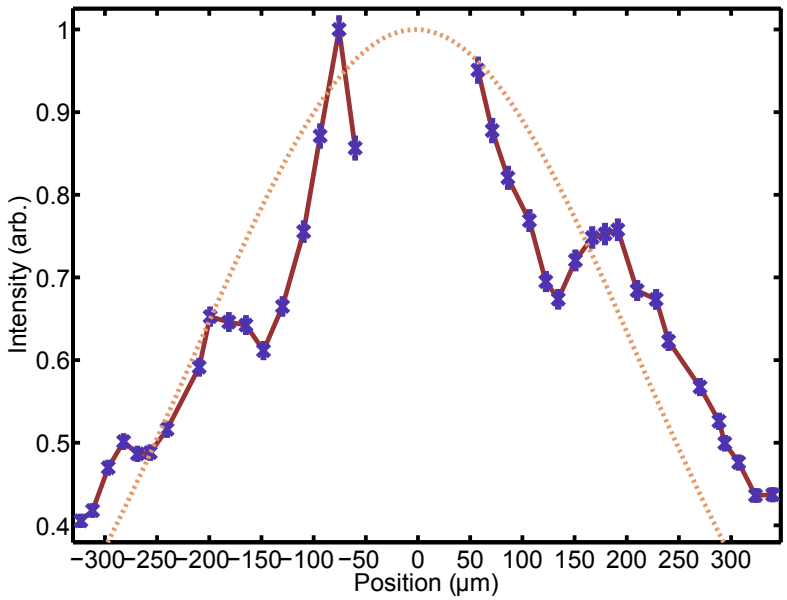

Figure 6.2: The recovered intensity profile for $q = 29$ is plotted with purple crosses. Again a Gaussian fit (dotted orange line) is used to emphasise the irregularity in the form presented by the experimental data. The brown line serves to guide the eye only.

extrapolated to other pinhole separations by assuming $\frac{\sigma_\mu}{|\mu|}$ was a constant for all data points. Clearly, the modulations in the recovered CCF cannot be explained by the estimated uncertainty in the measurement.

In figure 6.2 the intensity profile of $q = 29$ is plotted. As with the CCF, 'shoulders' are observed in the intensity profile, although the depth and position of the modulation is slightly different on the two sides of the beam.

Similar modulations were observed in the other harmonic orders recorded. To

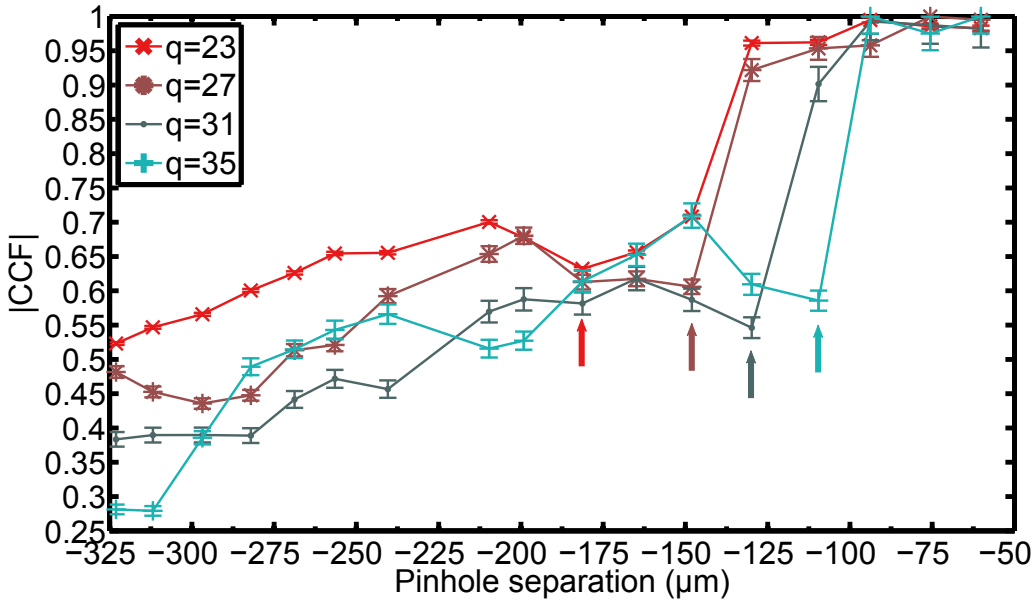

Figure 6.3: Left of centre CCF magnitude plotted for four different harmonic orders: $q = 23$ (red crosses), $q = 27$ (brown asterisks), $q = 31$ (grey dots) and $q = 35$ (blue plus signs). The solid lines serve to guide the eye. The arrows indicate the position of the characteristic dip for the harmonic order matching the arrow colour.

demonstrate this, in figure 6.3 the (left of centre) CCF of four selected harmonic orders are plotted. The distinctive shoulders are apparent for each order, however the position and depth of the modulation appears to change with q. This is made

clearer by the position of the four arrows in figure 6.3 which correspond to the locations of the (first) minima in the CCF. The arrow colour corresponds to a particular harmonic order, as defined in the legend of figure 6.3. The position of the dip occurs at larger separations for lower harmonic orders.

In order to more systematically study the spectral dependence of the CCF shoulders, the position and depth of the modulations were extracted as a function of harmonic order. We define here the 'shoulder depth' (D) as the CCF evaluated at the bottom of the modulation in the first shoulder. It is a measure of how deep a modulation is present. Since there are two minima, one either side of the beam centre, we quote the mean of the two values of D. The 'shoulder width' (ΔX_S) is defined as the full separation between the (first) two minima in the full CCF. In figure 6.1 ΔX_S is depicted by a black arrow. Effectively, it is a measure

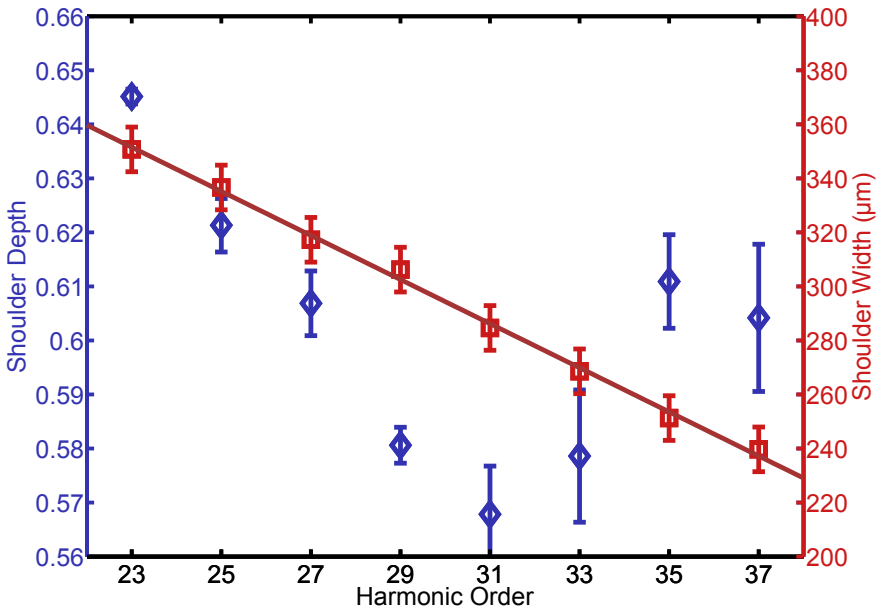

Figure 6.4: Shoulder depth (blue diamonds) and width (red squares) both plotted as functions of harmonic order. The brown line is a linear fit to the shoulder width.

of how broad the structure is. In order to better estimate these two qualities the measured harmonic CCF was first interpolated[1] and then smoothed with a running average length of two (experimental) data points. This process was aimed at overcoming any undersampling of the CCF structures.

In figure 6.4 D and ΔX_S are both plotted as functions of harmonic order. The depth is shown to initially decrease to a minima at $q = 31$ before recovering for higher orders. More strikingly the shoulder width presents a very clear linear dependence on harmonic order: ΔX_s is observed to decrease linearly with q.

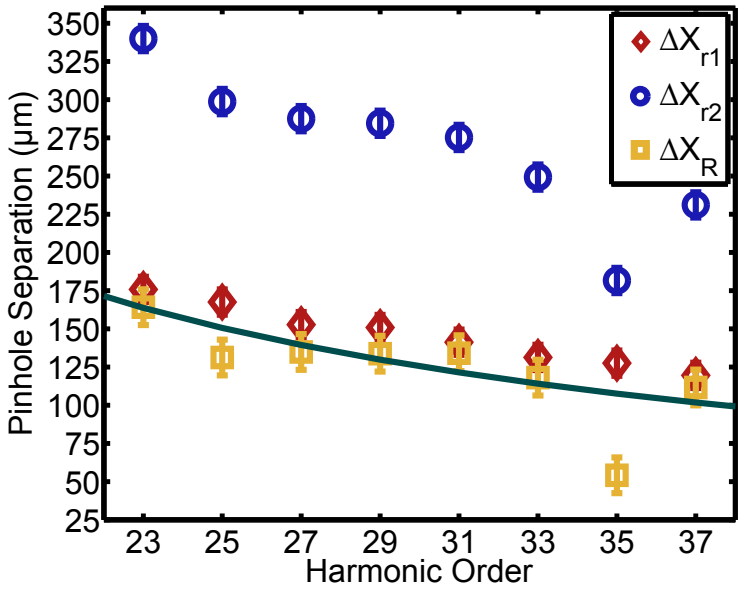

Figure 6.5: The pinhole separation where the first CCF shoulder (red diamonds) and the second shoulder (blue circles) are found. Data is shown for the CCF recorded right of the beam centre and plotted for the eight harmonic orders observed. The difference between the two pinhole separations ($\Delta X_R = \Delta X_{r2} - \Delta X_{r1}$) is plotted with gold squares. A fit of equation 6.2 to ΔX_R is shown by the green solid line.

[1]MATLAB's default linear interpolation was used with 9 points interpolated between experimental data points.

Close inspection of figure 6.1 reveals that a second distinct modulation is present at a larger pinhole separation ($\approx \pm 275\,\mu$m) compared to the separation associated with the first modulation ($\approx \pm 150\,\mu$m). Focussing on just the CCF right of centre, the location of this secondary shoulder is plotted in figure 6.5 as a function of harmonic order. The first modulation location is labelled by ΔX_{r1}, while the second is labelled by ΔX_{r2}. Also plotted in figure 6.5 is the difference ($\Delta X_{\mathrm{R}} = \Delta X_{\mathrm{r2}} - \Delta X_{\mathrm{r1}}$). With the exception of one anomalous data point, ΔX_{R} is found to slowly decrease with harmonic order. Figure 6.5 also shows that $\Delta X_{\mathrm{r2}} \approx 2\Delta X_{\mathrm{r1}}$ suggesting that the modulation in the CCF may be periodic with pinhole separation.

6.2 Origin of Modulated Spatial Properties

The existence of such clear structures in the harmonic spatial properties, as presented in section 6.1, demands an investigation into their origin. Here we explore possible explanations as to what experimental conditions give rise to modulated harmonic spatial properties.

By virtue of the experimental arrangement, the harmonic beam undergoes free-propagation from the gas cell exit to the SCIMITAR X-slit; there are no apertures or optics in place that could potentially modify the harmonic spatial properties before the beam is characterized. Therefore it is reasonable to focus on the nature of the harmonic source itself, and whether it could have produced the modulations observed.

6.2.1 Van Cittert-Zernike Theorem

The Van Cittert-Zernike theorem relates the measured CCF of radiation with the intensity profile of an equivalent[1] incoherent source $[I(x)]$ through a Fourier transform relation. In our case $I(x)$ can be thought of as being is located at the exit of the gas cell. The requirement that the source is incoherent simplifies the task of propagating the light to the plane of characterization at the expense of being unrealistic for high harmonic radiation. In section 3.2.1 it was shown that:

$$\mu(\Delta X) = N \exp(i\psi)\mathcal{F}[I(x)] \tag{6.1}$$

where ΔX denotes the separation of two test points, $\psi = -k\frac{X_1^2 - X_2^2}{2z}$ and N is a normalisation constant related to the total transmitted power. Through equation 6.1 it is expected that an aperture (of size a) in the source plane,[2] located at the exit of the gas cell, will cause a modulation in the CCF measured in a plane downstream (a distance z away) with a period:

$$X_{\mathrm{m}} \approx 0.4553\frac{\lambda_0 z}{aq}. \tag{6.2}$$

A fit of equation 6.2 to ΔX_{R} is shown in figure 6.5.[3] Assuming $\lambda_0 = 800$ nm and $z = 0.72$ m, a value of $a = 69.6 \pm 5.2\ \mu$m is deduced, with the error derived from the uncertainty of the fit. This is slightly larger than the measured FWHM of the fundamental spot size ($\approx 48\ \mu$m). Referring back to the VCZ theorem,

[1] It is equivalent in the sense that the intensity profile is that of an incoherent source which would produce radiation with a CCF as measured.

[2] To be clear, 'source' always refers to the location the radiation physically originates from.

[3] The anomalous data point for $q = 35$ is ignored when fitting equation 6.2 to the measured values of ΔX_{R}.

an incoherent disc of size a produces a modulated CCF with a $\mathrm{sinc}(...)^2$ form. The CCF measured in our case does not have the same functional form. Further investigation of the source intensity profile is therefore required.

We wish to invert equation 6.1 to evaluate $I(x)$. To do so the phase of CCF (Ψ_μ) must be known. Referring back to the definition of the CCF given in section 3.1.3, it is possible to show that the phase of μ is given by:

$$\begin{aligned}\Psi_\mu &= \mathrm{Arg}[\langle E(X_1,t)E(X_2,t)^*\rangle] \\ &= \phi(X_1) - \phi(X_2)\end{aligned} \tag{6.3}$$

where $\mathrm{Arg}(...)$ denotes the argument of the (complex) function enclosed in the brackets, X_2 and X_1 satisfy $\Delta X = X_2 - X_1$, and $\phi(X_i)$ is the harmonic wavefront at point X_i. Thus, the phase of the CCF can be evaluated by measuring the wavefront of the radiation at the characterization plane.[1] If we assume for simplicity that the spatial phase is dominated by a parabolic term in X (with a radius of curvature R_q), as is the case for high order harmonics,[2] then we may write:

$$\Psi_\mu \approx \frac{k\left(X_1^2 - X_2^2\right)}{2R_q}. \tag{6.4}$$

Inverting equation 6.1, yields:

$$I(x) = \frac{1}{N}\mathcal{F}'\left\{|\mu(\Delta X)|\exp\left[\frac{-ik(X_2^2 - X_1^2)}{2(R_q - z)}\right]\right\} \tag{6.5}$$

[1] This aspect was (obliquely) referenced in [4], where the authors noted that the CCF phase was encoded in the fringe position within the interference pattern itself.

[2] This point is illustrated by figures 4.8 and 5.7.

where, as before, $\mathcal{F}'$ denotes the inverse Fourier transform. It is noted that in the limit that the distance between the source and characterization planes is so large that the source may effectively be treated as a point emitter, $R_q = z$ and thus $\Psi_\mu = -\psi$.

Prior to applying equation 6.5 to the experimentally determined CCF, the data was treated to improve the resolution and accuracy of the recovered incoherent source intensity profile. The SCIMITAR scan measured $|\mu|$ up to $\Delta X \approx \pm 330\ \mu$m. In order to better resolve features in $I(x)$ close to the optical axis, the CCF was extrapolated to large values of ΔX (± 3 mm). To do so, $|\mu|$ was assumed to take the form of a Gaussian function at large ΔX. The width of the extrapolated Gaussian was set by fitting to the measured experimental CCF values. For small pinhole separations $|\mu|$ was assumed to be equal to unity, with

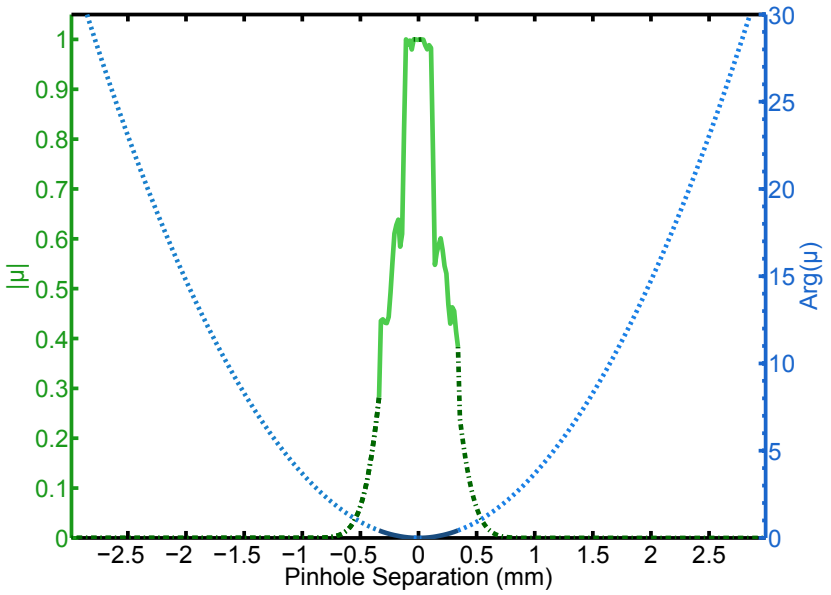

Figure 6.6: Measured $|\mu|$ for q=29 (solid green line) along with extrapolated data points (dot dashed green line). The phase of μ (solid blue line) was assumed to continue a parabolic form out to large separations (dotted blue line).

five additional data points added to fill the gap where the SCIMITAR scan was unable to record spatial coherence information. To extrapolate the phase of the CCF the harmonic wavefront was assumed to continue to be parabolic in X at large pinhole separations. To highlight this procedure the extrapolated CCF (both magnitude and phase) for $q = 29$ is plotted in figure 6.6.

Application of equation 6.5 yielded in the equivalent incoherent source, plotted for $q = 29$ in figure 6.7. It shows a central peak of FWHM = 34.85 μm flanked by low intensity structures out to approximately $x \approx \pm 250$ μm. It is noted that at some locations the incoherent source intensity falls below zero. This is clearly unphysical as the intensity is strictly a positive quantity.

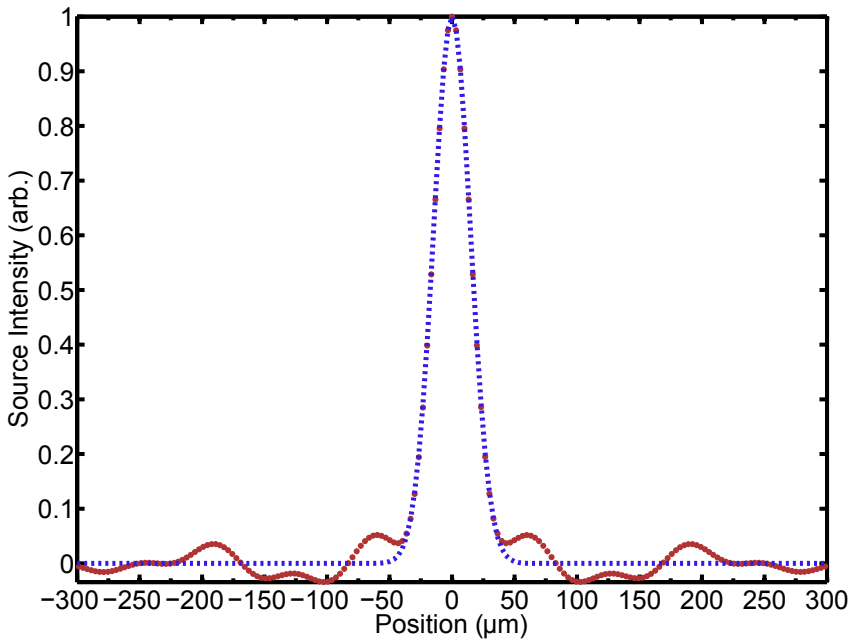

Figure 6.7: The equivalent incoherent source intensity profile for $q = 29$ is shown by the red dotted line. Uncertainty is given by the extent of the line in the vertical direction. Replacing the measured CCF with a Gaussian function, the intensity profile shown by the blue dotted line would result from the same analysis.

The negative intensity in figure 6.7 could arise from experimental uncertainty in the measured CCF. To test this hypothesis, $I(x)$ was calculated for 100 different CCFs. For each individual calculation, every value of $|\mu|$ was perturbed by a random amount in the range $\pm 2\%$. A value of 2% was used since this was the estimate for the uncertainty in a single CCF data point based upon experimentally repeating the acquisition from a single pinhole separation four times. The standard error, of each point x in the source plane, after 100 iterations, is plotted as errorbars on figure 6.7. For the most part the errors are around the same size or smaller than the symbol size. Furthermore, in all of the 100 cases calculated, $I(x)$ remained negative in the regions located at $x = \pm(100 - 150)\ \mu$m.[1] Thus experimental uncertainty is most likely not the cause of the negative intensity displayed by the equivalent incoherent source.

More likely, the negative intensity could originate from the choice of extrapolated data points added to the measured CCF. A non-Gaussian function for the extrapolated data points would yield a quantitatively different $I(x)$. In the following chapter an alternate approach to defining this 'missing' or unknown data is employed, producing an equivalent incoherent source intensity distribution that is everywhere positive.

6.2.2 Iterative Phase Retrieval Applied to the VCZ Theorem

In section 6.1 the (incoherent) source intensity profile, calculated using the VCZ theorem, was found to be negative for certain positions x in the generation plane,

[1] Even increasing the single CCF point error estimate to $\pm 10\%$ still rendered $I(x)$ negative in this region for all 100 cases.

indicating that the simple model of an incoherent source is too simplistic and/or that the necessary extrapolations of the CCF data were too crude. This result can be explored further by augmenting the VCZ theorem with an algorithm more commonly applied to phase retrieval problem in so called 'lensless' imaging experiments. For instance, in coherent diffractive imaging the scattered wavefield

	Lensless Imaging	**VCZ**
Measured Signal	Scattered Intensity $\|\Psi(X)\|^2$	CCF Magnitude $\|\mu\|$
Retrieved Phase	$\text{Arg}\{\Psi(X)\}$	$\text{Arg}\{\mu\}$
Unknown Property	Object Transmission $T(x)$	Source Intensity $I(x)$

Table 6.1: A brief comparison of the analogous quantities when comparing the problems of lensless imaging and inversion of the Van Cittert-Zernike theorem.

from some object must be back-propagated in order to retrieve the object transmission function. Likewise, in the Van Cittert-Zernike theorem, the CCF is back propagated to obtain the (equivalent incoherent) source intensity profile. The specific quantities which form the analogy are presented in table 6.1.

In the case of imaging, one wishes to find a solution to the phase, otherwise lost in a measurement, which is consistent with the measured far-field data and known information about a scattering object. The phase is found through an iterative process, with constraints applied both in the plane of the measured data and the plane of the (scattering) source. This is implemented computationally and here we focus on the algorithm first described by Fienup (the term GS[1] algorithm, or GS programme for our specific implementation, will be used hereafter) [93]. Generically, the GS algorithm can be represented by the flowchart in figure 6.8.

One benefit of GS (and other related algorithms) lies in the potential of deriving values for 'missing data'. In the case of the SCIMITAR measurement,

[1]GS stands for Gerchberg-Saxton, the names of two early proponents of the method.

data is not recorded for very small and very large pinhole separations. As will be

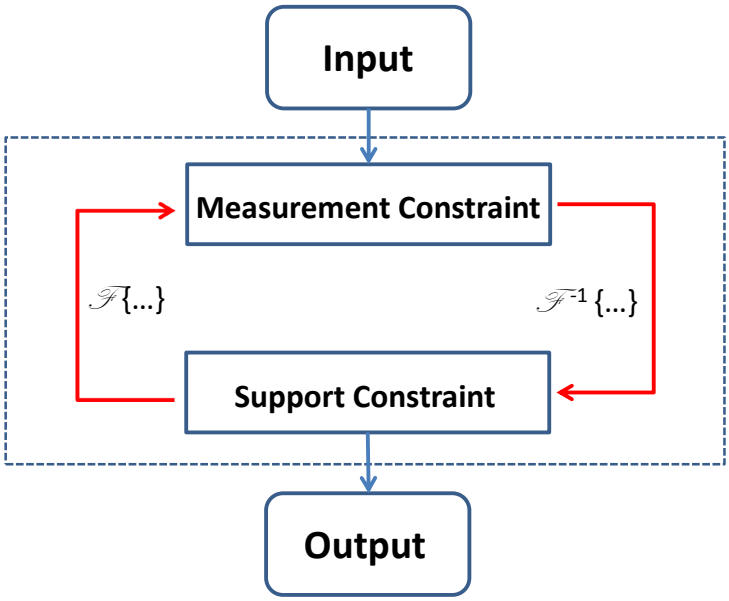

Figure 6.8: Flowchart describing a generic Gerchberg-Saxton algorithm. The actions enclosed within the dotted line are executed once per iteration. The Fourier transform and inverse Fourier transform are represented by $\mathcal{F}\{...\}$ and $\mathcal{F}^{-1}\{...\}$, respectively.

shown, through application of an iterative phase retrieval algorithm it is possible to deduce estimates for this missing data given the constraint that the incoherent source intensity must be a real and positive function of x. At the same time, the programme yields a solution for the incoherent source intensity profile $I(x)$ that best satisfies both the measured CCF and the constraints place upon $I(x)$.

Modifications are required to the GS algorithm in order to make it compatible with the VCZ theorem. The (specific) algorithm we employ is as follows:

1. Input

   Let μ_{g} be the measured CCF and $\{\Delta X_{\mathrm{m}}\}$ be the set of pinhole separations μ_{g} was measured over. Also, let $\{\Delta X_{\mathrm{r}}\}$ be the set of separations where the CCF was not measured[1] such that the two sets are disjoint and the maximum(minimum) values of $\{\Delta X_{\mathrm{r}}\}$ are larger(smaller) than the maximum(minimum) values of $\{\Delta X_{\mathrm{m}}\}$. Prior to the first iteration, the phase of the CCF is set to $\mathrm{Arg}(\mu)$ (an expression for the phase is found in equation 6.4). The CCF phase is extrapolated such that it spans the range of $\{\Delta X_{\mathrm{r}}\}$.

   For the first iteration, the CCF magnitude is:

   $|\mu_{\mathrm{g}}|$ if $\Delta X \in \{\Delta X_{\mathrm{m}}\}$ and

   $B \times r_1$ if $\Delta X \in \{\Delta X_{\mathrm{r}}\}$,

   where r_1 denotes a random number in the range [01] and $B = 1$ for points at small ΔX and $B = 0.01$ for points at large ΔX. The initial CCF magnitude and phase, used for one particular execution of the programme, are shown in figure 6.9.

2. Iteration Step: Support Constraint

   The CCF is inverse Fourier transformed. The support constraint is then applied: the incoherent source must be a real, positive function hence the real part of the inverse transformed CCF is retained and all negative values are set to zero. In recognition that harmonic generation is localised close to the optical axis, all values of the intensity where $x > \pm w_{\mathrm{d}}$ is satisfied are also set to zero, where w_{d} is referred to as the 'support width'. After all support constraints are applied we arrive at solution #1 for $I(x)$: $I_1(x)$.

[1] The maximum and minimum values chosen for $\{\Delta X_{\mathrm{r}}\}$ were found to have little effect on the output of the GS programme.

3. Iteration Step: Measurement Constraint

   The solution $I_1(x)$ is Fourier transformed to yield solution #1 for μ: μ_1. The phase of μ_1 is retained (ϕ_1). The Fourier transform brings us to the

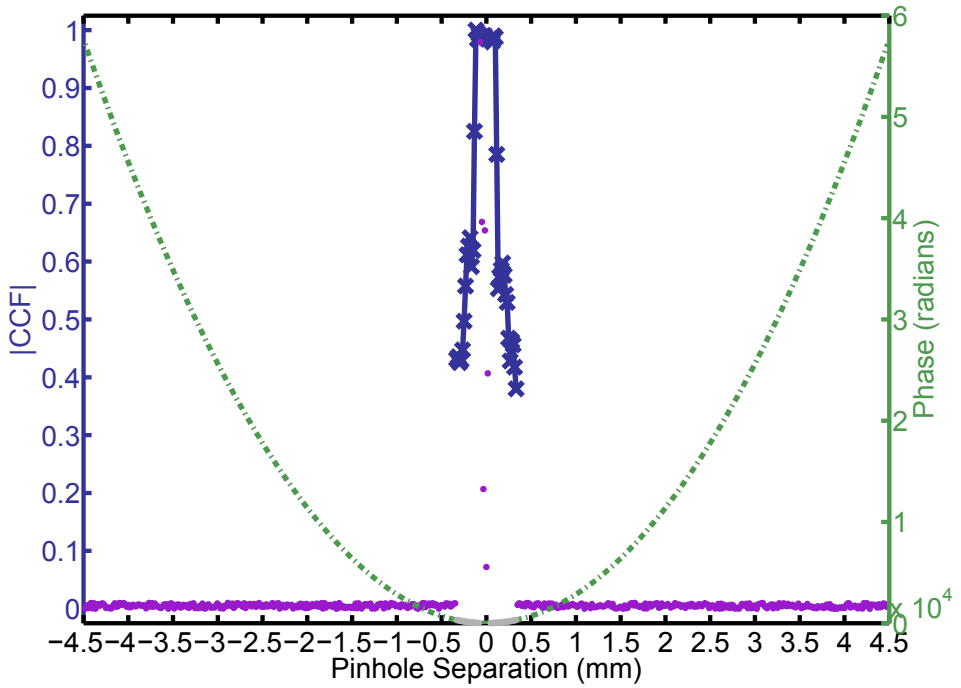

Figure 6.9: CCF magnitude (blue x's) and phase (grey dots) used to initiate one particular run of the GS programme. The pink dots and green dot-dashed line show the CCF magnitude and phase, respectively, at pinhole separations where the no data was collected.

plane the measurement of the CCF was recorded in. Here we wish to apply constraints that force the deduced CCF points 'close' to those that were measured. Mathematically the measurement constraint can be phrased as:

$$\text{if } |\mu_1(\Delta X_\mathrm{m})| > (1+\zeta)|\mu_\mathrm{g}(\Delta X_\mathrm{m})| \quad \text{then } |\mu_2(\Delta X_\mathrm{m})| = (1+\zeta)|\mu_\mathrm{g}(\Delta X_\mathrm{m})|$$

$$\text{if } |\mu_1(\Delta X_\mathrm{m})| < (1-\zeta)|\mu_\mathrm{g}(\Delta X_\mathrm{m})| \quad \text{then } |\mu_2(\Delta X_\mathrm{m})| = (1-\zeta)|\mu_\mathrm{g}(\Delta X_\mathrm{m})|$$

$$\text{if } (1-\zeta)|\mu_\mathrm{g}(\Delta X_\mathrm{m})| < |\mu_1(\Delta X_\mathrm{m})| < (1+\zeta)|\mu_\mathrm{g}(\Delta X_\mathrm{m})| \quad \text{then } |\mu_2(\Delta X_\mathrm{m})| =$$

$|\mu_1(\Delta X_{\mathrm{m}})|$

and

$|\mu_2(\Delta X_r)| = |\mu_2(\Delta X_r)|$

where ζ is a 'tolerance' parameter. Steps 2 and 3 are repeated until the algorithm either converges to a solution or stagnates.

In the third step, ζ, the tolerance parameter, is used to modify the constraint in the measurement plane. When $\zeta = 0$, the constraint forces the j^{th} solution for the CCF (μ_j) through the experimentally determined CCF (μ_{g}). When $\zeta \neq 0$, $\mu_j(\Delta X_{\mathrm{m}})$ is forced closer to $\mu_g(\Delta X_{\mathrm{m}})$: it acts to 'soften' the constraint, by forcing $\mu_j(\Delta X_m)$ to within a certain bound of the measured value. The tolerance parameter must be defined by the user prior to execution of the programme. Values of the CCF beyond the domain over which it was measured [$\mu_j(\Delta X_{\mathrm{r}})$] are allowed to take on any value. In this way, the GS algorithm should, after the execution of many iterations, selects values for $\mu_j(\Delta X_r)$ which satisfy the source constraints.

To test the progress of the GS algorithm an error metric is needed. The j^{th} solution of the CCF, prior to application of the measurement constraint, can be compared to the measured CCF values (μ_g). The error (ϵ_j) is defined as:

$$\epsilon_j = \frac{\Sigma\Big[|\mu_{\mathrm{j}}(\Delta X_{\mathrm{m}}) - \mu_{\mathrm{g}}(\Delta X_{\mathrm{m}})|\Big]}{\Sigma\mu_{\mathrm{g}}(\Delta X_{\mathrm{m}})} \tag{6.6}$$

where the sum is made over all the pinhole separations found in $\{\Delta X_{\mathrm{m}}\}$. When $\epsilon = 0$ the programme is judged to have converged to an exact solution, prior to this point $\epsilon > 0$. Larger values of ϵ correspond to solutions less consistent with

the measured CCF values.

A programme to execute the GS algorithm was written in MATLAB. After (successful) testing with artificially created data the GS programme was applied to the experimentally measured CCF for $q = 29$. In figure 6.9 the magnitude and phase of the experimental CCF are shown. The purple dots and green dash dotted line show the CCF magnitude and phase, respectively, at points not measured during the experimental run, that were used for the first iteration of the programme. For subsequent iterations those particular values were allowed to take on any value the GS programme allocates to them after each iteration.

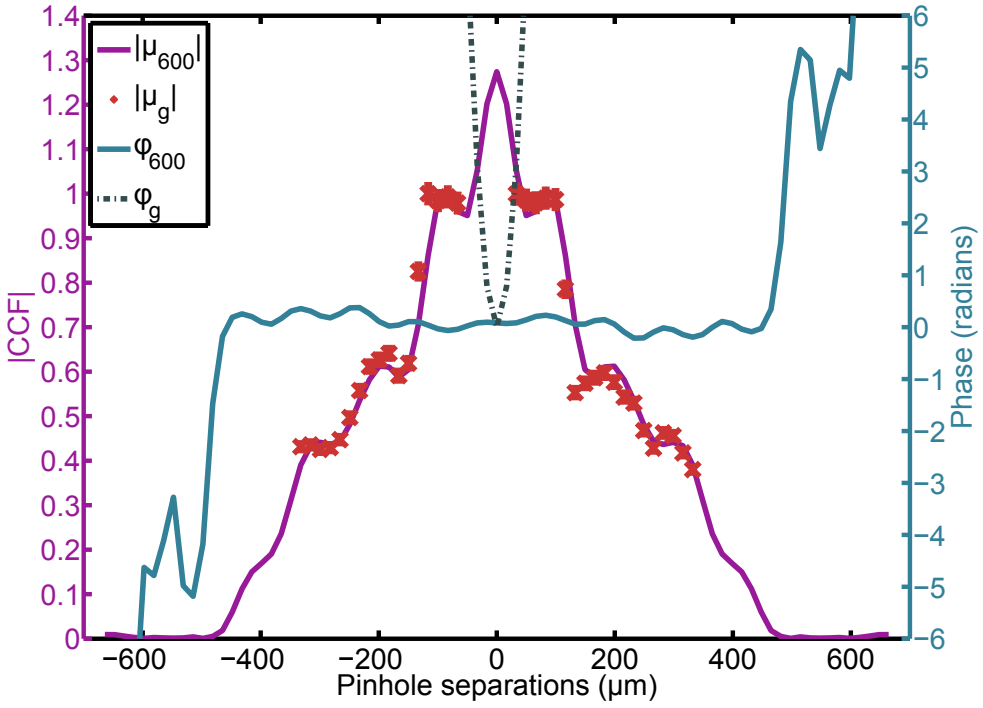

Figure 6.10: The CCF magnitude (purple line) and phase (solid green line) derived after 600 iterations of the GS programme and for $\zeta = 0$. The measured CCF magnitude and phase are given by the red crosses and grey dot-dashed line, respectively.

The magnitude and phase of the CCF derived after 600 iterations of the GS programme, with $\zeta = 0$ and $w_{\mathrm{d}} = 250\ \mu$m.[1] are shown in figure 6.10. It should be noted that the CCF deduced by the GS programme is simply the Fourier transform of the incoherent source intensity profile derived from the same programme.

Excellent agreement between the $|\mu_{\mathrm{g}}|$ and $|\mu_{600}|$ is observed. Interestingly, a further modulation in the CCF at $\Delta X = \pm 400\mu$m is retrieved, beyond the range of the SCIMITAR measurement. This is further evidence in favour of the modulation of the CCF being periodic with pinhole separation. At large pinhole separations the GS programme yields CCF values close to zero, as would be expected for a partially coherent radiation. The initial CCF phase and the phase after 600 iterations are both shown in figure 6.10. The discrepancy between the two quantities may be due to the uncertainty in the harmonic wavefront measurement, which contributes to the (inputted) phase of the CCF (ϕ_0).

For the very smallest pinhole separations, the GS programme retrieves a value greater than unity for the CCF magnitude. This is unphysical since $0 \leq |\mu| \leq 1$. The reason for this may well be related to the fact that the harmonic source is not incoherent, and so the Van Cittert-Zernike theorem, even with the augmentation described above, is not a suitable model for describing the harmonic source properties. It should be noted that one may be tempted to incorporate a further condition into the measurement constraint whereby μ_{j} is forced to be less than one. Including such a constraint was found to not solve the problem. When this additional constraint was added to the programme the retrieved CCF was still larger than unity for small values of ΔX while at the same time comparatively

[1] For reference, this value of w_{d} is approximately five times the focal spot size.

larger values of ϵ_j were calculated.

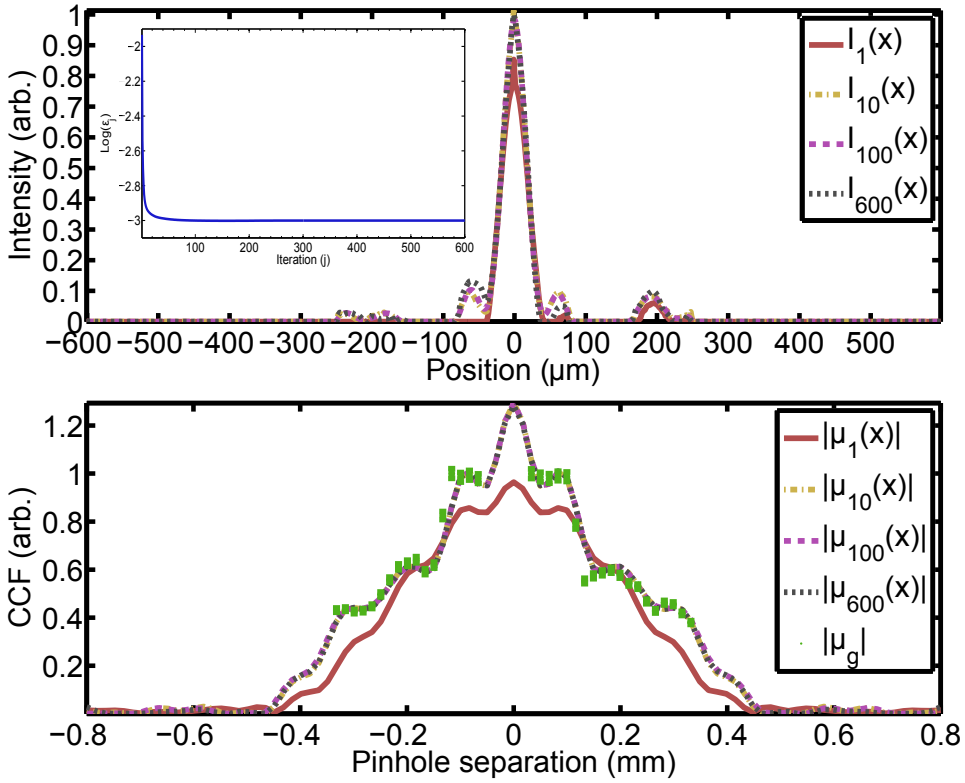

Figure 6.11: Upper plot: incoherent source intensity recovered by the GS programme extracted after four different iteration numbers (as identified in the legend), but the same starting values of μ. In the inset $\log(\epsilon_j)$ is plotted as a function of iteration number (j). Lower plot: CCF magnitude at the end of the same four iteration numbers as the above plot. The measured CCF magnitude is overlaid with green dots.

In the upper plot of the figure 6.11 the deduced incoherent source intensity is plotted after four different iteration numbers. Little difference is observed for I(x) beyond 10 iterations. This is further evidenced by the inset of the upper plot where $\log(\epsilon_j)$ is plotted with iteration number, showing that, as typical for algorithms of this type [39], negligible improvement to the solution is made after 10 or so iterations: the error quickly settles to a value of approximately 0.047.

In the lower plot the CCF magnitudes corresponding to the intensity profiles of the upper plot are shown. The measured CCF is overlaid with green dots. All

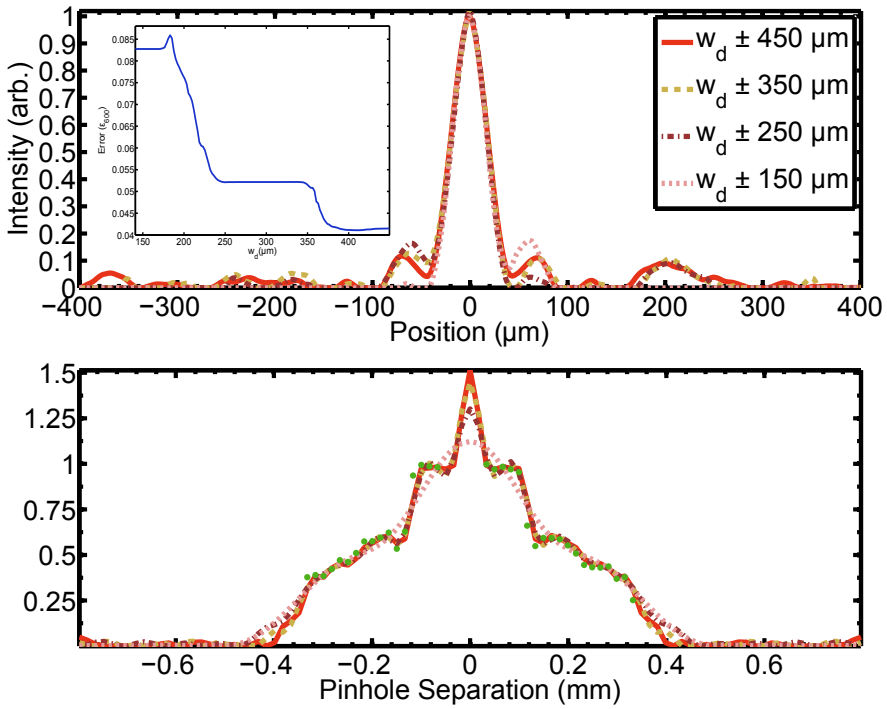

Figure 6.12: Upper plot: incoherent source intensity recovered after 600 iterations of the GS programme, with $\zeta = 0$, for different support widths (w_d). The inset shows the value of ϵ_j after the 600$^{\text{th}}$ iteration as a function of w_d. Lower plot: matching CCFs for the intensity profiles shown in the upper plot. SCIMITAR data is shown by green dots.

plots were obtained with $\zeta = 0$ and $w_{\text{d}} = 250\ \mu$m. Good agreement between measured and recovered values of the CCF is observed although for the very smallest pinhole separations $|\mu| > 1$.

In figure 6.12, $I(x)$ is plotted for a range of values for w_{d}. The variation of ϵ with w_{d} is shown in the inset. When w_{d} is large, $I(x)$ displays a highly modulated shape but with a small value for ϵ (≈ 0.044). Decreasing w_{d} results in the suppression of most of the modulations $I(x)$ at the expense of an increase

in the error: the recovered CCF is a 'smoother' and a poorer fit to experimental data. In other words, off-axis structures in $I(x)$ are needed to yield a low error value.

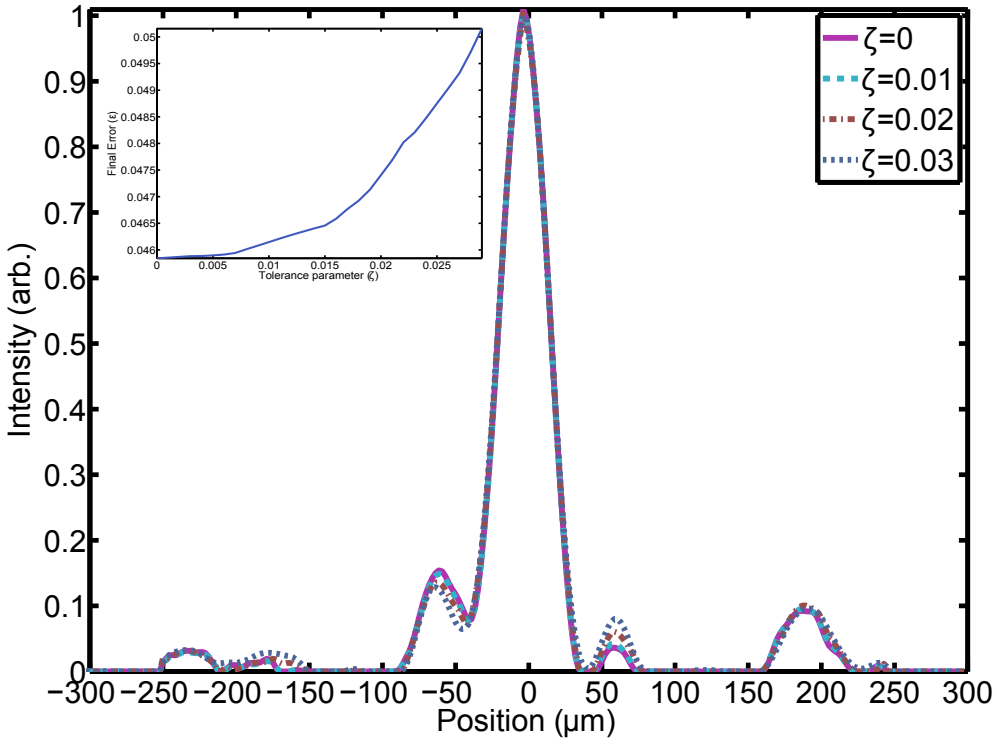

Figure 6.13: Incoherent source intensity recovered after 600 iterations of the GS programme. Each line represents the result of the programme run for different ζ values as indicated by the legend (with $w_{\mathrm{d}} = 250\,\mu$m). The inset shows the value of ϵ after the 600^{th} iteration as a function of ζ.

For all other plots in this section w_{d} was chosen to be $250\,\mu$m, as this offered a compromise between having a low error whilst yielding fewer (seemingly) unphysical structures in the source intensity profile. It is noted that the use of a fixed value for w_{d} is somewhat outdated for algorithms of the type used here. Indeed in the lenless imaging community, much success in terms of high fidelity object reconstruction has been reported by employing so called 'shrinkwrap' approaches

to defining w_d, whereby the support window is updated (reduced) in size periodically during the execution of the phase retrieval programme [82]. This approach has led to more accurate inversion of diffraction data without the requirements for a priori knowledge of the object size. A 'shrinkwrap' modification is not however employed in our case. In figure 6.13 the source intensity profile, after 600

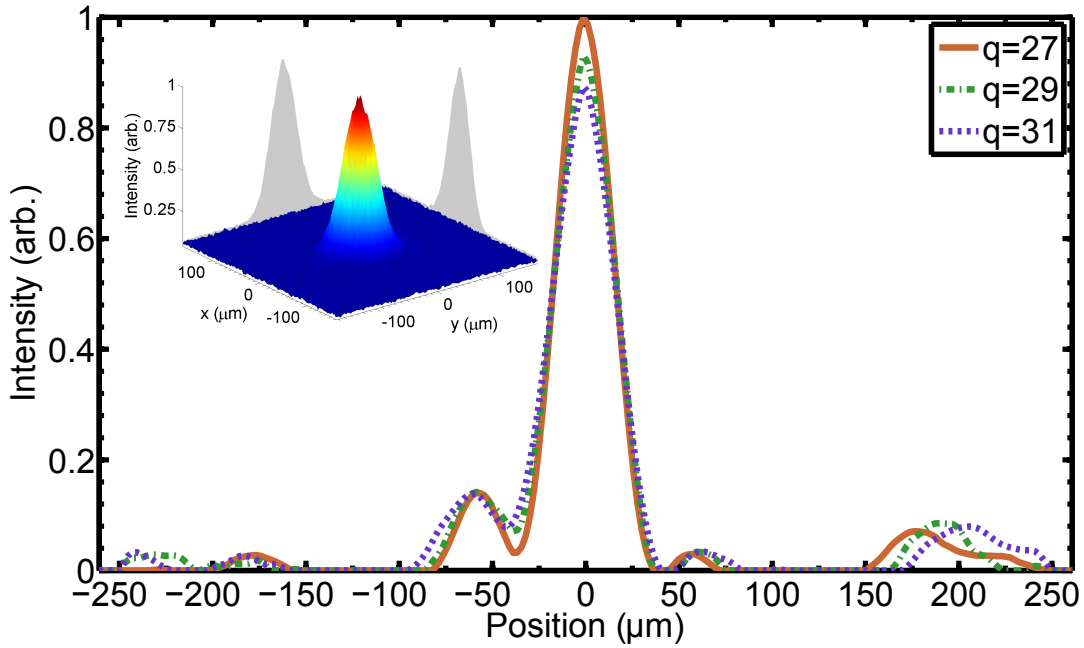

Figure 6.14: Equivalent incoherent source intensity profiles for $q = 27$ (solid brown line), $q = 29$ (green dot-dashed line) and $q = 31$ (purple dotted line). The inset shows the intensity distribution of the fundamental, recorded in situ.

iterations, for different values of the tolerance parameter ζ is shown. There is some variation depending on the value of ζ used, but broadly speaking, all executions of the GS programme yield an incoherent source intensity that is peaked on axis, with some sporadic low intensity structure ($< 10\%$ of the peak intensity) extending out to $\pm 250\,\mu$m. The inset of figure 6.13 shows the final error after 600 iterations of the GS programme as a function of ζ. The error increases slightly,

going from 0.0455 to 0.05 when ζ increases from 0 to 0.03.

When applied to other harmonic orders, the same analysis yielded qualitatively similar intensity profiles, with low intensity features located at the same locations in the source generation plane, as shown in figure 6.14. If the harmonic source is indeed shaped similar to what is presented in figure 6.14, it is not immediately clear what might cause such an irregularity.

Imaging of the fundamental focal spot, albeit at low intensity and at atmospheric pressure, did not reveal any irregularities in the laser intensity profile as evidenced by the inset of figure 6.14.[1] It may be that under the experimental conditions relevant here propagation through the partially ionized medium may lead to the distortion of the transverse profile of the driving pulse. In turn the distortion of the driving field is imparted on to the harmonic source producing the modulated spatial properties that we have measured. However it seems unlikely that such a process could lead to harmonic emission so far from the optical axis ($x > \pm 200\,\mu$m).

Alternatively, given the length of time needed to perform a SCIMTAR scan (≈ 2 hours), it is possible that a drift or instability in the fundamental may have led to the weak off-axis harmonic emission displayed in figure 6.14. However modulations were not observed in the results of other scans undertaken. Propagation simulations coupled with further experiments could shed light on whether such an unusual harmonic source shape can arise under the conditions of the experiments presented here.

The GS programme was successful in retrieving an incoherent source intensity

[1] Locations $x > \pm 150\,\mu$m are not plotted in the inset of figure 6.14 since they revealed no low intensity features above the noise level of the measurement.

profile which would yield the same (far-field) spatial coherence properties as we measured. The tolerance parameter ζ was found to not significantly change the shape of $I(x)$, but a physically realistic intensity profile required a sufficiently small value of w_{d}.

The excellent agreement between $\mu_j(\Delta X_{\mathrm{m}})$ and μ_g indicates that a more physically realistic picture of the source intensity can be derived if the Van Cittert-Zernike theorem is augmented with a Gerchberg-Saxton style iterative phase retrieval algorithm, compared with the standard approach described in section 6.1.

6.2.3 The Generalised Van Cittert-Zernike Theorem

Although the augmented Van Cittert-Zernike theorem managed to provide some insight in to the possible shape of $I(x)$, the requirement that the source is incoherent is somewhat restrictive. In particular, given that the high order harmonics are driven by a fundamental beam with high coherence and the resultant radiation has a low divergence, it stands to reason that HHG is produced by a partially coherence source. To further interrogate the origin of the modulated spatial properties the generalised Van Cittert-Zernike theorem (GVCZ theorem) may be used, first introduced in section 3.2.2. Here it is deployed to back-propagate the mutual intensity function of harmonic radiation measured using SCIMITAR, to probe both the source intensity profile $I_0(x)$ and source CCF (μ_0) simultaneously.

To recap, equation 3.47 gives an expression for the propagated mutual intensity function (J_{p}):

$$J_p(X_2, X_1, z) = \frac{1}{(\lambda z)^2} \int\int J_0(x_1, x_2)$$
$$\exp\Big\{ -i\frac{k}{2z}\Big[(X_2 - x_2)^2 - (X_1 - x_1)^2\Big]\Big\}\mathrm{d}x_1\mathrm{d}x_2 \tag{6.7}$$

where we have assumed the familiar paraxial approximation is valid. Recognising that equation 6.7 takes the form of a Fourier transform we may invert it to derive an expression for the **source** mutual intensity function:

$$J_0(x_1, x_2) = (\lambda z)^2 \exp\left[\frac{-ik}{2z}\left(x_2^2 - x_1^2\right)\right]\mathcal{F}\Big\{\mathcal{F}'\Big[J_\mathrm{P}\exp\left(i\psi\right)\Big]\Big\} \tag{6.8}$$

where $\psi = -\frac{k}{2z}(X_2^2 - X_1^2)$. The source intensity profile and CCF are retrieved from:

$$I_0(x) = J_0(x, x) \tag{6.9}$$
$$\mu_0(x_2, x_1) = \frac{J_0(x_1, x_2)}{\sqrt{I_0(x_1)I_0(x_2)}}. \tag{6.10}$$

The propagated mutual intensity (J_p) was constructed from the measured intensity, wavefront and CCF for $q = 29$. All three quantities were extrapolated to span a grid of size 3×3 mm. In the case of the intensity profile, a Gaussian was fitted to the experimental data and the intensity was assumed to take that form at points missing from the SCIMITAR measurement. The wavefront was assumed to continue as a parabola when extrapolated to span the size of the grid. Additionally, the CCF was assumed to be shift invariant such that for any point on the grid given by the coordinates $\{X_1, X_2\}$, the CCF took the value

$\mu(X_2 - X_1)$. The mutual intensity was assumed to be quasi-homogeneous, such that it takes the form of equation 3.43.

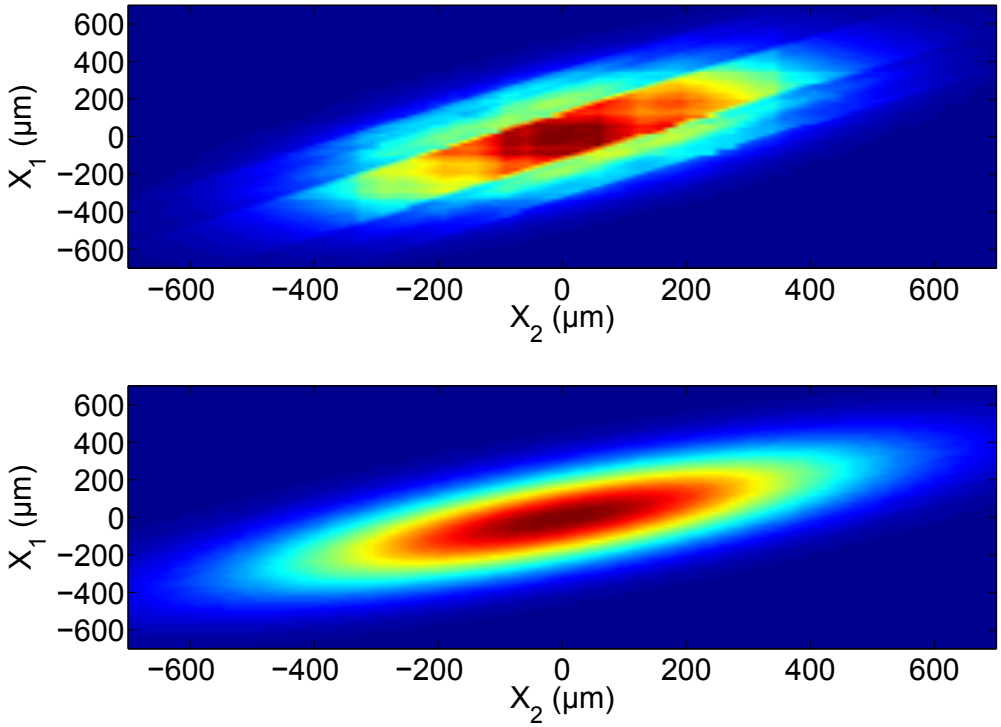

Figure 6.15: Upper plot: measured mutual intensity function $|J_p(X_1, X_2)|$ for $= 29$. The CCF was assumed to be shift invariant. Lower plot: mutual intensity function of an equivalent Gaussian-Schell model beam.

As a comparison the mutual intensity function of an 'equivalent Gaussian-Schell model beam' was also defined. The widths of the intensity profile and CCF of the GSM beam were determined by fitting to the experimental data.

In figure 6.15 $|J_p(X_2, X_1)|$, as measured at the plane of the X-slit, for $q = 29$, is shown in the upper plot. In the lower plot the mutual intensity for a Gaussian-Schell model beam, defined on the same grid as the upper plot, is also shown. The upper plot clearly presents a more structured CCF, compared with the GSM beam of the lower plot, arising from the modulated spatial properties.

The harmonic mutual intensity was (numerically) back propagated using equation 6.8 to yield the source mutual intensity function (J_0) from which the source intensity profile (I_0) and CCF (μ_0) were derived. In the upper plot of figure 6.16

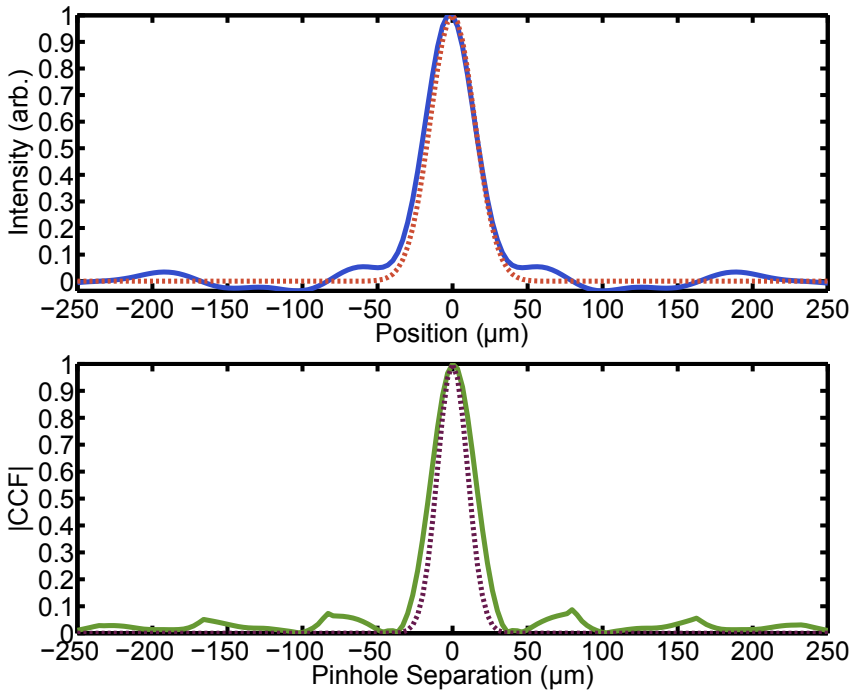

Figure 6.16: Upper plot: $I_0(x)$ derived from generalised Van Cittert-Zernike theorem (blue solid line). The dotted line is the same quantity for the equivalent GSM beam. Lower plot: $|\mu_0|$ (solid green line) found from the same back propagation method. The dotted purple line shows $|\mu_0|$ for the equivalent GSM beam.

$I_0(x)$ is shown for both harmonic and (equivalent) GSM beams. The similarity between this plot and that shown in 6.7 is apparent. Despite the GVCZ theorem providing a more physically realistic account of the harmonic source, the intensity is again found to be negative for certain positions.

The lower plot of figure 6.16 shows $|\mu_0|$ for both harmonic and (equivalent) GSM beam. The harmonic CCF is peaked on axis but displays low amplitude modulations out to large pinhole separations, the origins of which are unclear.

As with the VCZ theorem, the GVCZ theorem could benefit from a similar Gerchberg-Saxton inspired approach, as developed in section 6.2.2. However the complexity of such a task is considerable: to propagate, back and forward between source and measurement planes, would require both a 2-D Fourier transform and multiplication by a (2-D) phase factor for each propagation step (two propagation steps per iteration). The computational resources and potential for error scale considerably, compared to the 1-D case presented in section 6.2.2, putting the task beyond the scope of this thesis.

6.2.4 Comparing Driving Pulses

Comparing the experimental conditions for when the shoulders are present with those of the previous chapter, where such structures were not apparent (see figure 5.8 for comparison), the only significant difference is in the (measured) duration of the driving pulses. Irregularities in the temporal pulse profile could lead to, for instance, a harmonic source composed of both neutral and ionised gas. It is therefore natural to take a closer look at the driving pulse temporal properties while also evaluating the level of ionization in the medium.

In figure 6.17 the temporal intensity and temporal phase are plotted for the driving pulses used in chapter 5 (upper plot) and in this chapter (lower plot). The data was recorded using the GRENOUILLE and retrieved using a commercial implementation of the generalised projection algorithm (Femtosoft software).

There is nothing extraordinary about either pulse shown in figure 6.17. The 22 fs duration pulse, presented in the lower plot, shows a small structure at -35 fs, but this is of low intensity ($\approx$ 10% of the peak) and so should not con-

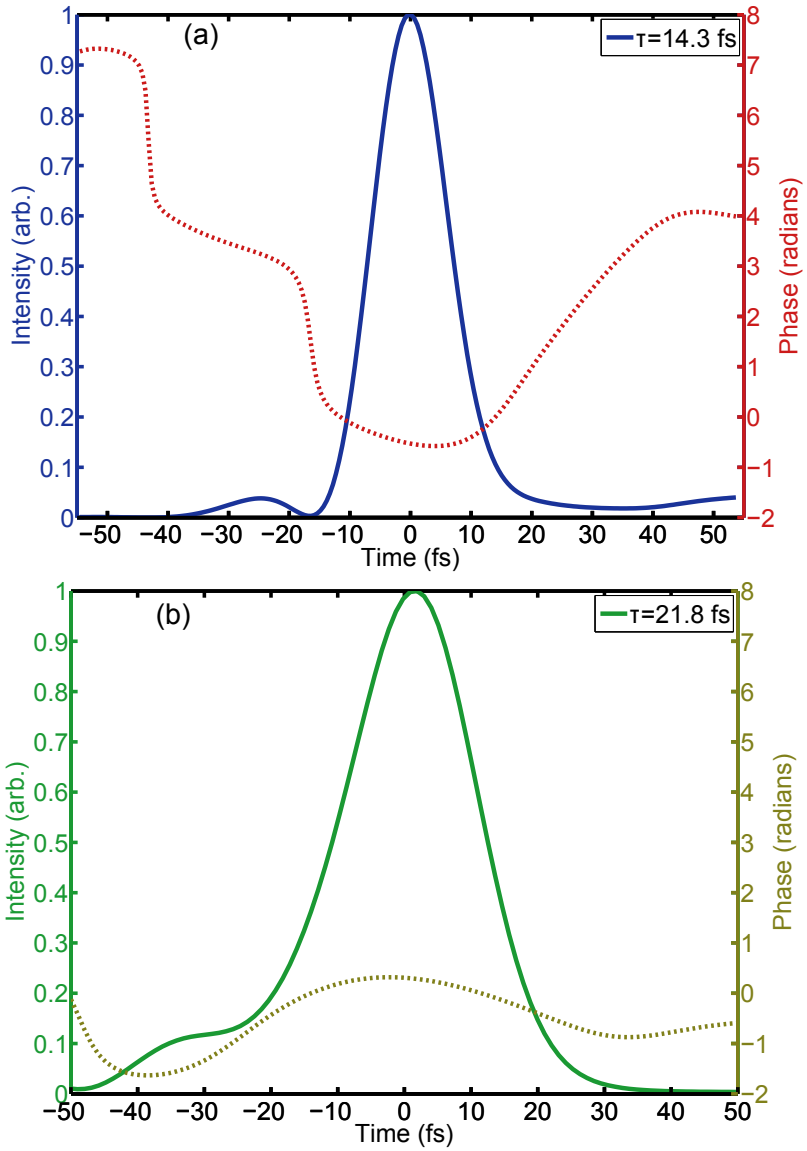

Figure 6.17: (Normalised) temporal intensity (solid lines) and phase (dotted lines) of driving pulses used for experiments described in the previous (upper plot) and current chapter (lower plot). Temporal characterization was performed using the GRENOUILLE. The pulse durations quoted were read off from the Femtosoft software. In the upper plot the 'FROG error' was 2.65%, the lower 4.4%.

tribute significantly to the harmonic generation process. It should also be noted that this temporal artefact may in fact occur *after* the temporal peak, since the GRENOUILLE yields the pulse temporal properties with no defined direction of time. In the case of the 22 fs pulse, the FROG error was relatively large, 4.4%. Large FROG errors can be symptomatic of both complex spatio-temporal effects in a single pulse and an element of randomness in the pulse train [48]. However the fact that the 22 fs duration pulses produced stable high order harmonics suggests that the large error may instead come from deficiencies in the FROG software itself.

Knowledge of the pulse temporal properties, combined with the pulse energy and spot size) allows the ionization fraction (η) to be calculated as function of time. A programme, adapted from [97], based on the ADK formularism [3], was used along with the experimentally determined laser temporal properties, extracted from the FROG software.

Figure 6.18 shows the calculated temporal variation of the (on axis) fraction of atoms ionized into either the first charged state or second charged state, assuming the temporal laser profile presented in the lower plot of figure 6.17. The leftmost plots are for the fundamental laser pulses used in this chapter, with the lower left plot showing the results for a time-reversed pulse. The rightmost plots show the results for the same calculation but for the fundamental pulses of chapter 5.

For the 21.8 fs duration pulse the level of Ar^{2+} is shown to be low ($\leq$ 8%) and only reaches its maximum level when the total ionization in the medium is high ($>$ 90%), suggesting that the contribution to the harmonic emission from ions should be negligible. This also true for the time-reversed pulse.

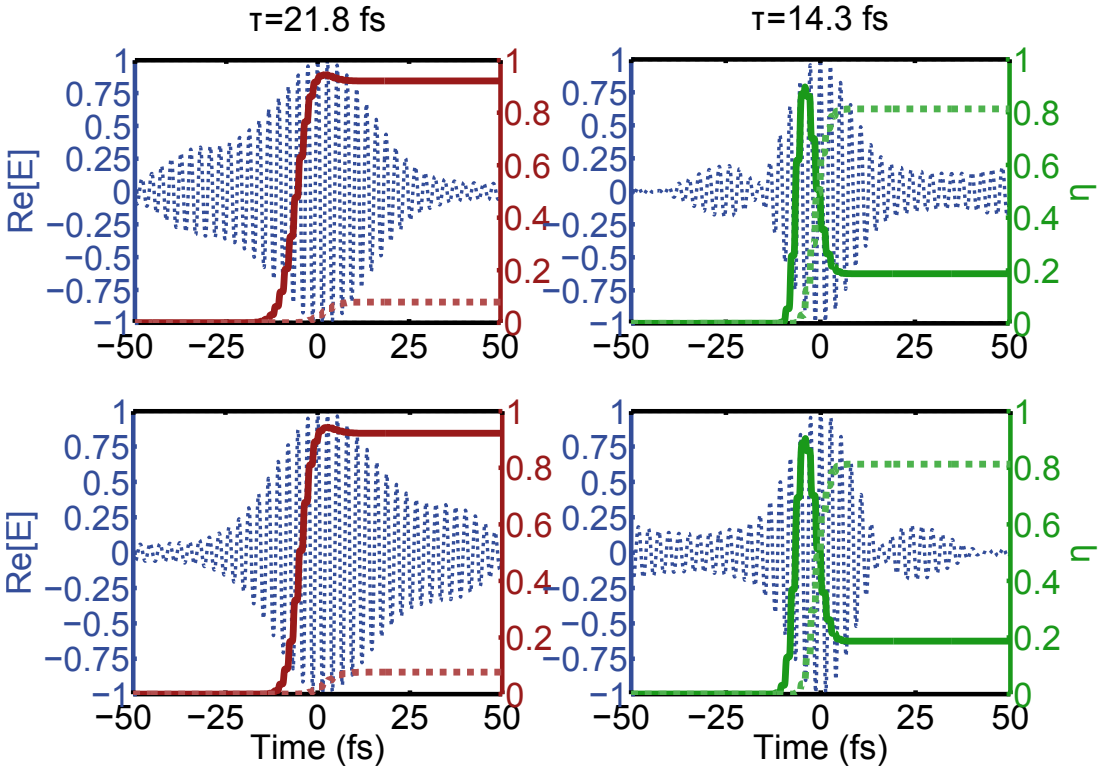

Figure 6.18: For all plots the fraction of atoms in the +1 charge state is shown by solid line and +2 charge state by a dashed line. The blue dotted line shows the electric field of the fundamental, assuming a carrier envelope phase of 0. The lower plots show the same as the upper plots but for a time-reversed fundamental pulse. The rightmost plots show the same quantities as the leftmost but for the fundamental pulse used in chapter 5.

6.3 Consequences of Modulated HHG Spatial Properties

A question remains unanswered regarding what impact, if any at all, the fine structures in the harmonic spatial properties could have on current experimental applications of HHG. Techniques which make use of diffraction, such as coherent diffractive imaging (CDI), may suffer adversely from the irregularities found in the harmonic intensity profile and spatial coherence.

In an attempt to qualitatively assess any deleterious effect, we have numerically simulated diffraction from a 1-D binary structure. Two cases are compared, both shown in figure 6.1: diffraction is calculated for one beam with the experimentally determined CCF and for another with a Gaussian CCF. The width of the Gaussian was determined by a fit to the measured data shown in figure 6.1.

6.3.1 Diffraction of Partially Coherent Light

The intensity pattern produced by an amplitude mask illuminated by partially coherent light can be modelled using statistical optics, as described by Goodman in [98]. Similar to the derivation of the Generalised Van Cittert-Zernike theorem in chapter 3, we use the mutual intensity (J) function to describe the spatial properties of the diffracted light. Again we assume the radiation source is quasi-homogeneous, that is:

$$J_0 = A(x_1)A(x_2)^*\mu(\Delta x) \tag{6.11}$$

where $A(x_i)$ is the wave amplitude at location x_i. The amplitude of the transmitted light $[A_t(x)]$ can be related to the incident amplitude $[A_i(x)]$ through:

$$A_t(x,t) = t_A(x)A_i(x, t-\tau_0) \tag{6.12}$$

where $t_A(x)$ is the amplitude transmission function and τ_0 is a time delay introduced by the diffracting object. Here we will assume that the amplitude mask is infinitely thin and causes no discernible delay. Thus further references to τ_0 are dropped. The mutual intensity of the transmitted light may be written as:

$$\begin{aligned} J_t &= \langle A_t(x_1)A_t(x_2)^*\rangle \\ &= t_A(x_1)t_A(x_2)^*\langle A_i(x_1)A_i(x_2)^*\rangle \\ &= t_A(x_1)t_A(x_2)^*J_i(x_1,x_2). \end{aligned} \tag{6.13}$$

The transmission function can be replaced with a pupil function $[P(x)]$, which may be complex, without loss of generality. Previously, equation 3.45 was used to derive the propagated mutual intensity. Here, it is used to calculate the diffracted intensity pattern through:

$$I(X) \cong \frac{1}{(\lambda z)^2}\int\int P(x_1)P(x_2)^*J_i(x_1,x_2)\exp[-ik(r_2-r_1)]\mathrm{d}x_1\mathrm{d}x_2. \tag{6.14}$$

$$= \frac{1}{(\lambda z)^2}\int\int P(x_1)P(x_2)^*\mu(x_2-x_1)\exp[-ik(r_2-r_1)]\mathrm{d}x_1\mathrm{d}x_2. \tag{6.15}$$

where, in the second line, the amplitudes A_t have been absorbed into the pupil functions P. Making the usual paraxial approximation and changing variables

yields:[1]

$$I(X) = \frac{1}{(\lambda z)^2}\int\int P\Big(\bar{x} - \frac{\Delta x}{2}\Big)P\Big(\bar{x} + \frac{\Delta x}{2}\Big)^* \\ \mu_i(\Delta x)\exp\Big(-i\frac{k}{z}\bar{x}\Delta x\Big)\exp\Big(i\frac{k}{z}X\Delta x\Big)\mathrm{d}\bar{x}\mathrm{d}\Delta x. \tag{6.16}$$

In section 3.2.2 a similar equation was derived after propagating the mutual intensity in free space. Applying the (same) assumption: $z > 4\frac{x\Delta x}{\lambda}$ allows us to drop the first exponential factor in equation 6.16 giving:

$$I(X) = \frac{1}{\lambda z}\int\int \mathcal{P}(\Delta x)\mu_i(\Delta x)\exp\left(i\frac{k}{z}X\Delta x\right)\mathrm{d}\Delta x \tag{6.17}$$

where $\mathcal{P}$ is the autocorrelation of the pupil function P:

$$\mathcal{P}(\Delta x) = \int P\left(\bar{x} - \frac{\Delta x}{2}\right)P\left(\bar{x} + \frac{\Delta x}{2}\right)^*\mathrm{d}\bar{x}. \tag{6.18}$$

Equation 6.17 shows that the diffracted intensity measured a distance z from a structure is given by the (scaled) Fourier transform of the product of the autocorrelation of the pupil function and the CCF (evaluated at the plane of the diffracting object). Using both the convolution theorem and the Weiner-Khinchin theorem allows equation 6.17 to be written in the more compact form:

$$I(X) = \frac{1}{(\lambda z)^2}|\mathcal{F}[P(x)]|^2 * \mathcal{F}[\mu(\Delta x)] \tag{6.19}$$

[1]The same two steps were made in deriving the generalised Van Cittert-Zernike theorem in section 3.2.2.

where, as before, $*$ denotes convolution between the two functions. It can be shown that setting $\mu = 1$ in equation 6.19 yields an expression identical to that for diffraction of coherent light in the Fraunhofer regime.

6.3.2 Diffracting Structure

A test object is required for assessing the impact the modulated spatial properties may have on diffractive imaging type experiments. A so called 'non-redundant array' (NRA) was chosen.[1] An NRA is an arrangement of pinholes such that

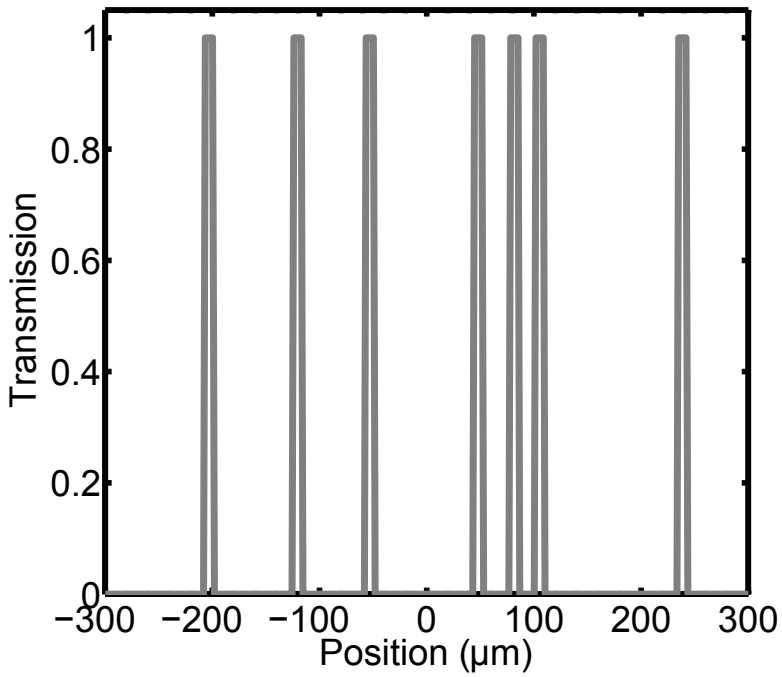

Figure 6.19: Plot showing the transmission function of the NRA used in the diffraction simulations described in this chapter. Each pinhole is 6.6 μm wide.

the separation between any two is unique and not repeated. It represents an

[1]Typically NRAs are two-dimensional structures, but the concept is equally valid in one spatial dimension, as considered here.

efficient sampling of reciprocal space points whilst minimising the total number of pinholes.

The idea of using an NRA to measure the spatial coherence of light has been explored both in the optical [110] and x-ray domains [44]. Just as a pinhole pair can encode the spatial coherence evaluated at one particular point separation through measuring the fringe visibility, the intensity pattern produced by an NRA has the potential to evaluate the CCF for multiple separations simultaneously. Analysis in general is simplified in the Fourier domain. However for accurate recovery of the CCF the (relative) intensity sampled by each pinhole in the NRA must be known.

For our simulation we are not so much interested in measuring the beam properties with an NRA as we are in evaluating the effect a modulated CCF may have on the resultant diffracted intensity pattern. The NRA used for the calculations described in this chapter is shown in figure 6.19. It is formed of seven pinholes[1], each of width 6.6 μm. For the diffraction calculations described here the (opaque part) of the NRA was extended to positions $x = \pm 690\,\mu$m, beyond what is shown in figure 6.19.

6.3.3 Diffraction from an NRA

For simplicity, we focus on the impact caused by modulations in the CCF, neglecting the similar effect observed in the intensity profile: in our calculation each aperture in the NRA was assumed to be illuminated by an equal intensity. The wavelength was set to that for $q = 29$ and the distance from the NRA to the detector was made to be 1 m. Using equation 6.17, the diffracted intensity pattern

[1] For an NRA of n pinholes, there are $\sum_{i=1}^{n}(i-1)$ possible pinhole separations.

was calculated for three cases:

1. Coherent light ($\mu = 1$). The diffraction pattern is shown in the upper plot of figure 6.20.

2. CCF as measured for $q = 29$ using SCIMITAR. The diffracted intensity is shown with a green dot-dashed line in the lower plot of figure 6.20.

3. CCF with a Gaussian shape. The width of the Gaussian was determined by a fit to the measured CCF of $q = 29$. The diffraction pattern is shown with a solid pink line in the lower plot of figure 6.20.

There is a clear difference in the diffraction patterns produced by the two partially coherent wavefronts, as evidenced in the lower plot of figure 6.20. This result indicates that the deviation from a monotonic form observed in the harmonic CCF will lead to a measurable difference in the measured diffraction pattern, compared to the case when the CCF is of Gaussian form. A study conducted by Williams et al. has shown that a small departure from full coherence can dramatically affect the fidelity of the reconstruction of the object transmission function for CDI-type techniques [36], while others have included the effects of partially coherent illumination into the reconstruction algorithm itself [46, 55]. Our results indicate that even if the partial coherence of light were built into the reconstruction through a one parameter function (e.g a Gaussian), erroneous results could well result.

This point is further illustrated in figure 6.21. Here an iterative phase retrieval program was used to reconstruct the NRA transmission function using

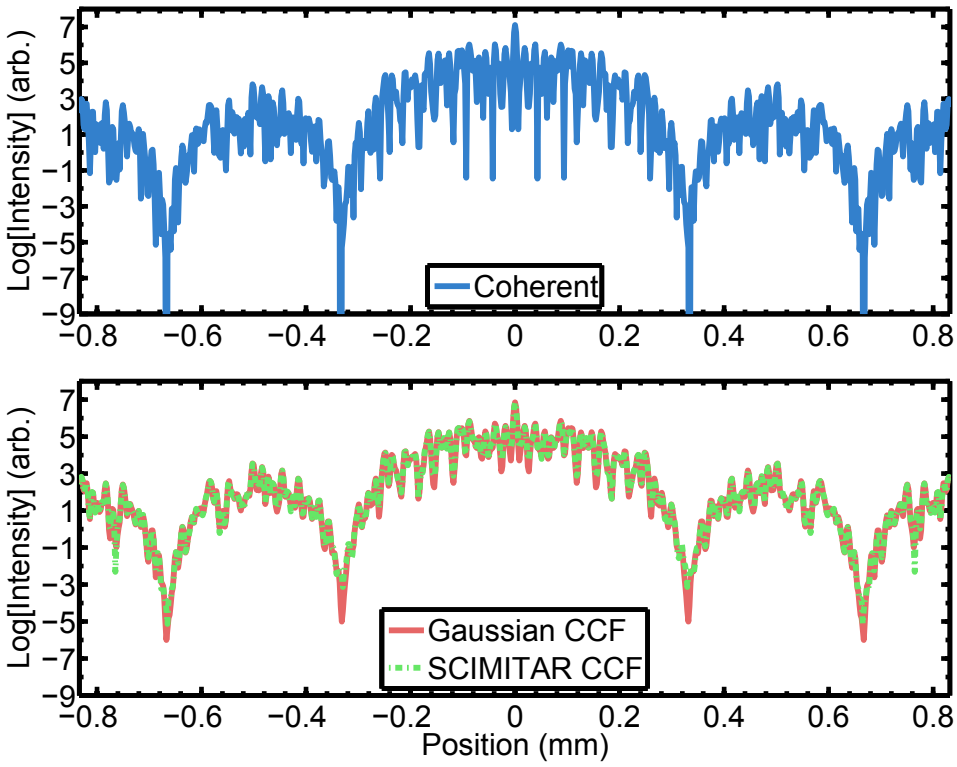

Figure 6.20: Upper plot: Diffracted intensity (on a log scale) for the NRA illuminated by coherent light. Lower plot: same as the upper plot but for partially coherent illumination either with a Gaussian shaped CCF (pink solid line) or a CCF as measured using SCIMITAR (dash-dotted green line). In all three cases the diffracted intensity was calculated setting the intensity at each pinhole in the NRA to unity and for $\lambda = 27.59$ nm and $z = 1$ m, where z is the detector - NRA longitudinal separation.

the diffraction patterns shown in figure 6.20. The algorithm used a combination of both the Gerchberg-Saxton and the Hybrid Input-Output approaches. The support was updated befor each iteration using the shrinkwrap approach [82]. The transmission functions shown in figure 6.21 were recovered after 700 iterations, where in all three cases the algorithm was judged to have stagnated. Figure 6.21 clearly shows that in the coherent case the NRA is reconstructed with excellent fidelity. In both the situations where the beam was partially coherent, with either a Gaussian CCF or CCF as presented in figure 6.1, the reconstruction fails. This underlines the importance of the role that spatial coherence can play in the success of lensless imaging experiments.

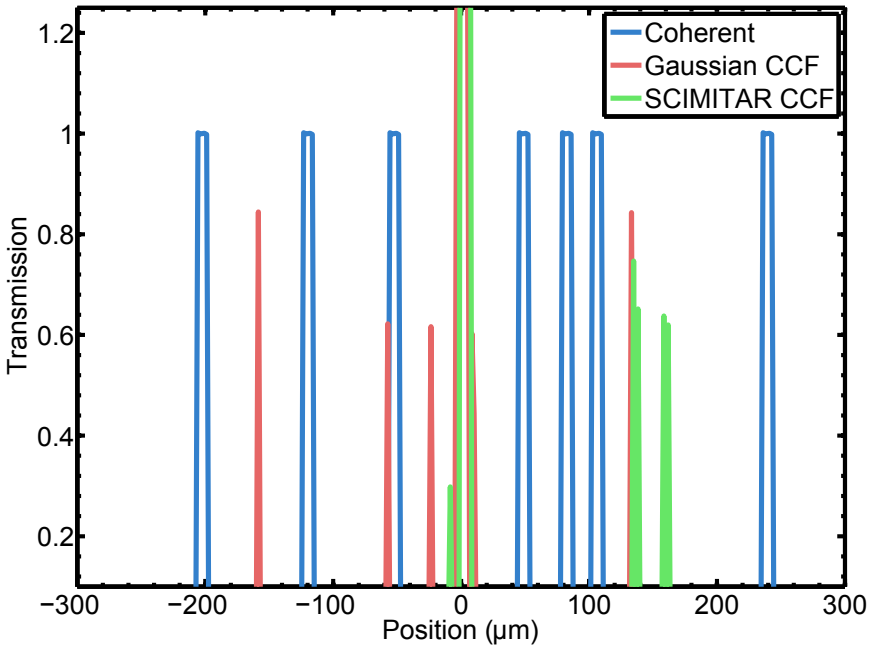

Figure 6.21: Reconstruction of the NRA for the three different degrees of spatial coherence considered. In the case where the NRA was illuminated with coherent light (blue line), an iterative phase retrieval algorithm recovered the transmission function with excellent fidelity. In the case of partially coherent illumination, (green and pink lines), the reconstruction failed.

6.4 Summary

In this chapter hitherto unreported modulations in the high order harmonic spatial properties were investigated. The positions of the so called 'shoulders' were found to vary with harmonic order in a way that suggested they may result from diffraction from an aperture in the plane where the harmonics were generated.

Application of the Van Cittert-Zernike theorem yielded a source intensity profile that was negative at certain positions in the generation plane. This was judged to have arisen from the extrapolation applied to the measured harmonic CCF. Augmentation of the Van Cittert-Zernike theorem with a Gerchberg-Saxton inspired algorithm overcame the negative intensity problem. The equivalent incoherent source intensity profile was found to be asymmetric with respect to position, with isolated, low intensity features appearing relatively far from the (orthogonal) optical axis.

The potential impact of the modulated spatial properties on lensless imaging experiments was investigated by calculating the diffraction pattern produced by illuminating a non-redundant array of pinholes with radiation with the same CCF as measured. The diffracted intensity was found to differ when compared to illumination with a Gaussian CCF. Reconstruction of the NRA transmission function using an iterative phase retrieval programme failed in both cases where the light was partially coherent. Together these results suggest that the CCF of the incident radiation must be well characterized before being utilised for applications dependent on the harmonic spatial coherence.

Chapter 7

Conclusion

This thesis has described a new technique for characterizing the spatial properties of light: SCIMITAR. Measurements of high harmonic generation driven by fundamental pulses of varying duration were reported. The key results are highlighted here, accompanied by a brief description of potential avenues of further research.

7.1 Summary of Work

The SCIMITAR technique itself was described in chapter 4. The interference patterns produced by the two-pinhole interferometer were shown to be more easily analysed in the Fourier domain, where a variation on the Takeda phase retrieval method was employed. Characterizing the spatial properties of HHG driven by 40 fs duration pulses showed that SCIMITAR retrieved the same beam intensity and spatial phase profiles as the SWORD technique. Measurement of the variation of the harmonic CCF with pinhole separation found that opposing sides of the beam differ in their coherence properties and that harmonic radiation was not shift invariant.

The spectral dependence of high harmonic spatial properties was investigated in chapter 5. Broadly speaking, both the intensity width and wavefront curvature were found to increase with harmonic order, with both quantities rolling off to constant values for the very highest orders. The harmonic coherence width was found to closely follow a q^{-1} relation. The intensity and coherence widths of the lowest harmonic orders ($q = 23$ and 25) were observed to differ significantly for the next lowest orders ($q = 27$ and 29). For orders 23 and 25 only, the absorption length was found to be smaller than both the coherence length and gas cell length, suggesting absorption plays a key role in defining the harmonic intensity profile and spatial coherence. By using expressions derived from the Gaussian-Schell model the harmonic intensity profile in the radiation generation plane was deduced. The harmonic intensity was found to obey $I_q = I_0^{\{q^n\}}$, where I_0 is the fundamental intensity and $n = 0.646 \pm 0.142$.

Modulations in the harmonic intensity and CCF were reported in chapter 6. The depth, position and period of the modulations were found to vary with harmonic order. The Van Cittert-Zernike theorem was augmented by including a modified version of Gerchberg-Saxton phase retrieval algorithm. The equivalent incoherent source intensity profile was found to be asymmetric, with isolated, low intensity features located up to positions $x = \pm 250\,\mu$m. The origin of the irregularity in the intensity profile is not apparent. The diffraction pattern produced from a pinhole array illuminated by the harmonic beam was calculated. There were marked differences between the patterns produced by a beam with a Gaussian CCF compared to that produced by a beam with a modulated CCF (as measured), suggesting that the fine structure within the harmonic spatial properties could adversely affect imaging applications.

The three experimental studies presented in chapters 4, 5 and 6 neatly display the strength and utility of the SCIMITAR technique. At the same time the results are testament to the rich behaviour of (and detailed information encoded within) the spatial properties of HHG. The conclusions we have drawn from the various studies contained within this thesis will be of immediate interest to groups interested in optimising and exploiting the desirable characteristics of HHG through various applications.

7.2 Future Prospects

The work contained in this thesis leaves a number of avenues of further investigation open. Here we outline three potential directions where further study could be directed.

7.2.1 Detailed Numerical Simulations

The bulk of the results presented in the three previous chapters are experimental in origin. The strength of the conclusions drawn would benefit from further information provided by numerical simulations. In particular, two areas have been identified where further computational work would aid the experimental results presented in this thesis.

In chapter 4 the CCF was found to be asymmetric with respect to pinhole separation. This result points towards the harmonic beam not possessing shift invariance. Previously reported numerical simulations of HHG have also found this to be the case [71]. Running similar simulations (as in [71]) for the experimental conditions of chapter 4 could allow us to be more confident that the asymmetry

recorded in the far-field results from harmonic dipole phase induced asymmetry during generation.

In chapter 5 harmonic orders 23 and 25 were observed to possess aberrant spatial properties. The two harmonic orders were identified as those being most affected by absorption within the gas cell. Numerical simulations of HHG, including the role of absorption and propagation, could add further evidence to the idea that the choice of generating gas plays an important role in shaping the harmonic spatial properties.

7.2.2 Characterizing Radiation from Free Electron Lasers

SCIMITAR has thus far been exclusively deployed to characterize high harmonic generation. However, the technique is equally well applicable to other sources of short-wavelength radiation. Fourth generation x-ray sources – Free Electron Lasers (FELs) – have been shown to produce the brightest pulses of coherent, ultrafast x-rays of any technique so far demonstrated [68]. The combination of short wavelength and pulse duration with high pulse energy and spatial coherence has enabled FELs to be used for a range of cutting-edge studies [60]. Further, the technique of 'seeding' has improved the shot-to-shot stability of such radiation sources [2]. This particular point is crucial for a multi-shot/scanning techniques: with the improved stability of the source it becomes feasible to characterize the radiation with SCIMITAR. Such a measurement would provide useful information for techniques utilising the high coherence and wavefront quality of light from FELs. Further, analysis of the spectral dependence of the beam properties could potentially be used as a diagnostic for optimising the FEL itself.

7.2.3 Characterizing HHG Driven by Shaped Laser Pulses

Spatial Light Modulators (SLMs) allow the spatial phase of a beam to be manipulated with unparalleled control. Previously, the brilliance of a high harmonic source has been optimised by using a genetic algorithm to manipulate the spatial phase distribution of the driving beam using such a device [45]. The SLM offers a number of interesting possibilities to not only to control the spatial properties of the harmonic field but also to probe aspects such as the role of the intensity dependence phase in shaping the harmonic beam. For both studies the same experimental arrangement could be employed, whereby the fundamental is first shaped by the SLM before being focussed into gas cell, with SCIMITAR being used to characterize the resultant high harmonic radiation. Such studies could simultaneously shed light on the physics of high intensity light-matter interaction while also serving to optimise the HHG radiation for a particular application.

Appendix A

SWORD Critique

A.1 Numerical Example

This section details a critique of the SWORD technique. This characterization method was first described by Frumker et al. in [33]. To briefly recap, SWORD measures the spectrally resolved intensity and spatial phase profiles of a beam of radiation. An aperture is scanned transversely across the beam and at each scan location a diffraction pattern is recorded. This critique specifically addresses the type of aperture used by the authors of [33] and how it can potentially lead to erroneous results.

In [33] the authors scanned a 20 μm wide slit transversely across a beam produced by a high harmonic radiation source. In figure A.1 we pictorially represent two possible transverse locations of the slit with respect to the fixed beam position. As the diagram shows, when the slit position corresponds with the beam centre it samples a large vertical area of the intensity distribution. Moving the slit to wings of the beam effectively reduces the sampled area. In order to spectrally

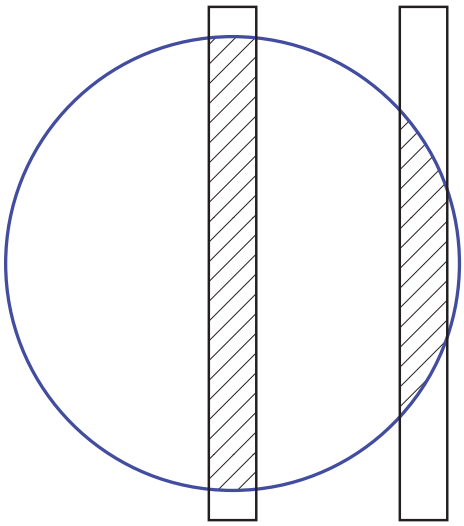

Figure A.1: Diagram depicting a thin extended slit sampling a beam a two different transverse locations during the course of a SWORD scan. The shaded area shows the area of the beam effectively sampled for each slit position.

resolve the beam spatial properties the (horizontally diffracted) diffraction pattern produced by the single slit is dispersed in the vertical direction by a grating. The recorded (intensity) diffraction pattern (for a given radiation wavelength), measured by the detector, is then the sum squared of the (field) diffraction patterns produced by each vertical location sampled by the slit.[1] Diffraction patterns from slit locations close to the centre part of the beam will therefore appear disproportionately brighter compared to those at the wings. Consequently, we expect that a SWORD scan performed using an extended slit will tend to retrieve intensity profiles which are narrower (brighter in the centre, dimmer in the wings) than what may actually be the case.

To illustrate the point raised above we numerically simulated a SWORD scan

[1]This point assumes the beam is spatially coherent. The effect of partial coherence is addressed further on.

of a monochromatic beam with a cylindrically symmetric top-hat intensity distribution (full width 1 mm). The scanning aperture was chosen to be a slit 20 μm wide in the scanning direction and 2 mm long in the vertical direction. The scan step size was 20 μm,with the scan itself composed of diffraction patterns from 50 different locations across the beam intensity profile.

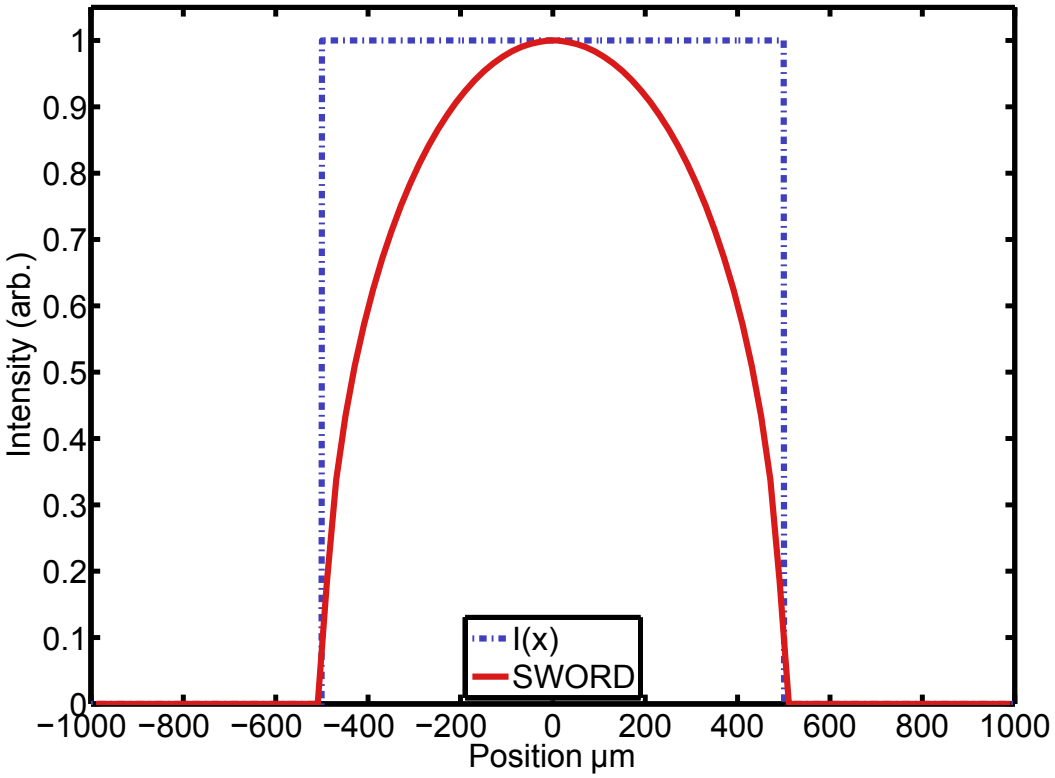

Figure A.2: Results of the simulated SWORD scan. The top-hat beam (blue dot-dashed line), was sampled at 20 μm intervals by a slit 20 μm wide and 2 mm long. Each SWORD data point (red solid line) is the sum squared of the field transmitted by the slit at that particular transverse location. The difference between the two intensity profiles is larger at locations further from the beam axis.

The results of the simulated SWORD scan are show in figure A.2. The recovered intensity profile (red solid line) is clearly both narrower and of an incorrect

shape compared to the actual beam profile (blue dashed line). The difference between the true and recovered beam profiles is more severe at locations further from the optical axis.

To further complicate the problem, the spatial coherence of the beam should be taken into account. In [33] the author's claimed that the radiation need only be spatially coherent over distances smaller than the slit width. However the fact that the slit is extended over a much larger distance in the vertical direction means the spatial coherence of the light (in the vertical direction) will determine the intensity recorded by the CCD. For a fixed slit position and beam shape, the signal recorded by the detector will be larger for a coherent beam than it would be for partially coherent radiation. It is clear then that the spatial coherence of beam (over distances larger than the slit width) is an important property in determining how severe the difference is between the recovered and true intensity profiles, as caused by the vertical extent of the slit.

In the original demonstration of SWORD reported in [33], the critiqe described above was mitigated somewhat by the use of a 100 μm wide spectrometer entry slit, with the entry slit orientated orthoganal to the scanning slit[1]. Nevertheless, each point in their scan represented the beam sampled over a significant (larger than the scanning slit width) vertical extent. Therefore, the fidelity of the intensity profiles (and widths) presented in [33] must be called into question.

The critique does not hold if a scanning pinhole is used in place of a slit, however a reduction in flux transmitted to the detector would be expected. Furthermore, if the radiation is known to be monochromatic (or very nearly at least), then the SWORD arrangement can be simplified by replacing the spectrometer

[1]The longitudinal distance between the two slits is not given in [33].

with just CCD alone. Then the vertical extent of the recorded image, rather than encoding the spectral properties of the beam, instead records the vertical variation in beam transverse intensity. In which case the critique described above is no longer relevant.

Appendix B

Space-Time Coupling

B.1 STC in Ultrashort Pulses

The discussion contained in sections 3.1.1 and 3.1.2 was limited to the situation where the electric field of the pulse may be expressed as the product of two functions, one of space, the other of time. However, this precludes the very real possibility that the spatial and temporal properties of a pulse may be coupled. This could manifest as a pulse duration which depends on the transverse location on the pulse, or equally well a time dependent wavefront. Such a situation is particularly adverse for characterization techniques which perform single-shot measurement through mapping of a transverse spatial dimension to time delay (see [30] for an example of this single-shot mapping).

B.1.1 Example: Pulse Front Tilt

A general theoretical description of space-time coupling based upon matrix manipulation was developed by Kostenbauder [104], however, for an example, we

consider only a common, specific manifestation of the phenomenon: pulse-front tilt (PFT). Pulse front tilt describes the presence of an angle between a line perpendicular to the direction of propagation and the pulse group front (the contour of equal intensity for a fixed time t). It is equivalent to a delay in arrival time across the transverse dimension of the pulse. Its existence has been connected to angular dispersion (a frequency dependent wavefront orientation), with authors claiming the two (angular dispersion and PFT) are one and the same [100]. However subsequent work identified that PFT could also result from the simultaneous presence of spatial and temporal chirp [78] even in the absence of angular dispersion.

To derive an expression for the PFT of a Gaussian pulse the notation of [78] is employed. A Gaussian spectrum with a linear (temporal) chirp (parameterised by $\phi^{(2)}$) can be written as:

$$E(\omega) = E_0 \exp\Big[-\frac{\omega^2\tau_0^2}{4}\Big] \exp\Big[-i\frac{\phi^{(2)}}{2}\omega^2\Big] \tag{B.1}$$

with the full pulse in the space-frequency domain taking the form of:

$$E(x,\omega) = E(\omega) \exp\Big[-\frac{k(x-\zeta\omega)^2}{kw_0^2}\Big] \exp(-ik_0\beta\omega x) \tag{B.2}$$

where k_0 is the central wavenumber of pulse spectrum and we have assumed a well collimated beam. The parameter β is used to parameterize the angular dispersion through:

$$\beta = \frac{\mathrm{d}\theta_0}{\mathrm{d}\omega} \tag{B.3}$$

where θ_0 is the propagation angle of frequency component ω. Here ζ is used to parameterize the spatial chirp through:

$$\zeta = \frac{\mathrm{d}x_0}{\mathrm{d}\omega} \tag{B.4}$$

where x_0 refers to the beam centre position of frequency component ω. The spatial chirp is often understood as the spatial gradient of the frequency:

$$\nu = \frac{\mathrm{d}\omega_0}{\mathrm{d}x} \tag{B.5}$$

which, for a Gaussian pulse, is related to our spatial chirp parameter ζ through

$$\nu = \frac{\zeta}{\zeta^2 + \frac{w_0^2\tau^2}{4}} \tag{B.6}$$

after substituting into equation B.1 and Fourier transforming into the space-time domain we arrive at

$$E(x,t) = f(x)\exp\Big[-\frac{(t-t_0)^2}{\tau^2}\Big]\exp\Big\{i\Big[\psi^{(1)}(t-t_0) + \frac{\psi^{(2)}}{2}(t-t_0)^2\Big]\Big\} \tag{B.7}$$

The details of functions $f(x)$, $\psi^{(1)}$ and $\psi^{(2)}$ are be found in [78] and are not included here for the sake of brevity. We are concerned with t_0 which is the pulse front arrival time:

$$t_0 = (k\beta + \phi^{(2)}\nu)x \tag{B.8}$$

which we observe now, for a pulse suffering PFT, is a function of transverse

position. The pulse front tilt itself (parameterised by p) is simply given by:

$$p = \frac{\mathrm{d}t_0}{\mathrm{d}x} = k\beta + \phi^{(2)}\nu \tag{B.9}$$

where the first term is caused by angular dispersion and the second term originates from the simultaneous presence of spatial and temporal chirp.

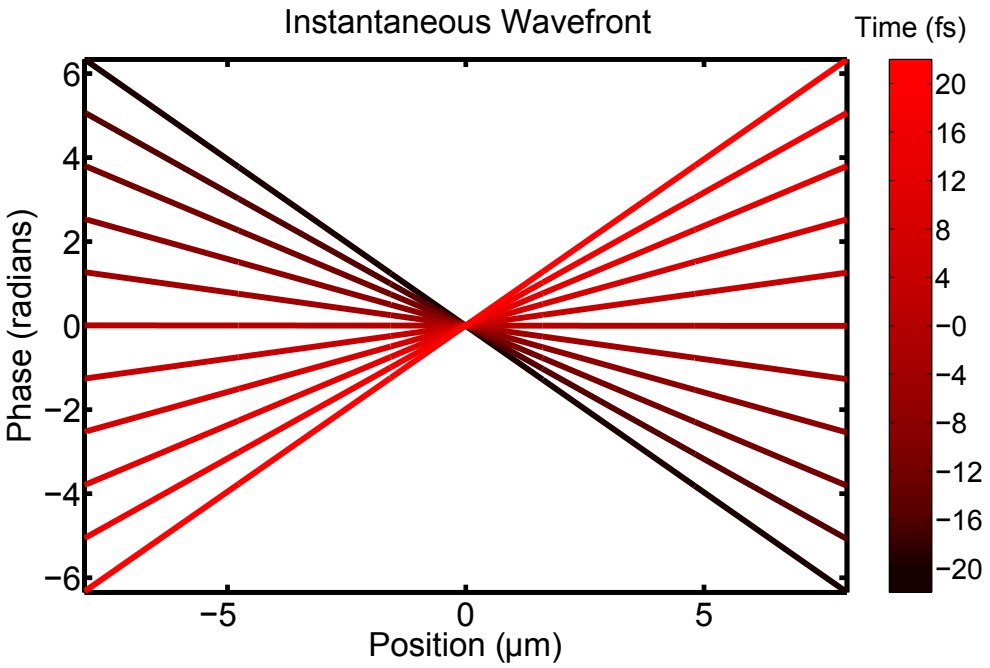

Figure B.1: Plot of the instantaneous pulse wavefront at focus. Each line corresponds to a different moment in time (given by the color). Pulse parameters: duration 15 fs, beam waist 47 μm, pulsefront tilt 0.35 fs mm^{-1} and focal length 0.375 m.

A beam suffering from pulse front tilt, will, when focussed, display wavefront rotation (WFR): the wavefront normal streaks out an arc over the duration of the pulse, as depicted in figure B.1. For a focal length f, the rotation velocity

(v_r) of the wavefront normal is given by:

$$v_r = \frac{w_0^2}{f\tau^2} \frac{p}{1 + \left(\frac{w_0 p}{\tau}\right)^2}. \tag{B.10}$$

The phenomenon of wavefront rotation may be deleterious especially in situations where a beam is focussed to produce a non-linear signal (SHG and HHG are two examples). However, its presence has been exploited, in the case of HHG, to produce a single attosecond pulse from a train of attosecond pulses, using the so called 'attosecond lighthouse' technique [120]. Each attosecond pulse in the train is generated at a different temporal point in the pulse and therefore is associated with a different wavefront normal. Hence, each attosecond pulse is emitted at a slightly different angle (with respect to the laser propagation axis).

B.1.2 Complete Space-Time Characterization

The existence of coupling between the spatial and temporal properties of a pulse necessitates the creation of diagnostics which are capable of accurately characterizing the pulse simultaneously in both domains. The increase in complexity of the information required to properly describe the pulse goes hand in-hand with the complexity of the measurement technique employed. Despite the technical challenge, space-time characterization methods covering a broad range of spectral regions have been proposed and demonstrated.

B.1.2.1 Visible and NIR

In section 3.3, two characterization techniques were described that made use of 'shearing' to measure particular properties of a pulse. In lateral shearing interferometry interference between a pulse and it's spatially sheared replica enables measurement of the wavefront. For SPIDER, interference between spectrally sheared pulses provides information on the spectral phase, and hence allows temporal characterization of a field. Dorrer et al. recognised that the simultaneous application of shears in both and space and frequency could be employed to perform space-time characterization of a pulse [13] in the visible and near-infrared spectral regions. A SPIDER like arrangement combined with a tilted arm Michelson interferometer was used to provide the spectral and spatial shears respectively. The experimental trace contained fringes in space and frequency forming a chequerboard like pattern. Despite the complexity of the arrangement, standard phase reconstruction procedures could be used to recover the spatial and spectral phase, and through other information contained in the trace, the full space-time map of an infrared pulse from a Titanium:Sapphire chirped pulse amplifier.

B.1.2.2 XUV and SXR

The difficulty of performing space-time characterization of short-wavelength light would seem a first glance to be insurmountable; especially given the fact that techniques using non-linear crystals, common in the visible spectrum, are not available. However, Kim and co-authors, through their approach, were able to successfully characterize simultaneously the spatial and temporal properties of

isolated attosecond pulses from HHG [53]. A weak[1] second harmonic field was mixed at a small angle with the fundamental in the generation region, with the harmonic signal recorded in the spatial-spectral domain (x, ω). By measuring the deflection of the harmonic beam (in x) as a function of both the delay of the second harmonic (with respect to the fundamental) and high harmonic order, the authors were able to retrieve the full space-time map of the attosecond burst, revealing the space-time coupling in the emitted radiation. This work stands to markedly improve the utilisation of attosecond pulses, through, for instance, revealing the variation of pulse duration with transverse position, informing future applications of this unique light source.

[1]The field perturbs the process enough to provide an experimentally measurable signal (deflection), but not so much as to drastically change the generation process.

References

[1] G. Agrawal. Second-harmonic generation with arbitrary pump-beam profiles. *Physical Review A*, 23(4):1863–1868, April 1981. 27

[2] E. Allaria, R. Appio, and L. Badano. Highly coherent and stable pulses from the FERMI seeded free-electron laser in the extreme ultraviolet. *Nature Photonics*, 6:699 – 704, 2012. 194

[3] M. V. Ammosov, N. B. Delone, and V. P. Krainov. Tunnel ionization of complex atoms and of atomic ions in an alternating electromagnetic field. *Sov Phys JETP*, 64(6):1191–1194, 1986. 11, 12, 133, 180

[4] M. Born and E. Wolf. Principles of Optics. 36, 43, 63, 88, 158

[5] R.W. Boyd. Nonlinear Optics. 17

[6] T. Brabec and F. Krausz. Intense few-cycle laser fields: Frontiers of nonlinear optics. *Reviews of Modern Physics*, 72(2):545, April 2000. 20

[7] P. H. Van Cittert. Kohaerenz-probleme. *Physica*, (10), 1939. 43

[8] E. Collett. Beams generated by Gaussian quasi-homogeneous sources. *Optics Communications*, 32(1):27–31, January 1980. 36

[9] E. Collett and E. Wolf. Is complete spatial coherence necessary for the generation of highly directional light beams? *Optics letters*, 2(2):27, February 1978. 28

[10] J. W. Cooper. Photoionization from outer atomic subshells. A model study. *Physical Review*, 128(1), 1962. 121

[11] P. B. Corkum. Plasma perspective on strong field multiphoton ionization. *Physical Review Letters*, 71(13):1994–1997, September 1993. 8

[12] H. Daido. Review of soft x-ray laser researches and developments. *Reports on Progress in Physics*, 65(10):1513–1576, October 2002. 2

[13] C. Dorrer, E. M. Kosik, and I. A. Walmsley. Spatio-temporal characterization of the electric field of ultrashort optical pulses using two-dimensional shearing interferometry. *Applied Physics B: Lasers and Optics*, 74(9):s209–s217, June 2002. 206

[14] A. Le et al. Quantitative rescattering theory for high-order harmonic generation from molecules. *Physical Review A*, 80(1):013401, July 2009. 22

[15] A. L'Huillier et al. High-order Harmonic-generation cutoff. *Physical Review A*, 48(5):R3433–R3436, November 1993. 14, 17

[16] A. McPherson et al. Studies of multiphoton production of vacuum-ultraviolet radiation in the rare gases. *Journal of the Optical Society of America B*, 4(4):595, April 1987. 1, 27

[17] A. Schropp et al. Full spatial characterization of a nanofocused x-ray free-

electron laser beam by ptychographic imaging. *Scientific Reports*, 3:1–5, April 2013. 72

[18] A. Zaïr et al. Spatio-temporal characterization of few-cycle pulses obtained by filamentation. *Optics express*, 15(9):5394–404, April 2007. 112

[19] B. Flöter et al. EUV Hartmann sensor for wavefront measurements at the Free-electron LASer in Hamburg. *New Journal of Physics*, 12(8):083015, August 2010. 63, 65, 66

[20] B. Shan et al. Tunable high harmonic generation with an optical parametric amplifier. *Applied Physics B: Lasers and Optics*, 74(9):s23–s26, June 2002. 110

[21] C. Durfee et al. Phase matching of high-order harmonics in hollow waveguides. *Physical Review Letters*, 83(11):2187–2190, September 1999. 21, 128, 146

[22] C. Erny et al. Metrology of high-order harmonics for free-electron laser seeding. *New Journal of Physics*, 13(7):073035, July 2011. 67

[23] C. Gohle et al. A frequency comb in the extreme ultraviolet. *Nature*, 436(7048):234–7, July 2005. 3

[24] C. La-O-Vorakiat et al. Ultrafast demagnetization dynamics at the M edges of magnetic elements observed using a tabletop high-harmonic soft x-rays source. *Physical Review Letters*, 103(25):1–4, December 2009. 3

[25] C. P. Hauri et al. Generation of intense, carrier-envelope phase-locked few-

cycle laser pulses through filamentation. *Applied Physics B*, 79(6):673–677, September 2004. 112

[26] C. Q. Tran et al. Experimental measurement of the four-dimensional coherence function for an undulator x-ray source. *Physical Review Letters*, 98(22):224801, May 2007. 75

[27] C. Valentin et al. High-order harmonic wave fronts generated with controlled astigmatic infrared laser. *JOSA B*, 25(7):B161–B166, 2008. 66

[28] D. Austin et al. Lateral shearing interferometry of high-harmonic wavefronts. *Optics letters*, 36(10):1746–8, May 2011. 25, 71, 101, 137

[29] D. G. Lee et al. Wave-front phase measurements of high-order harmonic beams by use of point-diffraction interferometry. *Optics letters*, 28(6):480–2, March 2003. 72

[30] D. J. Kane et al. Single-shot measurement of the intensity and phase of a femtosecond UV laser pulse with frequency-resolved optical gating. *Optics letters*, 19(14):1061–3, July 1994. 201

[31] E. A. Gibson et al. Coherent soft x-ray generation in the water window with quasi-phase matching. *Science (New York, N.Y.)*, 302(5642):95–8, October 2003. 18

[32] E. Constant et al. Optimizing high harmonic generation in absorbing gases: model and experiment. *Physical Review Letters*, 82(8):1668–1671, February 1999. 128

[33] E. Frumker et al. Frequency-resolved high-harmonic wavefront characterization. *Optics Letters*, 34(19):3026–3028, 2009. 67, 70, 82, 101, 196, 199

[34] E. Frumker et al. Order-dependent structure of high harmonic wavefronts. *Optics Express*, 20(13):13870–13877, 2012. 67, 70, 71, 109, 126, 129, 130

[35] G. Sansone et al. Isolated single-cycle attosecond pulses. *Science (New York, N.Y.)*, 314(5798):443–6, October 2006. 3

[36] G. Williams et al. Coherent diffractive imaging and partial coherence. *Physical Review B*, 75(10):104102, March 2007. 187

[37] H. Diao et al. Carrier-envelope phase effects on the spatial coherence of high-order harmonics. *Optics Express*, 22(15):17657, July 2014. 76

[38] H. Shin et al. Nonadiabatic blueshift of high-order harmonics from Ar and Ne atoms in an intense femtosecond laser field. *Physical Review A*, 63(5):053407, April 2001. 120

[39] H. Takajo et al. Study on the convergence property of the hybrid inputoutput algorithm used for phase retrieval. *JOSA A*, 15(11):2849–2861, 1998. 169

[40] H. Wörner et al. Observation of Electronic Structure Minima in High-Harmonic Generation. *Physical Review Letters*, 102(10):103901, March 2009. 121

[41] I. C. E. Turcu et al. Spatial coherence measurements and x-ray holographic imaging using a laser-generated plasma x-ray source in the water window spectral region. *Journal of Applied Physics*, 73(12):8081, 1993. 4

[42] J. Collier et al. A single-shot third-order autocorrelator for pulse contrast and pulse shape measurements. *Laser and Particle Beams*, 19(2):231–235, April 2001. 58

[43] J. Higuet et al. High-order harmonic spectroscopy of the Cooper minimum in argon: Experimental and theoretical study. *Physical Review A*, 83(5):053401, May 2011. 121

[44] J. Lin et al. Measurement of the Spatial Coherence Function of Undulator Radiation using a Phase Mask. *Physical Review Letters*, 90(7):074801, February 2003. 186

[45] J. Lohbreier et al. Maximizing the brilliance of high-order harmonics in a gas jet. *New Journal of Physics*, 11(2):023016, February 2009. 63, 65, 67, 195

[46] J. N. Clark et al. High-resolution three-dimensional partially coherent diffraction imaging. *Nature communications*, 3:993, January 2012. 187

[47] J. P. Farrell et al. Influence of phase matching on the Cooper minimum in Ar high-order harmonic spectra. *Physical Review A*, 83(2):023420, February 2011. 121

[48] J. Ratner et al. Coherent artifact in modern pulse measurements. *Optics letters*, 37(14):2874–6, July 2012. 180

[49] J. Rothhardt et al. Enhancing the macroscopic yield of narrow-band high-order harmonic generation by Fano resonances. *Physical Review Letters*, 112(23):233002, June 2014. 128

[50] J. S. Robinson et al. The generation of intense, transform-limited laser pulses with tunable duration from 6 to 30 fs in a differentially pumped hollow fibre. *Applied Physics B*, 85(4):525–529, August 2006. 114, 116

[51] J. Seres et al. Coherent superposition of laser-driven soft-X-ray harmonics from successive sources. *Nature Physics*, 3(12):878–883, November 2007. 18

[52] J. W. G. Tisch et al. Angularly-resolved high-order harmonic generation in helium. *Journal of Modern ...*, 49(1), 1994. 27

[53] K. T. Kim et al. Manipulation of quantum paths for spacetime characterization of attosecond pulses. *Nature Physics*, 9(2):1–5, January 2013. 80, 207

[54] L. Le Déroff et al. Measurement of the degree of spatial coherence of high-order harmonics using a Fresnel-mirror interferometer. *Physical Review A*, 61(4):43802, March 2000. 75

[55] L. W. Whitehead et al. Diffractive Imaging Using Partially Coherent X Rays. *Physical Review Letters*, 103(24):243902, December 2009. 187

[56] L. Zhu et al. Wave-front generation of Zernike polynomial modes with a micromachined membrane deformable mirror. *Applied optics*, 38(28):6019–26, October 1999. 63

[57] M. Gaarde et al. Spatiotemporal separation of high harmonic radiation into two quantum path components. *Physical Review A*, 59(2):1367–1373, February 1999. 139

[58] M. Hentschel et al. Attosecond metrology. *Nature*, 414(6863):509–13, November 2001. 3

[59] M. Lewenstein et al. Theory of high-harmonic generation by low-frequency laser fields., March 1994. 15

[60] M. M. Seibert et al. Single mimivirus particles intercepted and imaged with an X-ray laser. *Nature*, 470(7332):78–81, February 2011. 2, 194

[61] M. Nisoli et al. A novel-high energy pulse compression system: generation of multigigawatt sub-5-fs pulses. *Applied Physics B: Lasers and Optics*, 65(2):189–196, August 1997. 112, 116

[62] M. Praeger et al. Spatially resolved soft X-ray spectrometry from single-image diffraction. *Nature Physics*, 3(3):176–179, February 2007. 66

[63] M. Schnürer et al. Absorption-limited generation of coherent ultrashort soft-X-ray pulses. *Physical Review Letters*, 83(4):722–725, July 1999. 128

[64] M. Zepf et al. Bright quasi-phase-matched soft-x-ray harmonic radiation from argon ions. *Physical Review Letters*, 143901(October):1–4, 2007. 18

[65] N. Wagner et al. Self-compression of ultrashort pulses through ionization-induced spatiotemporal reshaping. *Physical Review Letters*, 93(17):173902, October 2004. 112

[66] O. Smirnova et al. High harmonic interferometry of multi-electron dynamics in molecules. *Nature*, 460(7258):972–7, August 2009. 22

[67] P. Balcou et al. Generalized phase-matching conditions for high harmonics: The role of field-gradient forces. *Physical Review A*, 55(4):3204–3210, April 1997. 25, 26

[68] P Emma et al. First lasing and operation of an angstrom-wavelength free-electron laser. *Nature Photonics*, 4(August):641–647, 2010. 194

[69] P O'Shea et al. Highly simplified device for ultrashort-pulse measurement. *Optics letters*, 26(12):932–4, June 2001. 60, 116

[70] P. Salieres et al. Spatial profiles of high-order harmonics generated by a femtosecond Cr: LiSAF laser. *Journal of Physics B: ...*, 217, 1994. 27, 101, 126

[71] P. Salieres et al. Study of the spatial and temporal coherence of high order harmonics. *arXiv preprint quant-ph/*, 1(1):1–39, 1997. 22, 25, 82, 105, 193

[72] R. A. Bartels et al. Generation of spatially coherent light at extreme ultraviolet wavelengths. *Science*, 297(5580):376, 2002. 4, 76, 104, 106, 150

[73] R. A. Ganeev et al. Spatial coherence measurements of non-resonant and resonant high harmonics generated in laser ablation plumes. *Applied Physics Letters*, 104(2):021122, January 2014. 73

[74] R. I. Tobey et al. Ultrafast extreme ultraviolet holography: dynamic monitoring of surface deformation. *Optics letters*, 32(3):286–8, February 2007. 4

[75] R. K. Singh et al. Vectorial van Cittert-Zernike theorem based on spatial

averaging: experimental demonstrations. *Optics letters*, 38(22):4809–12, November 2013. 42

[76] R. Sandberg et al. Lensless diffractive imaging using tabletop coherent high-harmonic soft-x-ray Beams. *Physical Review Letters*, 99(9):1–4, August 2007. 4

[77] R. Szipocs et al. Chirped multilayer coatings for broadband dispersion control in femtosecond lasers. *Optics letters*, 19(3):201, February 1994. 113

[78] S. Akturk et al. Pulse-front tilt caused by spatial and temporal chirp. *Optics express*, 12(19):4399–410, September 2004. 202, 203

[79] S. Akturk et al. The general theory of first-order spatio-temporal distortions of Gaussian pulses and beams. *Optics express*, 13(21):8642–61, October 2005. 30

[80] S. Baker et al. Probing proton dynamics in molecules on an attosecond time scale. *Science (New York, N.Y.)*, 312(5772):424–7, April 2006. 3

[81] S. Bodrov et al. Plasma filament investigation by transverse optical interferometry and terahertz scattering. *Optics express*, 19(7):6829–35, March 2011. 88

[82] S. Marchesini et al. X-ray image reconstruction from a diffraction pattern alone. *Physical Review B*, 68(14):1–4, October 2003. 172, 189

[83] S. Rutishauser et al. Exploring the wavefront of hard X-ray free-electron laser radiation. *Nature communications*, 3:947, January 2012. 72

[84] S. Skupin et al. Self-compression by femtosecond pulse filamentation: Experiments versus numerical simulations. *Physical Review E*, 74(5):056604, November 2006. 112

[85] T. Ditmire et al. Spatial coherence measurement of soft x-ray radiation produced by high order harmonic generation. *Physical Review Letters*, 77(23):4756–4759, December 1996. 28, 82, 104, 106, 150

[86] T. Ditmire et al. Spatial coherence of short wavelength high-order harmonics. *Applied Physics B:*, 328:313–328, 1997. 76, 106, 126

[87] T. Mey et al. Wigner distribution measurements of the spatial coherence properties of the free-electron laser FLASH. *Optics Express*, 22(13):16571–16584, 2014. 75

[88] T. Popmintchev et al. Bright coherent ultrahigh harmonics in the keV x-ray regime from mid-infrared femtosecond lasers. *Science (New York, N.Y.)*, 336(6086):1287–91, June 2012. 1, 110

[89] W. A. Barletta et al. Free electron lasers: Present status and future challenges. *Nuclear Instruments and Methods in Physics Research Section A: Accelerators, Spectrometers, Detectors and Associated Equipment*, 618(1-3):69–96, June 2010. 65

[90] X. Zhang et al. Quasi-phase-matching and quantum-path control of high-harmonic generation using counterpropagating light. *Nature Physics*, 3(4):270–275, February 2007. 19

[91] Y. Mairesse et al. Attosecond synchronization of high-harmonic soft x-rays. *Science (New York, N.Y.)*, 302(5650):1540–3, November 2003. 3

[92] Y. Takayama et al. Relationship between spatial coherence of synchrotron radiation and emittance. *Journal of synchrotron radiation*, 5(Pt 4):1187–94, July 1998. 4

[93] J. R. Fienup. Reconstruction of an object from the modulus of its Fourier transform. *Optics letters*, 3(1):27–29, 1978. 162

[94] P. A Franken and A. E. Hill. Generation of optical harmonics. *Physical Review*, 7(1):118–120, 1961. 1

[95] J. Gautier, P. Zeitoun, and C. Hauri. Optimization of the wave front of high order harmonics. *The European Physical*, 463:459–463, 2008. 65, 66

[96] D. C. Ghiglia and M. D. Pritt. Two-dimensional phase unwrapping: theory, algorithms and software. 92, 93

[97] E. Gibson. Quasi-phase matching of soft x-ray light from high-order harmonic generation using waveguide structures (PhD Thesis). 180

[98] J. W. Goodman. Statistical Optics. 36, 48, 182

[99] F. Gori and C. Palma. Partially coherent sources which give rise to highly directional light beams. *Optics Communications*, 27(2):185–188, 1978. 47

[100] J. Hebling. Derivation of the pulse front tilt caused by angular dispersion. *Optical and Quantum Electronics*, 28(12):1759–1763, December 1996. 202

[101] C. Iaconis and I. A. Walmsley. Spectral phase interferometry for direct electric-field reconstruction of ultrashort optical pulses. *Optics letters*, 23(10):792–4, May 1998. 88

[102] K. Janssens. Synchrotron radiation in art and archaeology. *Journal of Analytical Atomic Spectrometry*, 26(5):883, 2011. 2

[103] J. Kasparian and J. Wolf. Physics and applications of atmospheric nonlinear optics and filamentation. *Optics express*, 16(1):466–93, January 2008. 112

[104] A.G. Kostenbauder. Ray-pulse matrices: a rational treatment for dispersive optical systems. *IEEE Journal of Quantum Electronics*, 26(6):1148–1157, June 1990. 201

[105] J. L. Krause, K. J. Schafer, and K. C. Kulander. High-order harmonic generation from atoms and ions in the high intensity regime., June 1992. 15

[106] L. Le Déroff, P. Salières, and B. Carré. Beam-quality measurement of a focused high-order harmonic beam. *Optics letters*, 23(19):1544–6, October 1998. 128

[107] M. Lewenstein, P. Salieres, and A. L'huillier. Phase of the atomic polarization in high-order harmonic generation. *Physical Review A*, 52(6):4747–4754, 1995. 16, 23, 144

[108] D. T. Lloyd, K. O'Keeffe, and S. M. Hooker. Complete spatial characterization of an optical wavefront using a variable-separation pinhole pair. *Optics Letters*, 38(7):1173, April 2013. 82

[109] T. H. Maiman. Stimulated Optical Radiation in Ruby. *Nature*, 187(4736):493–494, August 1960. 1

[110] Y. Mejía and A. I. González. Measuring spatial coherence by using a mask with multiple apertures. *Optics Communications*, 273(2):428–434, May 2007. 186

[111] K. O'Keeffe, T. Robinson, and S. M Hooker. Quasi-phase-matching high harmonic generation using trains of pulses produced using an array of birefringent plates. *Optics express*, 20(6):6236–47, March 2012. 134

[112] J. Peatross, J. R. Miller, and K. R. Smith. Phase matching of high-order harmonic generation in helium-and neon-filled gas cells. *Journal of Modern*, (April):37–41, 2004. 135

[113] B. C. Platt and R. Shack. History and principles of Shack-Hartmann wavefront sensing. *Journal of Refractive Surgery*, 17(October 2001), 2001. 63

[114] P. Salières, A. L'Huillier, and M. Lewenstein. Coherence Control of High-Order Harmonics, May 1995. 25

[115] B. Schäfer and K. Mann. Determination of beam parameters and coherence properties of laser radiation by use of an extended Hartmann-Shack wavefront sensor. *Applied optics*, 41(15):2809–2817, 2002. 64

[116] Diamond Light Source. Diamond light source faq, March 2014. 2

[117] Mitsuo Takeda, Hideki Ina, and Seiji Kobayashi. Fourier-transform method of fringe-pattern analysis for computer-based topography and interferom-

etry. *Journal of the Optical Society of America*, 72(1):156, January 1982. 88

[118] B. J. Thompson and E. Wolf. Two-beam interference with partially coherent light. *JOSA*, 47(10):895–902, 1957. 73, 74

[119] I. A. Vartanyants and A. Singer. Coherence properties of hard x-ray synchrotron sources and x-ray free-electron lasers. *New Journal of Physics*, 12(3):035004, March 2010. 52

[120] H. Vincenti and F. Quéré. Attosecond lighthouses: how to use spatiotemporally coupled light fields to generate isolated attosecond pulses. *Physical Review Letters*, 108(11):113904, March 2012. 205

[121] C. G. Wahlström, J. Larsson, and A. Persson. High-order harmonic generation in rare gases with an intense short-pulse laser. *Physical Review A*, 48(6), 1993. 7, 8

[122] I. A. Walmsley and C Dorrer. Characterization of ultrashort electromagnetic pulses. *Advances in Optics and Photonics*, 1(2):308, April 2009. 59

[123] E. Wolf. Partially coherent sources which produce the same far-field intensity distribution as a laser. *Optics Communications*, 25(3):293–296, 1978. 131

[124] H. L. Xu and S. L. Chin. Femtosecond laser filamentation for atmospheric sensing. *Sensors (Basel, Switzerland)*, 11(1):32–53, January 2011. 112

[125] T. Young. The Bakerian lecture: On the theory of light and colours. *Philosophical transactions of the Royal ...*, 92(1802):12–48, 1802. 28, 38

[126] F. Zernike. The concept of degree of coherence and its application to optical problems. *Physica*, (8):785–795, 1938. 43

[127] F. Zernike. Diffraction and optical image formation. *Proceedings of the Physical Society*, 158, 1948. 43